SUMMARY OF STRESS CORROSION CRACK INITIATION MEASUREMENTS AND ANALYSES ON ALLOY 600 AND ALLOY 690

Technical Milestone Report: M2LW-15OR0402034
September 2015

Z. Zhai, M. J. Olszta, M. B. Toloczko and S. M. Bruemmer
Pacific Northwest National Laboratory

Research Project:
Stress Corrosion Crack Initiation of
Nickel-Base Alloys in LWR Environments
Project Manager: S. M. Bruemmer
Pacific Northwest National Laboratory

Conducted for:
Office of Nuclear Energy, U.S. Department of Energy
Light Water Reactor Sustainability Program
Materials Aging and Degradation Pathway
Pathway Manager: K. J. Leonard
Oak Ridge National Laboratory

Table of Contents

Project Background

Objective

This research project addresses one of the least understood aspects of stress corrosion cracking (SCC) for light-water reactor (LWR) pressure boundary components - crack initiation. The focus of the work is to investigate important material (composition, processing, microstructure, strength) and environmental (temperature, water chemistry, electrochemical potential, stress) effects on the SCC susceptibility of corrosion-resistant, nickel-base alloys. The primary objectives are to identify mechanisms controlling crack nucleation, investigate the transition from short to long crack growth in these alloys under realistic LWR conditions and help establish the framework to effectively model and mitigate SCC initiation processes.

Approach

Alloy 600 materials were selected for the first phase of SCC initiation experimentation followed by testing on the more resistant alloy 690 materials. For both alloys, material variants known to influence SCC response are being examined including cold/warm work (forged, rolled and tensile strained), banded/inhomogeneous microstructures (plate versus extruded tubing), grain boundary precipitation (heat-to-heat variations, mill-annealed, solution annealing and changes due to thermal treatments) and surface grinding (various damage depths, surface roughness and nanocrystalline layers). Materials and material conditions have been identified and obtained from ongoing research projects where stress-corrosion crack growth has been characterized, thus creating an important link between SCC initiation and propagation behavior. Detailed examinations have been performed using optical and electron microscopy to establish key bulk and surface microstructural features that may act as initiation precursors. Dedicated test systems with continuous in-situ detection of crack formation were designed and constructed enabling SCC initiation experimentation of a range of alloy 600 and 690 materials. After SCC testing in high temperature autoclave systems, surface and near-surface characterizations were conducted to document nano-to-microscale initiation precursors leading to macroscopic stress corrosion cracks. The fundamental understanding of how the near-surface microstructure is degraded during high-temperature water exposure is essential to an improved predictive methodology for SCC initiation.

Focus of Current Report

This report reviews recent SCC initiation testing on alloy 600 and alloy 690 materials in high-temperature, simulated PWR primary water. It follows earlier milestone reports [1-3] that described our first SCC initiation tests and corrosion-structure characterizations on alloy 600 and alloy 690 materials. Current results have established baseline responses for as-received and cold-worked (CW) alloy 600 with constant load, SCC initiation tests performed on three material

heats. Alloy 600 cold work levels from 7% to 20% have been assessed along with ongoing tests on specimens in the as-received (AR), mill-annealed (MA) condition. Scanning electron microscopy (SEM) is used extensively for the characterization of material, corrosion and crack microstructures. Observations of nanoscale precursor intergranular attack (IGA) and small IGSCC cracks are linked to macroscopic SCC initiation. Critical assessments have been performed to determine the fidelity of in-situ direct current potential drop (DCPD) detection capability and provide insights into mechanisms controlling crack nucleation. Ongoing SCC initiation tests on CW alloy 690 heats are also reviewed. Due to its much higher resistance to SCC, blunt-notch initiation tests that employ minor applications of dynamic strain to promote crack nucleation are included along with long-term, constant load tensile tests on materials with 12-31% cold work. A key issue for crack initiation for the alloy 690 materials is whether dynamic straining is required for IGSCC initiation. Slow-strain-rate deformation is shown to promote formation of grain boundary creep cavities in CW alloy 690 that may control nucleation of surface cracks.

Materials and Experimental Methods for SCC Initiation Tests

Materials and Microstructures – Alloy 600

Two control rod drive mechanism (CRDM) heats and one plate heat were tested with compositions listed in Table 1. All materials were received and tested in the MA condition with or without additional cold work. The first heat (M3935) comes from the decontaminated CRDM nozzle #1 of the original Davis Besse reactor pressure vessel head replaced in 2002 after ~15.8 effective full power years of operation [4]. This heat exhibited high SCC susceptibility in PWR primary water service and during crack-growth tests at PNNL and Argonne National Laboratory [5,6]. It was reported to have a final MA temperature of 871 to 927°C and a yield strength of 334 MPa. Very large grains were found in this CRDM tubing ranging from 150–500 µm in diameter with a semi-continuous distribution of carbides spaced ~500 nm apart, as illustrated in Figure 1. In addition, a high bulk concentration and grain boundary segregation [7] of boron was present for this MA material.

Table 1. Bulk compositions of alloy 600 materials for this study.

Product	**Heat**	**Ni**	**Cr**	**Fe**	**Mn**	**C**	**Si**	**Cu**	**P**	**S**	**B, appm**
Service CRDM	M3935	77.9	15.6	6.3	0.27	0.028	0.37	0.01	0.004	0.002	69
CRDM Tube	93510	74.4	15.4	8.9	0.23	0.047	0.30	0.01	0.005	0.002	NM
Plate	NX6106XK-11	74.0	16.4	8.5	0.23	0.060	0.22	0.01	0.004	0.001	NM

*NM = not measured.

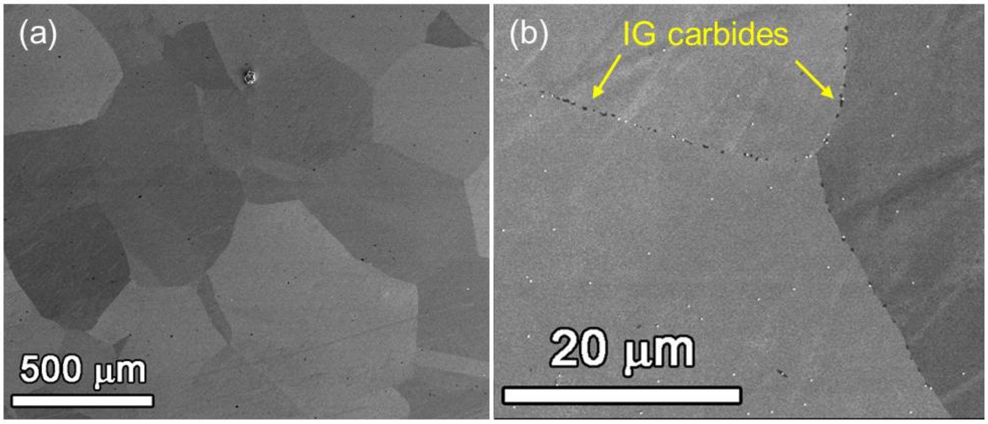

Figure 1. SEM backscatter electron (BSE) images illustrating (a) the general microstructure and large grain size and (b) the uniform distribution of IG carbides in the MA alloy 600 service CRDM heat M3935.

The second CRDM heat (93510) was obtained from General Electric Global Research (GEG). Reported yield and tensile strengths for this material are 269 and 678 MPa with an elongation to failure of 48%. Ladle analysis did indicate a small amount of B, but GDMS measurements were not conducted to quantify the concentration, nor has grain boundary compositions been determined. As illustrated in Figure 2, the microstructure of this heat is very different from that of the service CRDM (M3935) heat. It has a much smaller grain size of ~20–25 µm with transgranular (TG) carbides that appeared to have formed on prior grain boundaries.

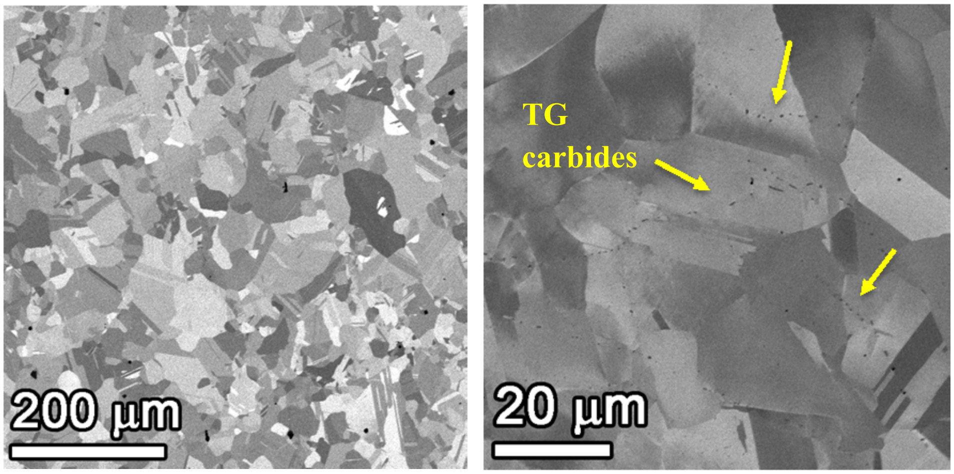

Figure 2. SEM-BSE images illustrating the microstructure of CRDM tube heat 93510 and the TG nature of the carbides.

The final heat (NX6106XK-11) is a 2-inch thick alloy 600 plate mill annealed at 927°C for 3.5 hours followed by a water quench. Mill specs indicated that the yield and tensile strengths were 259 and 667 MPa with an elongation to failure of 43%. It features a moderate grain size with an average diameter of ~65 µm. As shown in Figure 3, both TG carbides on prior grain boundaries and a non-uniform distribution of IG carbides were observed in this material.

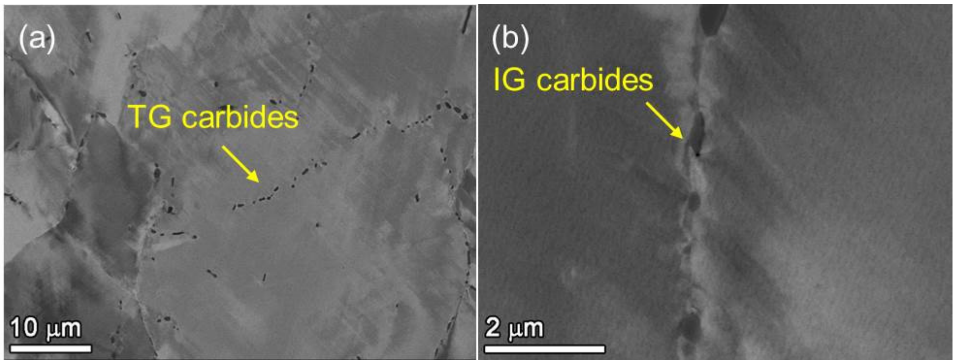

Figure 3. SEM-BSE images illustrating (a) TG (typically along prior grain boundaries) and (b) isolated IG carbides in plate heat NX6106XK-11.

A summary of the measured microstructures for these three heats is provided in Table 2.

Table 2. Microstructural characterization of alloy 600 materials.

Component	Heat	Grain Size (µm)	Strain Contrast	Primary Carbide Location	IG Carbide Density
CRDM Nozzle	M3935	150–500	Low	IG	500 nm spacing
CRDM Tube	93510	20–25	Low	TG	N/A
Plate	NX6106XK-11	~65	Low	TG on ghost grain boundaries + low density of IG	0.5-1.5 µm spacing on IG boundaries

Specimens

Specimen Design

Active, constant load testing of round tensile specimens was selected for SCC initiation studies. A tensile specimen produces a uniaxial stress state, the gauge region is accessible allowing control over the surface microstructure, various types of micro/macroscopic defects can be generated and there are several ways to produce specimens with well-known amounts of uniform plastic strain. In addition, prior work at KAPL [8] has shown that DCPD can be effectively used to detect crack initiation. Several factors played into the specific design of the tensile specimens employed for SCC initiation testing [3], the most important was maximizing the ability of DCPD to detect crack initiation. The DCPD signal is affected not only by crack growth, but also by elastic and plastic strains including creep. Initiation tests are typically conducted at the yield stress or very near the yield stress where small amounts of creep occur at PWR primary water temperatures. To reduce the magnitude of the creep contribution to the DCPD signal, the gauge length was kept as short as possible while allowing a sufficient number of grain boundaries to be exposed. The short gauge length also played favorably for the desire to be able to fully survey the specimen gauge surface for cracks by SEM in a reasonable length of time. This is of importance because it is critically important to understand crack nucleation and short crack growth mechanisms.

The effect of resistivity change on the DCPD signal for nickel-base alloys exposed to PWR relevant temperatures was measured and subtracted from the gauge signal. This was accomplished by monitoring a larger diameter region of the specimen where the stress is approximately 15-25% of the gauge stress (depending on gauge diameter). For this low stress region, neither crack initiation nor any substantial amount of creep will occur and the inherent resistivity change of the material can be measured. The specimen dimensions along with a photo of the specimen are shown in Figure 4. After taking into account all design considerations, a 30.5 mm tall tensile specimen with a 4.0 mm gauge length was selected.

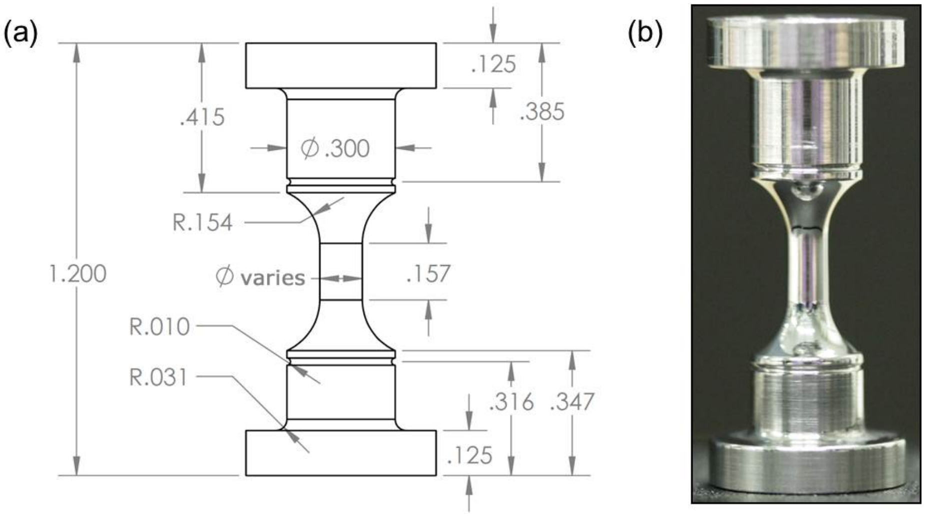

Figure 4. PNNL initiation specimen design. Gauge diameter is selected based on material strength and can be varied from 2.75-4.5 mm and the gauge length is 4.0 mm. Overall height is 30.5 mm (1.2 inches).

Specimen Preparation

Materials were tested in either the as-received (AR) or a cold-worked (CW) condition. Cold working was achieved either by cold tensile straining or cold rolling. Cold rolling performed on the plate material was done such that the rolling direction was the same direction as the original plate processing direction. Specimens taken from CRDM tubing were cut with the gauge axis parallel to the CRDM tubing axis. The gauge axis of specimens cut from the plate material was parallel to the "S" direction relative to the plate processing. Prior to insertion of the specimens into the autoclave, the gauge section either was polished to a 1 µm finish or was rough ground. A "C" finish used for some of the specimens attempts to emulate the surface damage layer created by typical service component grinding operations [7]. Application of the surface damage was achieved by applying various grinding tools to the gauge section while rotating the specimens in a lathe. Grinding tools that have been used include wood-backed sandpaper of various grits and a rotary tool with different roughness grinding disks. In order to obtain the 1 µm finish, pieces of gradually finer SiC paper (400 to 600 grit) was used followed by polishing cloth (on which 6 µm then 1 µm diamond paste was evenly spread) with a width a little wider than specimen gauge length was firmly adhered to a wooden stick. This tool was then moved systematically with a controlled load applied by hand across the gauge section with the specimen spinning at 200 revolutions per minute on a lathe. Each grinding or polishing step normally lasted 30 s to 2 min while lubricant oil was dripped onto the tool whenever necessary. After each step, the specimen was rinsed in dish soap water and then the gauge surface was checked using an optical stereoscope. Upon completion, the specimen was sonicated twice in dish soap water, once in 2% ethanol and then dried. SEM surface and cross-section observations of the

1 µm finish and the 60 grit finish applied to a CW material are shown in Figures 5, 6 and 7, respectively.

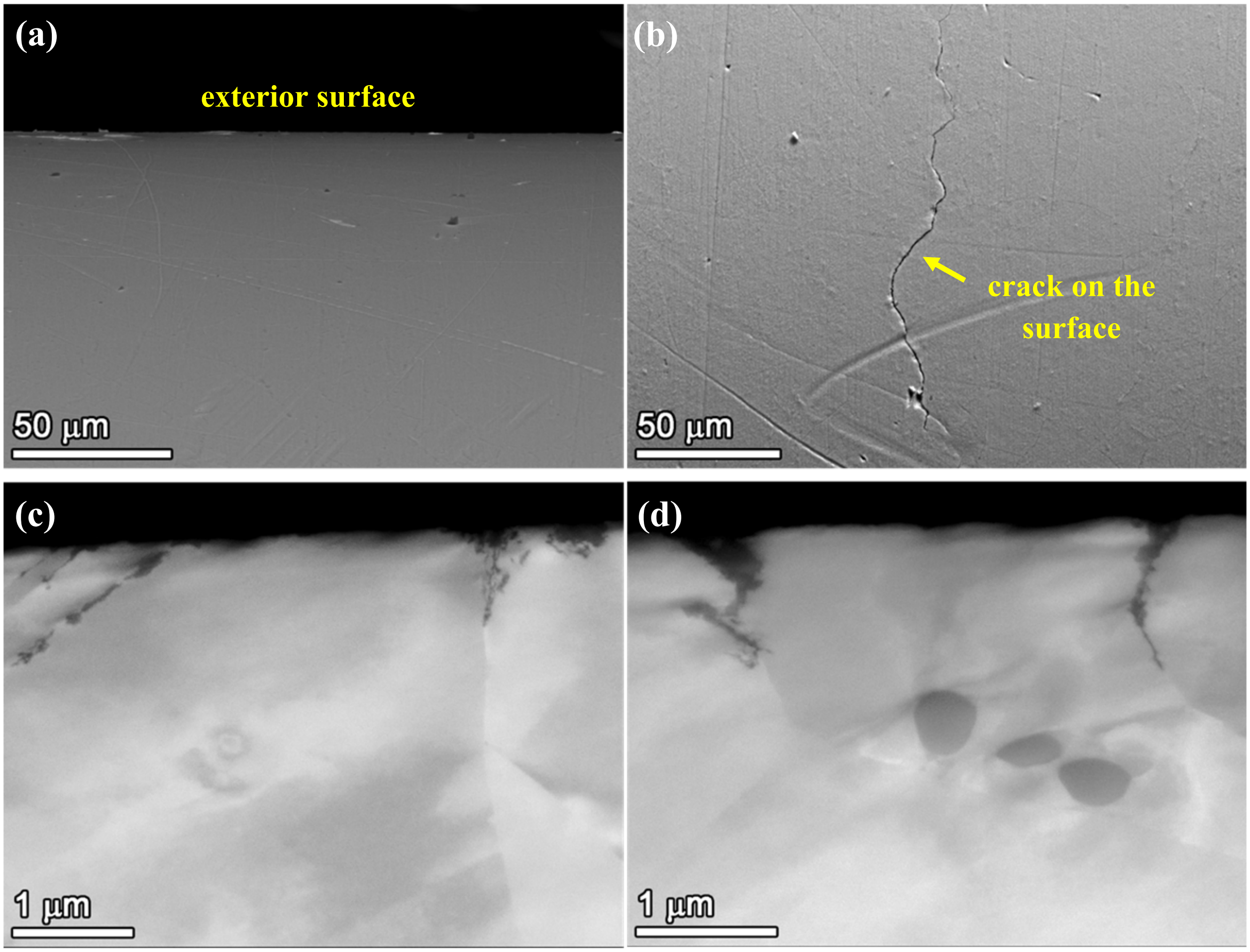

Figure 5. (a,b) SEM secondary electron (SE) images showing the surface and (c,d) BSE images showing the cross-section of a 1 µm surface of a CW material after exposure.

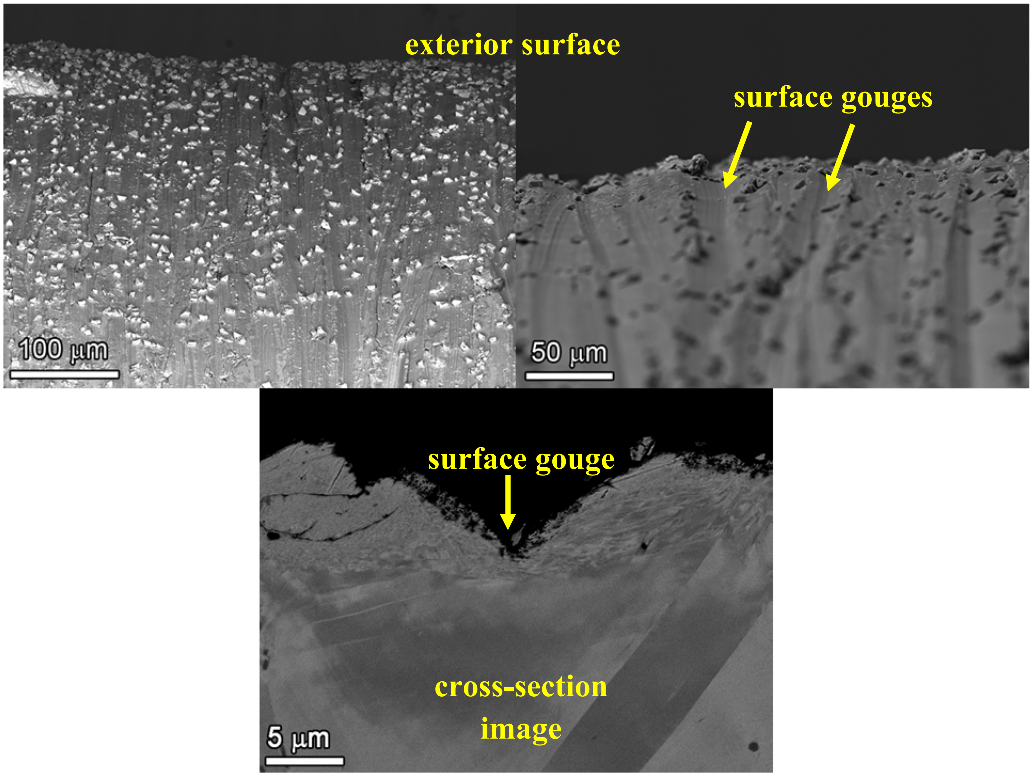

Figure 6. SEM-SE (upper) and BSE (lower) images showing the surface and cross-section of a 60 grit surface of a CW material after exposure.

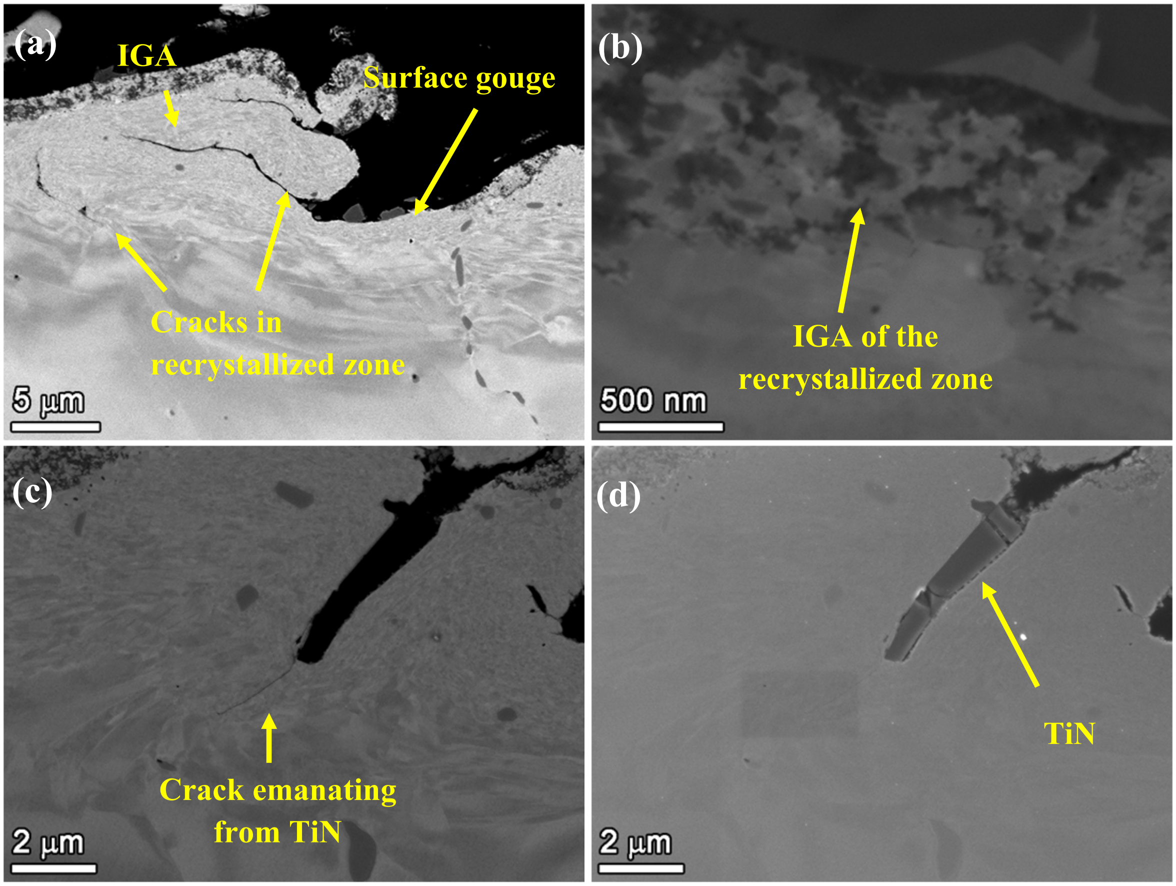

Figure 7. SEM-BSE images of a ground alloy 600 cross-section sample showing sub-surface microstructures and oxidation morphologies. (a, b) The surface is comprised of a recrystallized zone of nanocrystalline grains. Once exposed, this surface slowly corrodes. Random cracking within the nanocrystalline zone was observed and was most likely imparted during grinding. (c,d) Cracks were observed to emanate from TiN particles near the surface.

Generally, aggressive grinding produces a nanocrystalline layer (Figures 6 and 7) that promotes corrosion across the entire surface and delays water access to bulk grain boundaries. This has been found to have a small effect on initiation times as discussed later. In comparison, a highly polished surface ensures that all grain boundaries reaching the surface are immediately exposed to water. From a testing perspective, a ground surface impairs observation of surface cracks due to rough surface and microscale fold-over that often have a crack-like appearance. A polished surface eliminates these complicating factors and enables a better visual (optical, SEM) assessment of IGA and SCC initiation as a function of the material, environment and test conditions. Materials and conditions for each specimen can be found in Table 3.

Table 3. Summary of Alloy 600 SCC Initiation Test Specimens

Spec. ID	Material Type	Heat Number	CW level	Finish
IN002	Plate	NX6106XK-11	18%CTS	1200 grit
IN003	Plate	NX6106XK-11	18%CTS	1 µm
IN016	Plate	NX6106XK-11	19%CR	1 µm
IN017	Plate	NX6106XK-11	19%CR	60 grit
IN018	Plate	NX6106XK-11	19%CR	60 grit
IN022	Service CRDM	M3935	20%CTS	1 µm
IN052	Plate	NX6106XK-11	8%CTS	1 µm
IN023	CRDM tube	93510	5-7%CTS	1 µm
IN048	Service CRDM	M3935	AR†	1 µm
IN049	Service CRDM	M3935	AR	1 µm
IN050	Service CRDM	M3935	AR	"C"
IN013	Plate	NX6106XK-11	AR	1 µm
IN014	Plate	NX6106XK-11	AR	60 grit
IN015	Plate	NX6106XK-11	AR	60 grit
IN045	CRDM tube	93510	AR	1 µm
IN046	CRDM tube	93510	AR	1 µm
IN047	CRDM tube	93510	AR	"C"

† AR = as-received condition, no cold work. CTS = cold tensile strained. CR = cold rolled.

Test Methods

In-situ DCPD measurement

PNNL uses a reversing DCPD system developed by Peter Andresen of GEG. As with all DCPD measurement systems, a constant current is run through the sample. However by using a solid-state polarity-reversing switch built into the current path, potential drop is measured in both a forward and reverse current flow condition. By measuring the average of the voltage in the forward and reverse current conditions, contact voltages are eliminated from the measurement. Finite element modeling was used to visualize the voltage distribution in the interior of the specimen and on the surface. Wire attachment positions were selected at regions where voltage was relatively uniform on the surface, thus making it relatively easy to remove and reinsert specimens for testing without significantly changing the DCPD voltage values. Figure 8 shows the ideal voltage measurement points on the specimen. As noted in the figure, voltage is monitored across both the gauge region and a reference region with a larger diameter where stresses are much lower. The gauge voltage is sensitive to multiple phenomena including cracking, elastic and plastic strain, and resistivity evolution of the material while the voltage across the reference region will be primarily sensitive to resistivity evolution and a smaller amount of creep. This reference measurement is used to subtract out resistivity drift from the gauge voltage signal, leaving only cracking and some creep strain as contributions to the measured specimen response. While cracking and creep are both likely to be simultaneously contributing to the gauge DCPD response, the data here are presented as creep strains because it is thought that up to the point of SCC initiation, the DCPD signal will be predominantly affected by creep and any strong deviation in response from the creep strain trajectory will likely be due to crack initiation and growth.

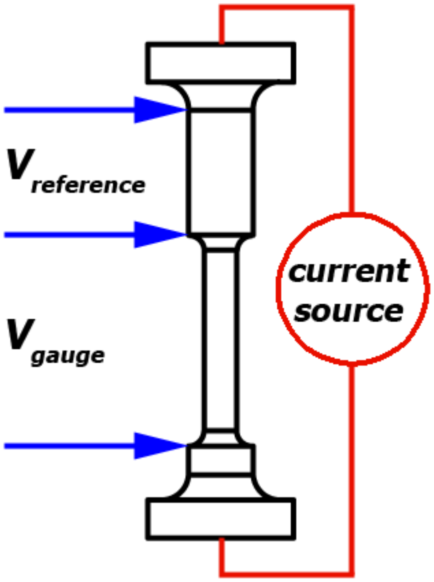

Figure 8. Sketch of the tensile specimen showing desired DCPD measurement points.

A formula for strain as a function of voltage starts first with the dependence of voltage on gauge dimensions:

$$V = \rho(L/A) \tag{1}$$

V is the measured voltage, ρ is the material resistivity, L is the distance between measurement points, and A is the cross-sectional area. Because plastic strain (including creep) is volume conservative, the relationship can be rewritten as:

$$V = (\rho/v)L^2 \tag{2}$$

where v is the volume of material between the voltage measurement points. By rearranging this equation to solve for L and inserting it into the equation for true strain ($\varepsilon = \ln(L/L_o)$), strain is obtained as a function of voltage from the following formula:

$$\varepsilon_{\text{referenced}} = \frac{1}{2}\left[\ln\left(\frac{V_{\text{gauge}}}{V_{\text{gauge}_0}}\right) - \ln\left(\frac{V_{\text{ref}}}{V_{\text{ref}_0}}\right)\right] \tag{3}$$

where $\varepsilon_{\text{referenced}}$ is the resistivity corrected creep strain, and "gauge" and "ref" are measurements across the gauge section and reference region, respectively.

Due to the specimen fixturing obstructing the idealized voltage measurement points, the actual voltage pickup points were at slightly different locations as shown in Figure 9. The deviation in voltage from idealized pickup points was assessed using finite element modeling, and a correction factor as a function of gauge diameter was determined. Further details on the development of this DCPD measurement method can be found in Ref. [3].

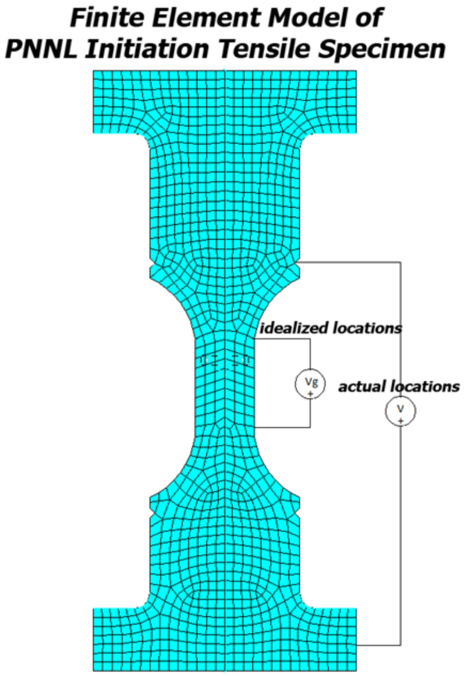

Figure 9. 2D representation of the axisymmetric finite element model. Actual gauge spot-weld locations versus idealized gauge spot weld locations are shown.

SCC Initiation Tests

Test systems built for SCC initiation studies are very similar to those used for SCC CGR studies at PNNL [9,10] and have been described in detail in a previous report [3] for this project. These systems provide a high degree of control over load, water temperature and water chemistry including B/Li content, dissolved gas content and impurity content. Important test data are continuously monitored and electronically recorded. Up to three specimens can be tested together and an example of a two specimen test is shown in Figure 10.

The SCC initiation tests were conducted in 360°C simulated PWR primary water with 1000 ppm of boron, 2 ppm of lithium and a dissolved hydrogen content of 25 cc/kg (corresponding to the

Ni/NiO stability line). All specimens were tested at or just slightly above their as-prepared yield stress under constant load. Prior to application of load, the test systems were observed for up to one week to establish stable behavior. At the start of a test, loading was achieved over a period of ~1 hour at a constant actuator displacement rate. Strain was monitored by DCPD using Equation (3), while stress was calculated from the applied load and the measured cross-sectional area. From this information, a real time stress versus strain plot was generated and was used to determine when yield had been achieved. For a multi-specimen load train where loading was in-series, each specimen was machined from the same material and same gauge dimensions, but since every specimen has a slightly different yield stress, initial loading was typically increased until all the specimens had exhibited yield as defined by deviation from linear elastic loading. An example of this is shown in Figure 11 for a 2-specimen test. In the few cases where one specimen yielded somewhat earlier than others, small amounts of plastic strain would be allowed in order to achieve yield in the other specimens. The intent was to keep this plastic strain to less than ~1%, but the plastic strain reached 2.5% for one specimen. If a test was interrupted for examination of the surface or if a specimen had exhibited crack initiation, the remaining specimens were typically taken back to their initial load upon restart of the test, again while monitoring stress versus strain.

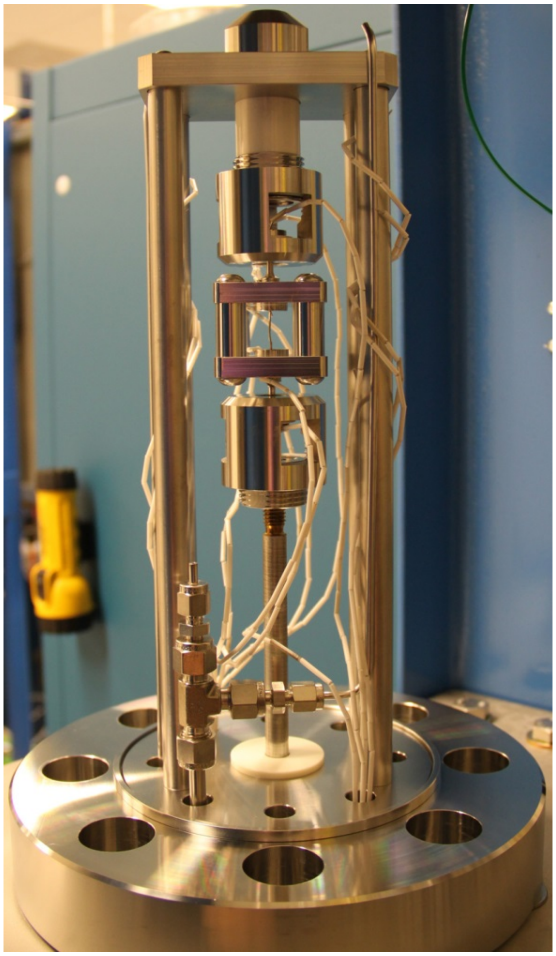

Figure 10. Crack initiation test system load train at PNNL for 1–3 specimens.

Because this research has a key interest in the formation of SCC precursors, specimens were sometimes removed from a test system prior to DCPD-indicated crack initiation so that surface microstructures could be documented. Upon completion of the surface characterization, specimens were usually put back into test.

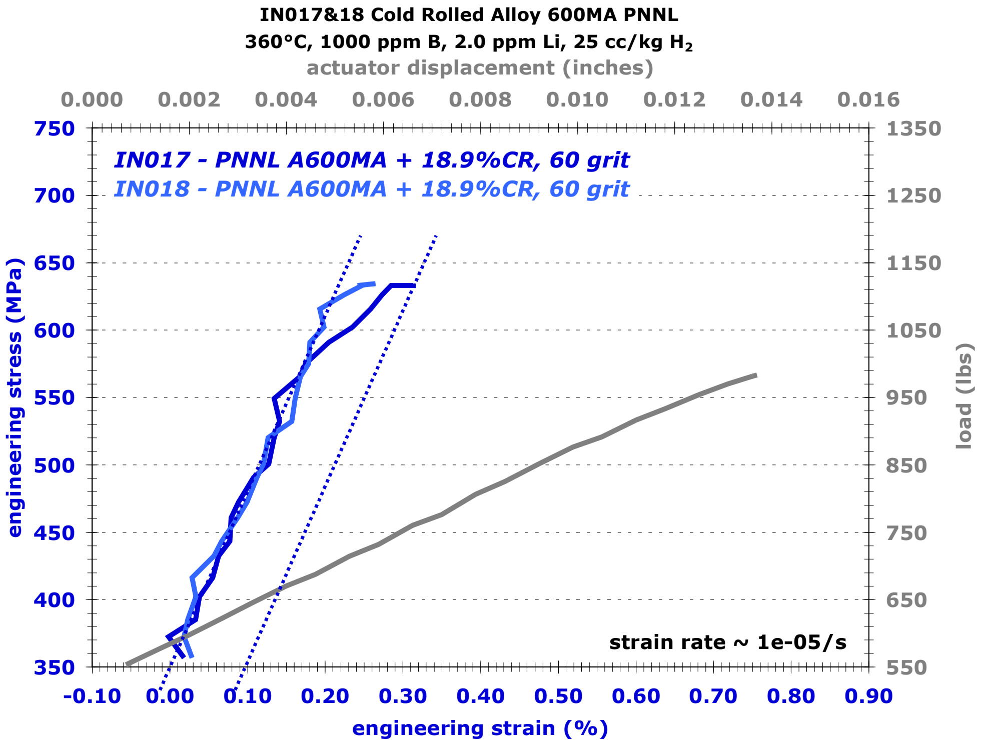

Figure 11. Example stress versus strain plot during initial loading of tensile specimens for SCC initiation testing.

Complimentary SCC Crack Growth Rate Testing

In order to better understand SCC initiation response, SCC CGR tests are being conducted on the same materials. Environmental conditions are the same as for the initiation tests with a focus on investigating propagation rates at lower stress intensities that are important during the transition to a mature growing crack after SCC nucleation.

Microstructural Characterization

Examination techniques utilized methods that were originally developed for crack observations on SCC CGR test specimens and were subsequently modified for observation of short cracks on initiation specimens. For the present study, cracks were observed by ex-situ examinations on exposed surfaces as well as in cross-section. The routine approach developed for specimen characterization mainly utilized SEM conducted on a JEOL 7600 instrument equipped with a low angle backscatter detector. Oxford Aztec software was used to automate stage movement such that the entire gauge surface could quickly be mapped enabling montages to be created.

SEM Surface Examination

Because of the highly polished condition, crack characteristics on the surface of the 1 µm finish specimens could be evaluated in detail. Examination of a specimen surface started with SEM observations of the gauge region at a variety of magnifications. Since SE imaging only collects low energy electrons generated <100 nm from the surface, smaller cracks were difficult or impossible to differentiate because they were often covered by native surface oxides on the order of 10–100 nm thick. Therefore, BSE imaging was more frequently utilized because it has a much larger interaction volume than SE imaging. Four fiducial scribe marks (90° to one another) were made at the button ends of each specimen to keep track of the specimen orientation. Each of the four orientations was then mapped at higher accelerating voltages (20–30 kV) taking advantage of the larger interaction volume of the beam (on the order of micrometers). Figure 12 provides an example of the mapping of the gauge surface of a 1 μm finish CRDM specimen. By this methodology, crack surface length and corresponding location were measured with high accuracy each time specimens were removed from testing.

SEM Cross-Section Examination

Based the cracks observed during the final surface examination, all the specimens were sectioned in two pieces longitudinally (along the length of the specimen) at a location that intersected the highest density of cracks on either side. The cross-sections were then hand polished to a colloidal silica finish and examined using low-kV (~5 kV) BSE imaging. Serial polishing was iteratively performed in this way to allow mapping the depth profile of the crack. While mounting the sample in epoxy resin typically produces a much more uniform polish surface with minimal polishing damage, it was determined that hand polishing was sufficient to observe small corrosion features (>10 nm in depth). By avoiding mounting the samples in resin, it was possible to relate the serial cross-section depth measurements to the position of a crack along its length on the surface of the tensile specimen and crack profile maps could be created. The ability to iteratively polish in steps as small as 50 μm enabled a high confidence in the determination of surface length versus depth ratios for a large number of cracks. An example is shown in Figure 13, highlighting a long surface crack intersected six times by serial polishing and the corresponding crack morphology in the cross-section after each polish. This procedure was performed repetitively to document as many cracks as possible, especially those with a longer length and wider opening on the surface.

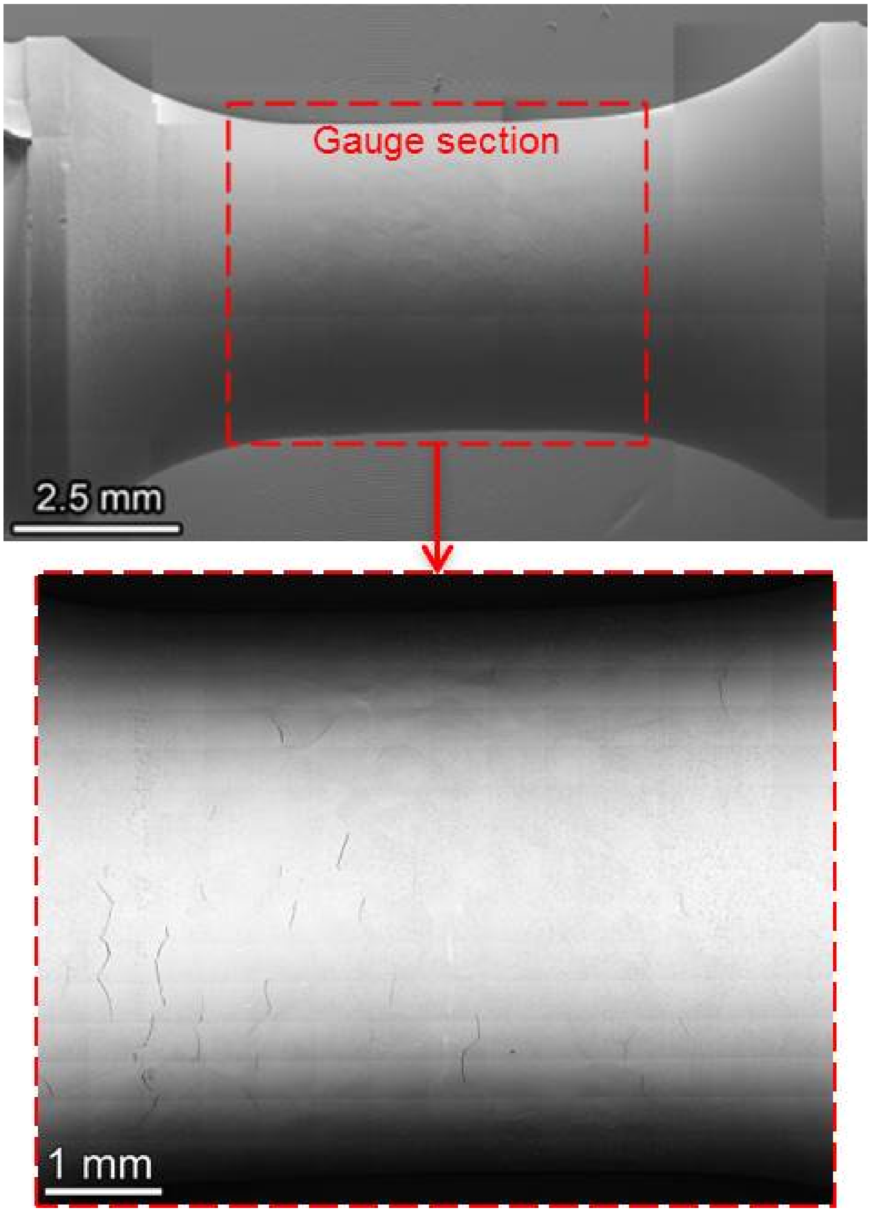

Figure 12. SEM-SE (upper) and BSE (lower) montage images showing IG cracks on the gauge section of a 1 µm finish CRDM specimen (IN048).

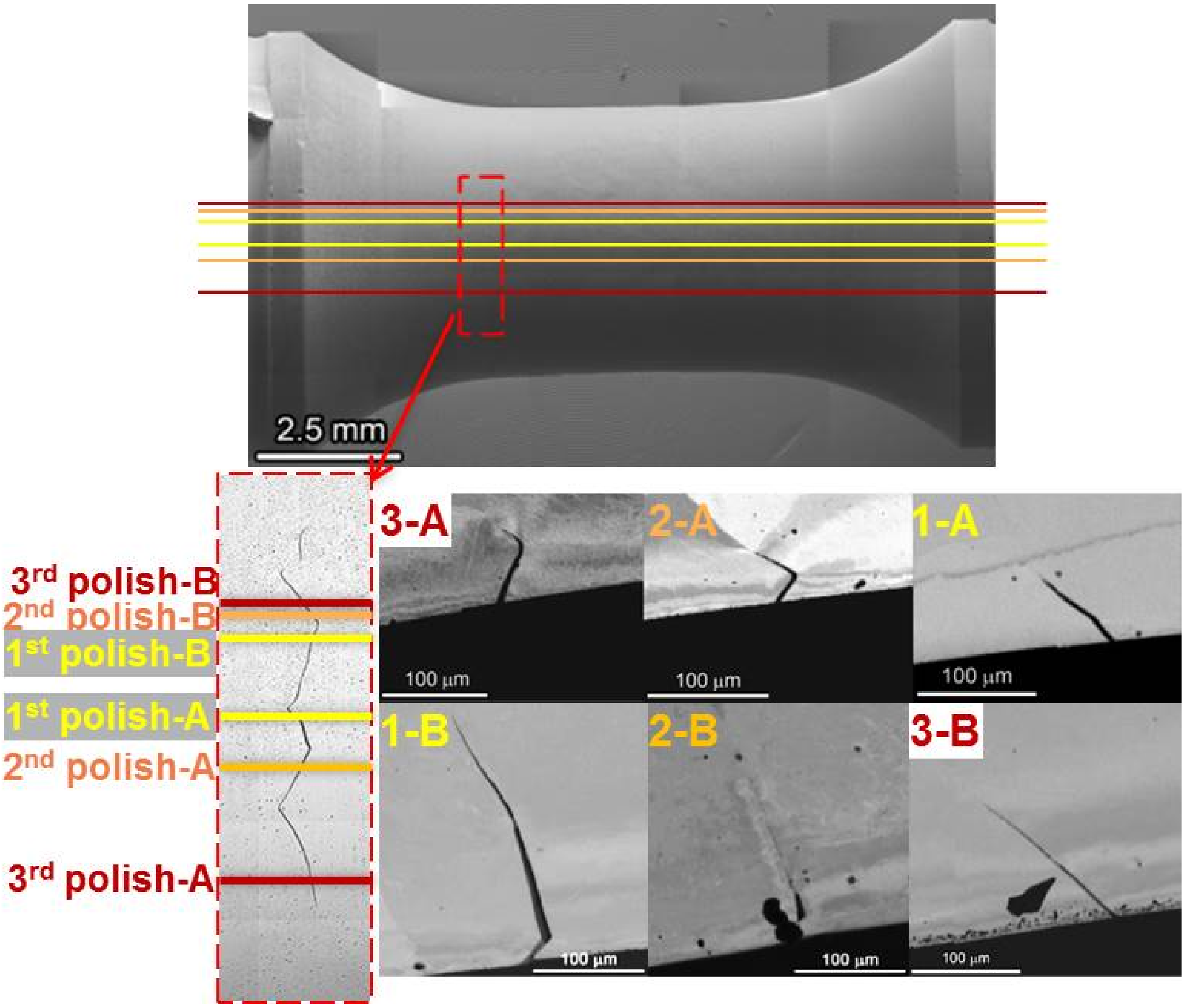

Figure 13. SEM-SE (upper) and BSE (lower left) montage image of the same specimen (IN048) shown in Figure 12, with lines marking the position of individual cross-sections and the thickness removed after iterative polishing.

SCC Initiation Tests on Alloy 600 Materials

Alloy 600 SCC Initiation Measurements

The latest data obtained on SCC initiation for three MA alloy 600 heats are summarized in this report. Materials were tested in their AR non-CW condition and with up to 20% cold work applied either by cold tensile straining or cold rolling. Results of ongoing SCC CGR tests on some of these same materials are also presented to help clarify the SCC initiation response.

SCC nucleation was readily detected by DPCD in the highly CW specimens that exhibited a smooth but very rapid transition to a higher indicated apparent strain rate over a period of 10's of hours (recognizing that the higher strain rate is due to rapid crack growth rather than crack extension). An example is shown in Figure 14 for two 18%CTS specimens. More lightly CW materials exhibited a more gradual transition to a higher indicated strain rate with the change taking place over 100's of hours as can be seen for a 7%CTS specimen in Figure 15. However, AR materials exhibited some complexity in DCPD response. As with the CW materials, some AR materials such as two NX6106XK-11 plate specimens with a ground surface have exhibited a very gradual upward trend in referenced strain rate (Figure 16). The IN014 plate specimen began showing an increasing response at ~6925 hours with this transition to higher strain rates continuing over the next ~1000 hours. In the final 1000 hours of the test, the DCPD indicated strain rate increased by 60%. The IN015 plate specimen exhibited a transition in DCPD response at ~7480 hours, and over the final ~500 hours of the test, the DCPD indicated strain rate increased by ~170%. Other AR materials have exhibited a distinctly different response that consisted of a step change in referenced strain as shown in Figure 17 for a 1 µm finish service CRDM material (M3935). The cause for this step change response is still under investigation, and whether a specimen that exhibits a step change in response will eventually also show an increasing strain rate has yet to be studied at PNNL. However, researchers at KAPL have observed some specimens exhibiting a step change in strain that was eventually followed by an increasing strain rate [8]. This response for the AR materials is discussed further later.

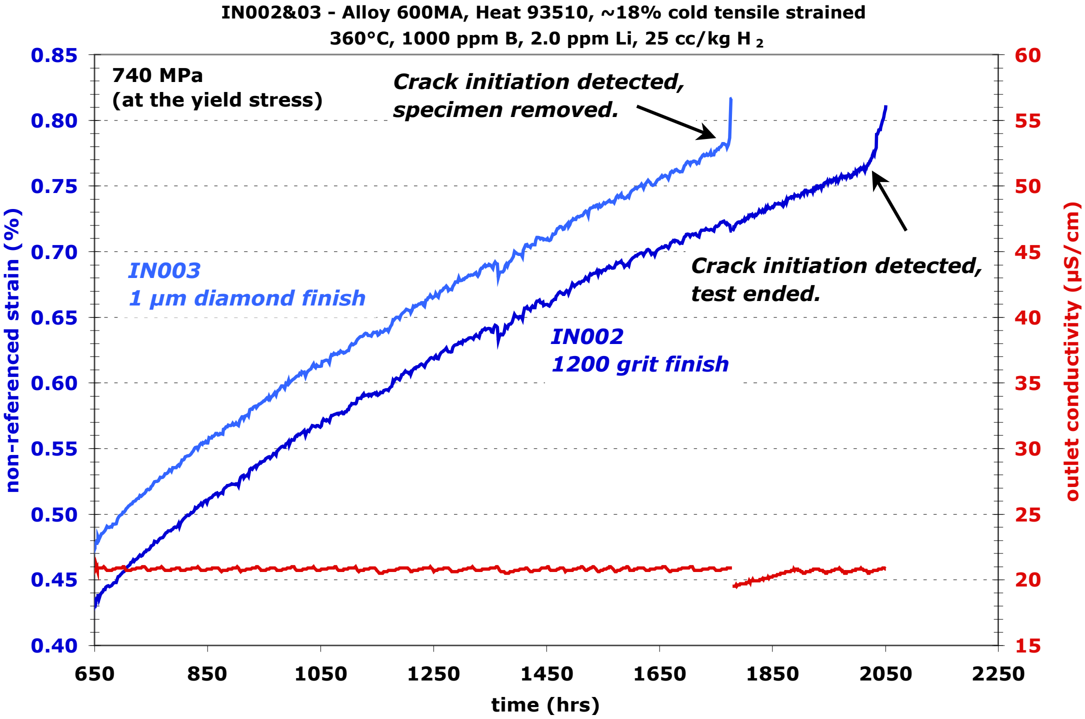

Figure 14. SCC initiation response of two ~18%CTS alloy 600 plate specimens showing a smooth but sharp transition to a higher indicated strain rate.

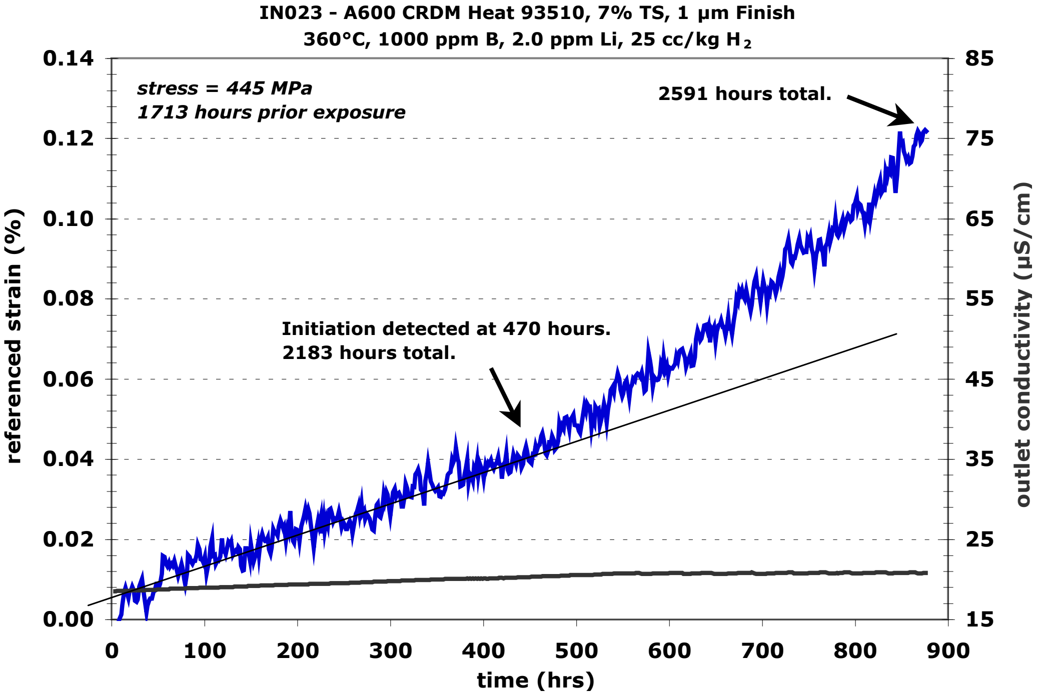

Figure 15. SCC initiation response for a ~7%CTS alloy 600 CRDM specimen showing a sharp but continuous transition to a higher indicated strain rate.

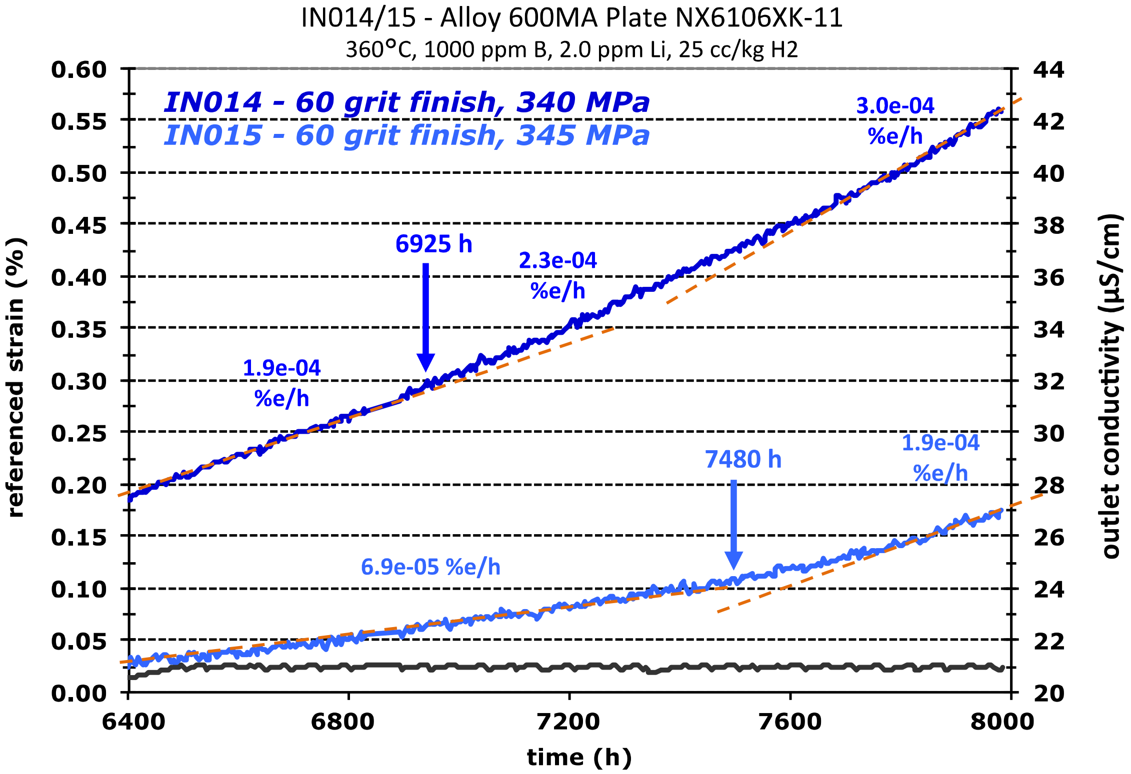

Figure 16. Observed DCPD response of two AR alloy 600 plate specimens with the estimated time of SCC initiation identified by arrows at the first change in slope.

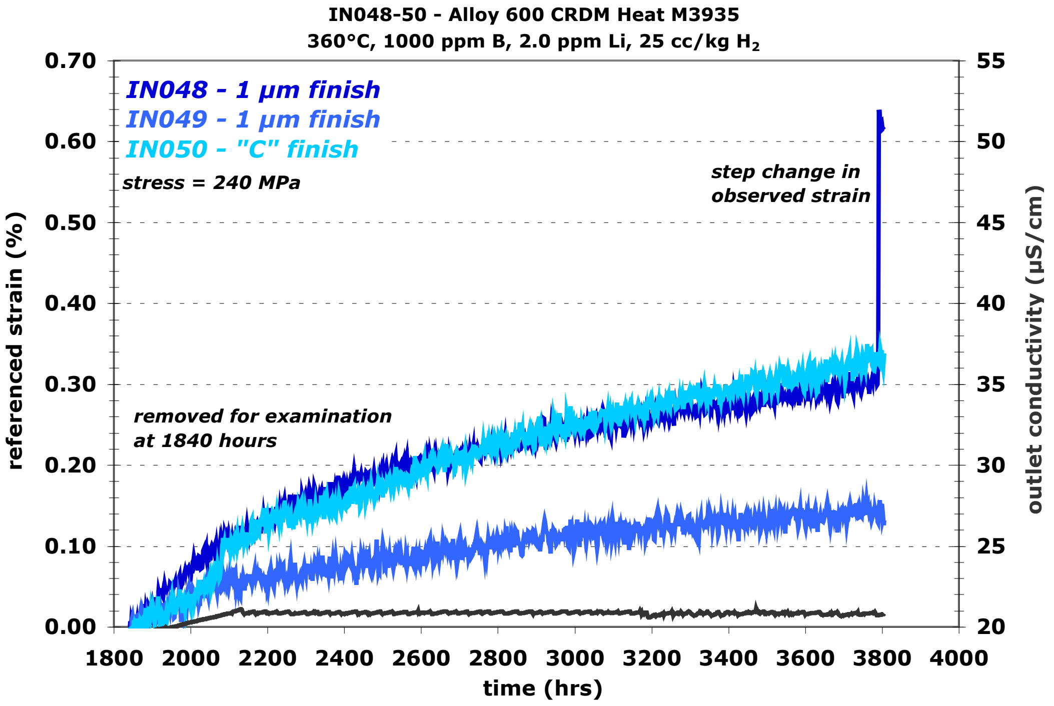

Figure 17. Observed DCPD response of AR alloy 600 CRDM (M3935) specimens.

SCC initiation times are summarized in Table 4. As noted in the table, two tests were stopped before a clear indication of SCC initiation by DCPD. The 20%CTS service CRDM specimen (IN022) was stopped early due to a higher than expected indicated strain rate from the very start of the test (Figure 18). This MA material exhibited very high SCC crack growth susceptibility in the AR, non-CW condition [5,6]. Post-test analysis of the SCC initiation specimen revealed significant cracking with the primary crack having a peak depth of 350 µm, comparable to that for other CW specimens that showed clear DCPD-indicated crack initiation. This suggests that either SCC initiation detection was imminent or that crack nucleation and growth occurred almost immediately from the start of the test. Based on the crack depth observations, the time at which the test was stopped (385 h) was considered to be a reasonable estimate of the SCC initiation time. The other specimen that was stopped before an indication of SCC initiation was a specimen made from the service CRDM material in the AR condition (IN049). This specimen is nominally identical to IN048 that underwent a step-change in DCPD response. The decision was made to discontinue testing IN049 so that its crack morphology could be compared to IN048. Comparative examinations of these two specimens are ongoing with the most current results presented later.

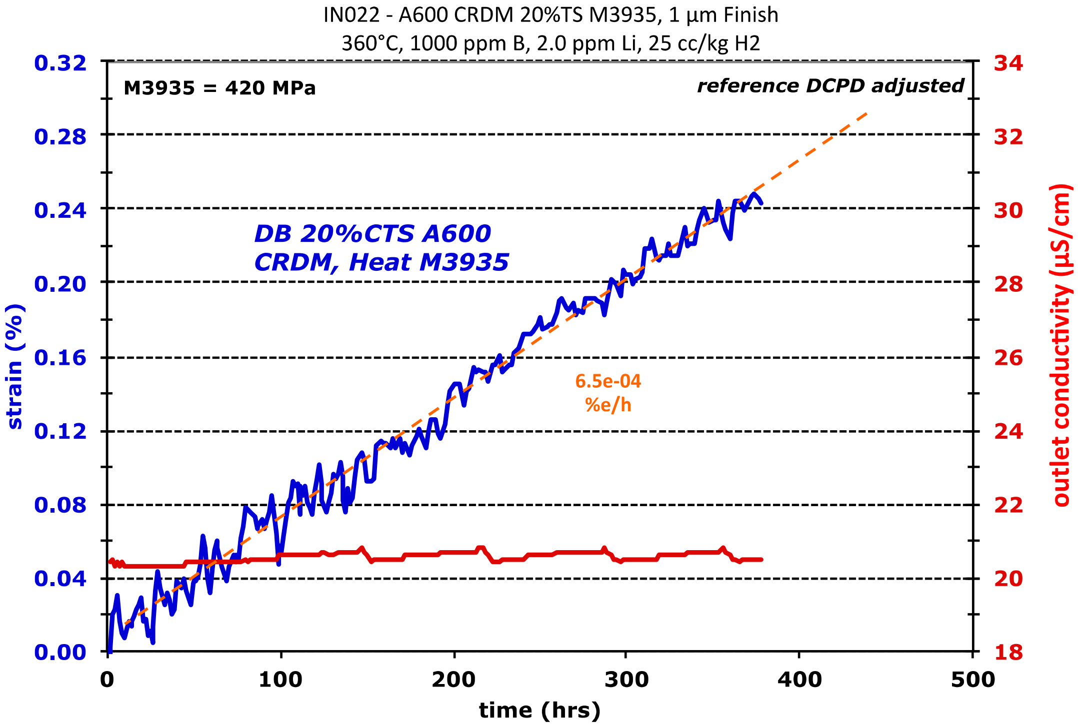

Figure 18. DCPD response of the 20%CTS service CRDM specimen IN022.

Table 4. Summary of specimen initiation response.

Spec. ID	Material Type	Heat Number	CW level	Finish	Applied Stress‡ (MPa)	Initiation Time (h)
IN002	Plate	NX6106XK-11	18%CTS	1200 grit	740	2025
IN003	Plate	NX6106XK-11	18%CTS	1 µm	740	1775
IN016	Plate	NX6106XK-11	19%CR	1 µm	610	1522
IN017	Plate	NX6106XK-11	19%CR	60 grit	610-634	1787
IN018	Plate	NX6106XK-11	19%CR	60 grit	610-634	1715
IN022	Service CRDM	M3935	20%CTS	1 µm	420	385*
IN052	Plate	NX6106XK-11	8%CTS	1 µm	435	1250
IN023	CRDM tube	93510	5-7%CTS	1 µm	425-445	2183
IN048	Service CRDM	M3935	AR†	1 µm	240-255	3775
IN049	Service CRDM	M3935	AR	1 µm	240-255	3795*
IN050	Service CRDM	M3935	AR	"C"	240-255	NI** (5792)
IN013	Plate	NX6106XK-11	AR	1 µm	330	5942
IN014	Plate	NX6106XK-11	AR	60 grit	330	6925
IN015	Plate	NX6106XK-11	AR	60 grit	330	7480
IN045	CRDM tube	93510	AR	1 µm	290	NI (4100)
IN046	CRDM tube	93510	AR	1 µm	290	NI (4100)
IN047	CRDM tube	93510	AR	"C"	290	NI (4100)

‡ The applied stress is the yield stress of the specimens.

† AR = as-received condition, no cold work. CTS = cold tensile strained. CR = cold rolled.

* Test stopped before clear indication of SCC initiation. Post-test analysis revealed significant cracking.

** NI = no initiation, ongoing test. Time in parenthesis is the total accumulated time.

Effect of Cold Work on SCC Initiation Time

Testing is still underway, but a sufficient number of tests have been completed to show key trends as a function of cold work. The relationship between SCC initiation time and applied stress is shown in Figure 19 and for the level of cold work in Figure 20. Dashed lines in the plots are meant to bound the data and aid in visualization of the initiation response. For this relatively small data set, the trend versus either applied stress (yield stress) or the level of cold work is very similar. In comparison, Etien et al. [8] have reported a much stronger correlation of SCC initiation to the level of plastic strain than to the applied stress. In the current work, materials with 7-8%CTS have initiated in less than 2200 hours, and higher levels of cold work or stress have caused only a small additional reduction. Initiation times for the AR non-CW materials range from ~3800 h for the highly susceptible service CRDM material to ~7500 h for the plate material within this range of values roughly 3-4x higher than the 7-8%CTS material. Whether analyzed as a function of stress or cold work level, the data show a substantial reduction in SCC initiation time between no cold work and low levels of cold work. Crack growth testing is showing a similar strong effect of cold work on SCC. As shown in Figure 21, the plate heat in the AR non-CW condition exhibited constant K propagation rates of $\leq 1x10^{-8}$ mm/s for stress intensities below 20 MPa$\sqrt{m}$, but SCC CGRs for the 19%CR plate were 1000-10000x higher (~$1x10^{-5}$ mm/s) at the same stress intensity (K). Further testing is needed and is underway to establish whether there is a strong sensitivity to lower levels of cold work on SCC CGRs. These current results appear to be consistent with the results of Paraventi and Moshier [11] for alloy 600, where compared to the as received (non-CR condition), a significant increase in SCC CGR was found for a 12%CR material. While these results show a strong effect of small amounts of cold work, the concurrent application of higher stress in the highly CW materials must also be having an effect. Future tests will isolate these effects by assessing the response of low and moderate CW materials at 2-3 different stress levels.

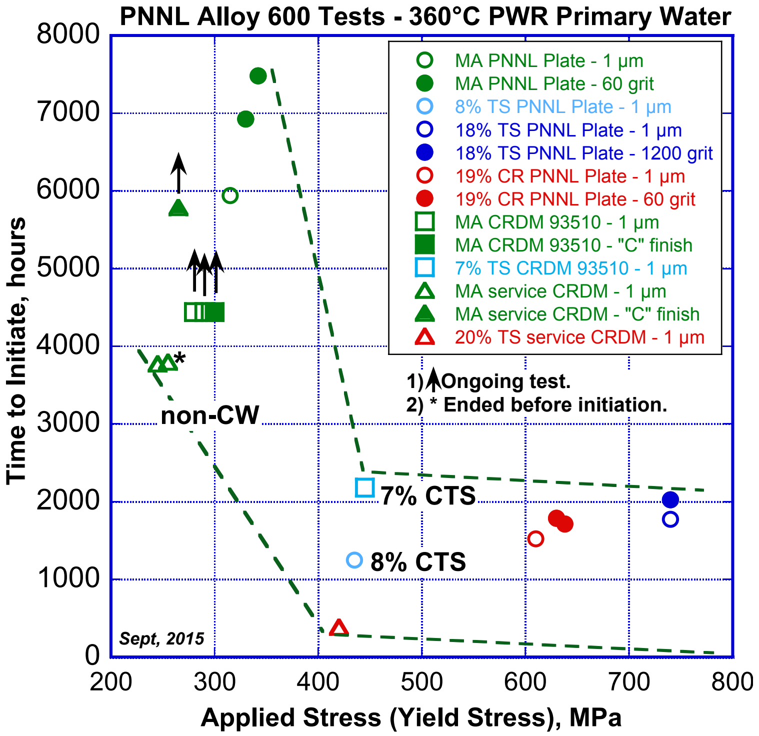

Figure 19. Measured SCC initiation time as a function of applied stress. Dashed lines are meant to bound the data and aid in visualization of the initiation response.

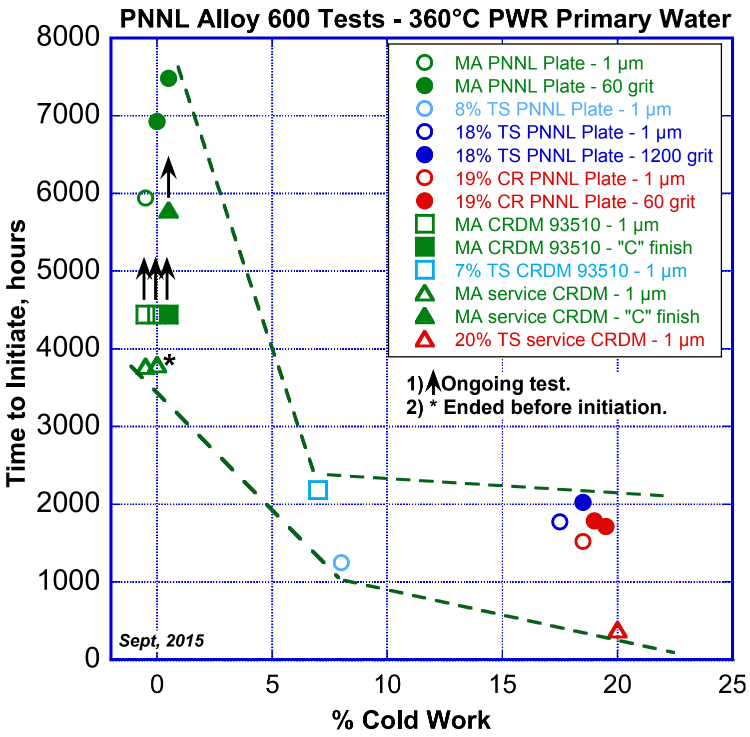

Figure 20. Measured SCC initiation time as a function of % cold work. Dashed lines are meant to bound the data and aid in visualization of the initiation response.

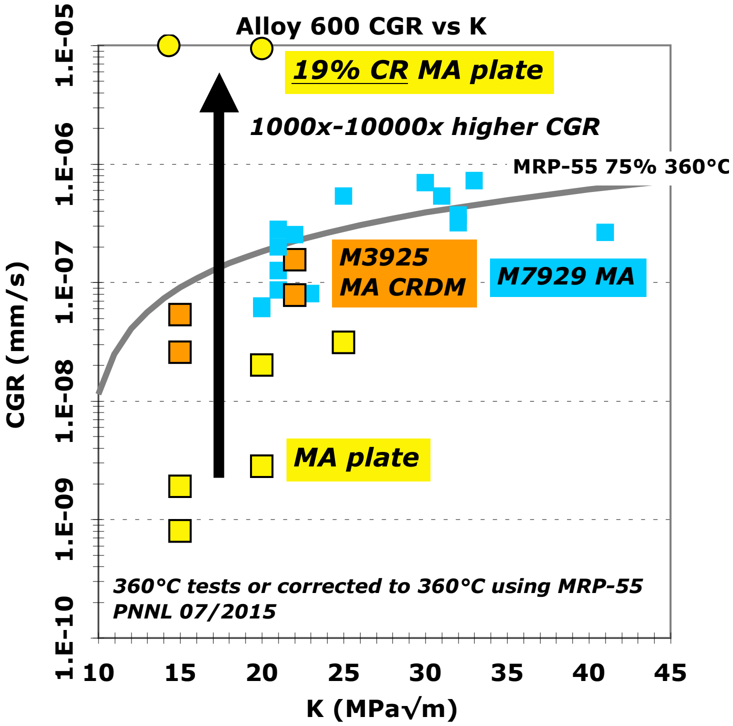

Figure 21. Measured SCC CGRs for alloy 600 materials in 360°C simulated PWR primary water. A strong effect of cold work can be seen for the MA plate heat with 1000-10000x higher CGRs for the 19%CR material versus the AR material.

Microstructural Observations of Initiated Alloy 600

Overview of SCC Initiation Microstructures

Cross-section observations of cracks in initiated specimens have revealed a range of morphologies from IGA to well developed IGSCC cracks having depths exceeding 150 µm. Examples are shown in Figure 22 for the 18%CTS plate specimen with a polished surface (IN003). IGA observed at grain boundaries along the entire length of the gauge section had depths of no greater than 5 µm, such as in Figure 22(a) and (b). Short cracks were also observed such as in Figure 22(c) and (d). For the CW materials, it appears that a few cracks eventually outpaced the others to produce a deep crack that caused the DCPD-indicated SCC initiation response. These dominant cracks were often readily identified on the surface such as shown in Figure 23 for the 8%CTS plate material (IN052). Smaller cracks were also readily identifiable on specimens with polished surfaces.

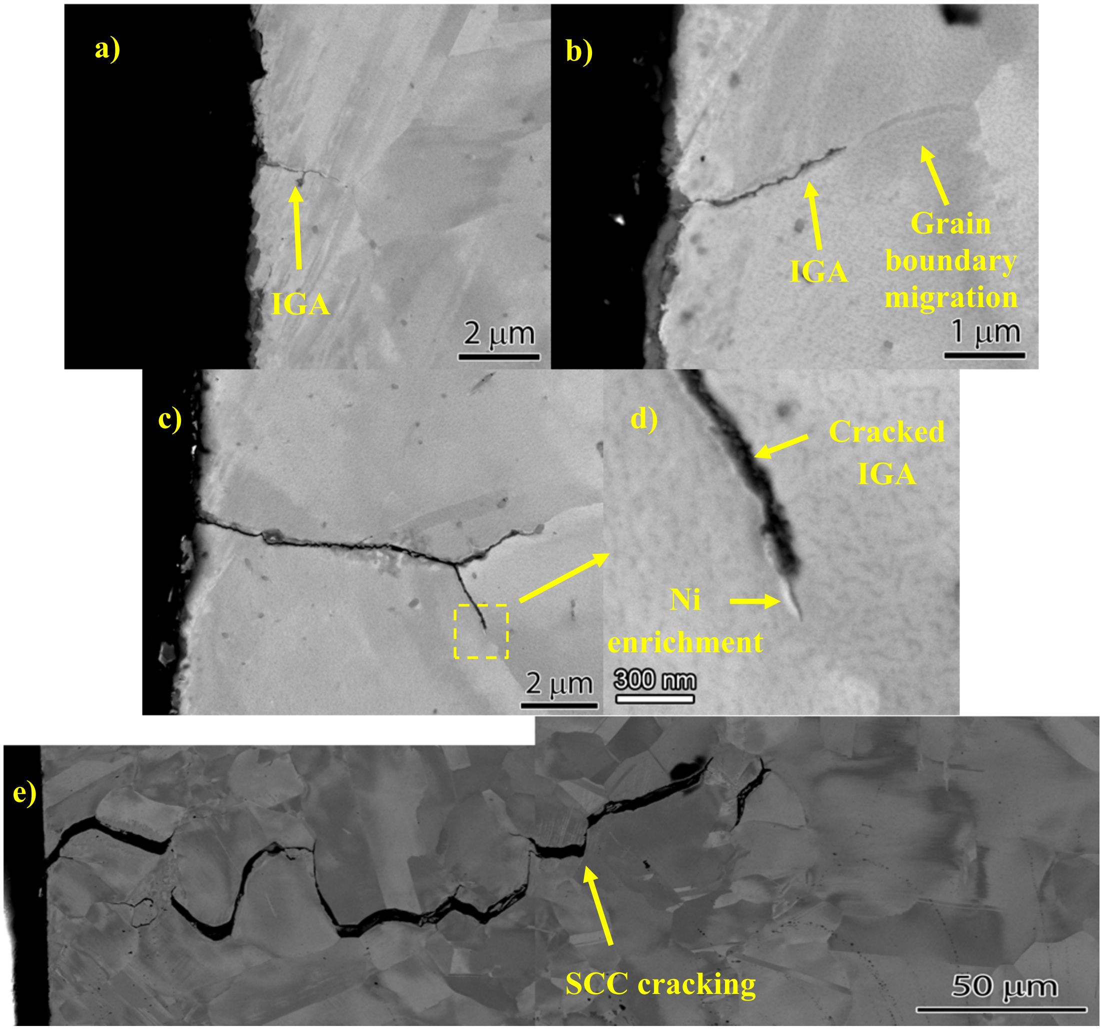

Figure 22. Range of SCC morphologies observed in cross-section for the 18%CTS plate specimen (IN003) after SCC initiation.

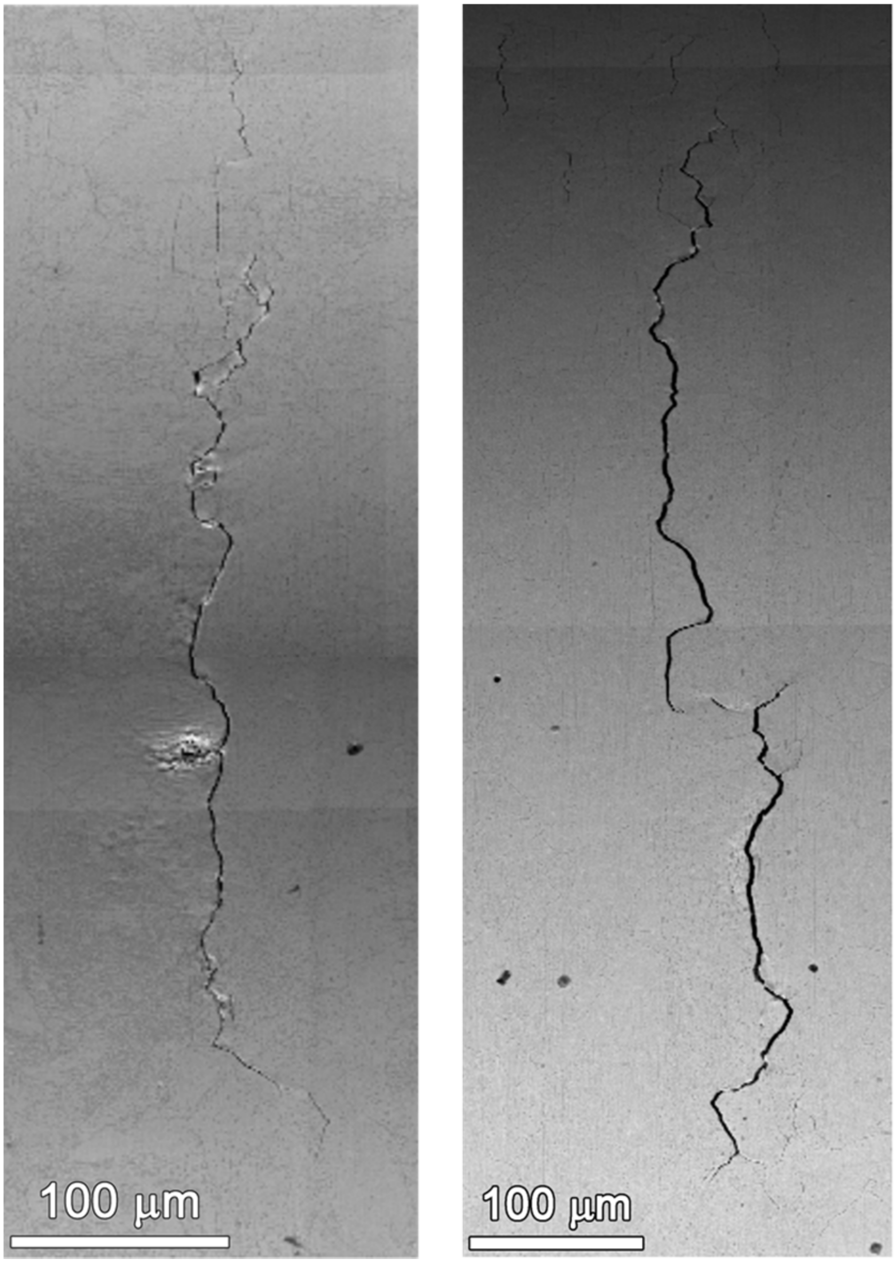

Figure 23. Dominant cracks observed on the surface of the 8%CTS plate material (IN052).

Observations of small cracks on the surface of ground specimens were much more difficult for reasons already discussed. When viewed in cross-section, IGA was observed to uniformly progress through the nanocrystalline layer on ground surfaces as shown for example in Figure 24 and eventually reach grain boundaries below the ground surface. Figure 25 suggests that by the time an increasing strain rate is detected by DCPD response, large SCC cracks would become evident even on the relatively rough surface of ground specimens. Detailed quantitative examinations are underway to characterize the crack surface length, crack depth, and crack shape for the initiated specimens. Early results on selected specimens with a 1 µm finish presented later in this report.

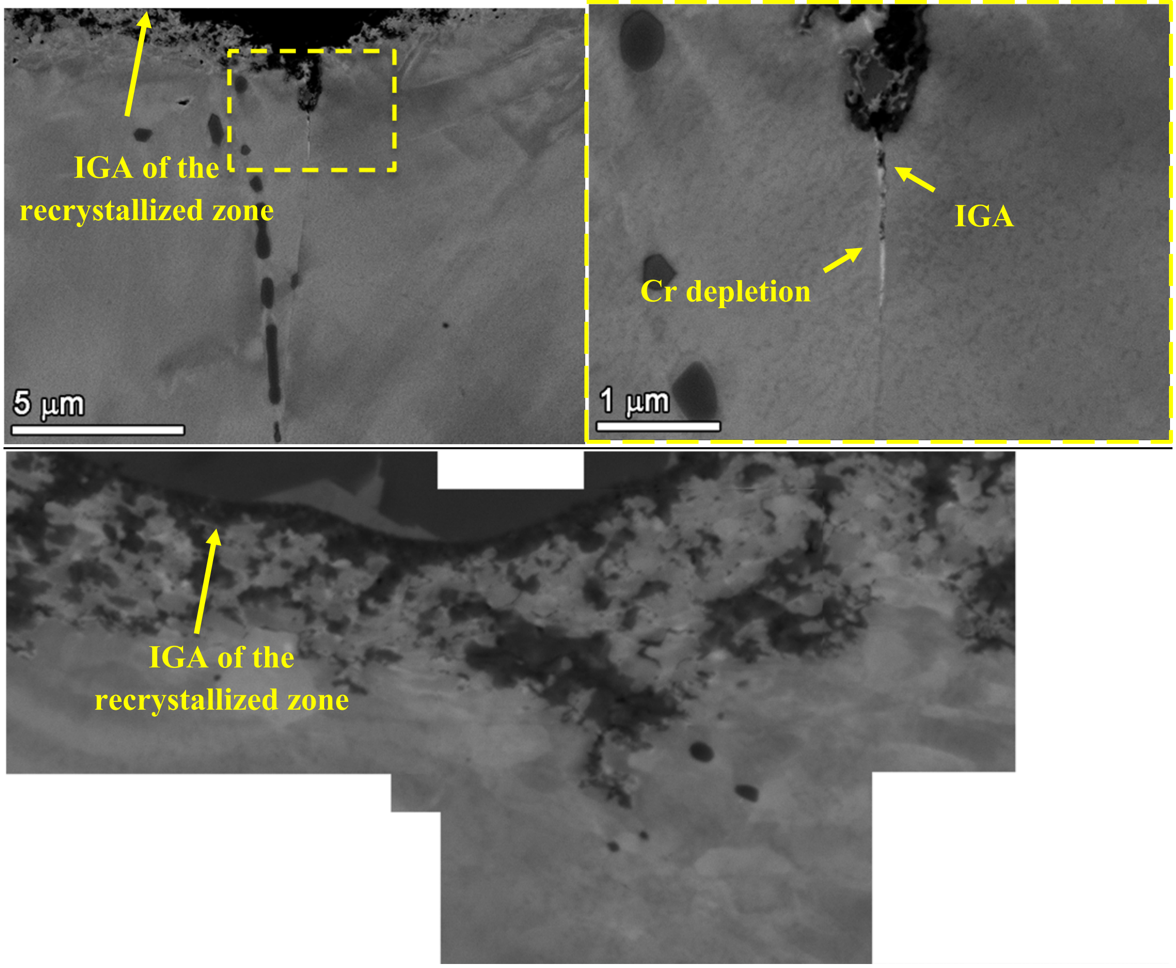

Figure 24. Corrosion through the ground surface and subsequent IGA of a bulk grain boundary for the 19%CR plate specimen IN018.

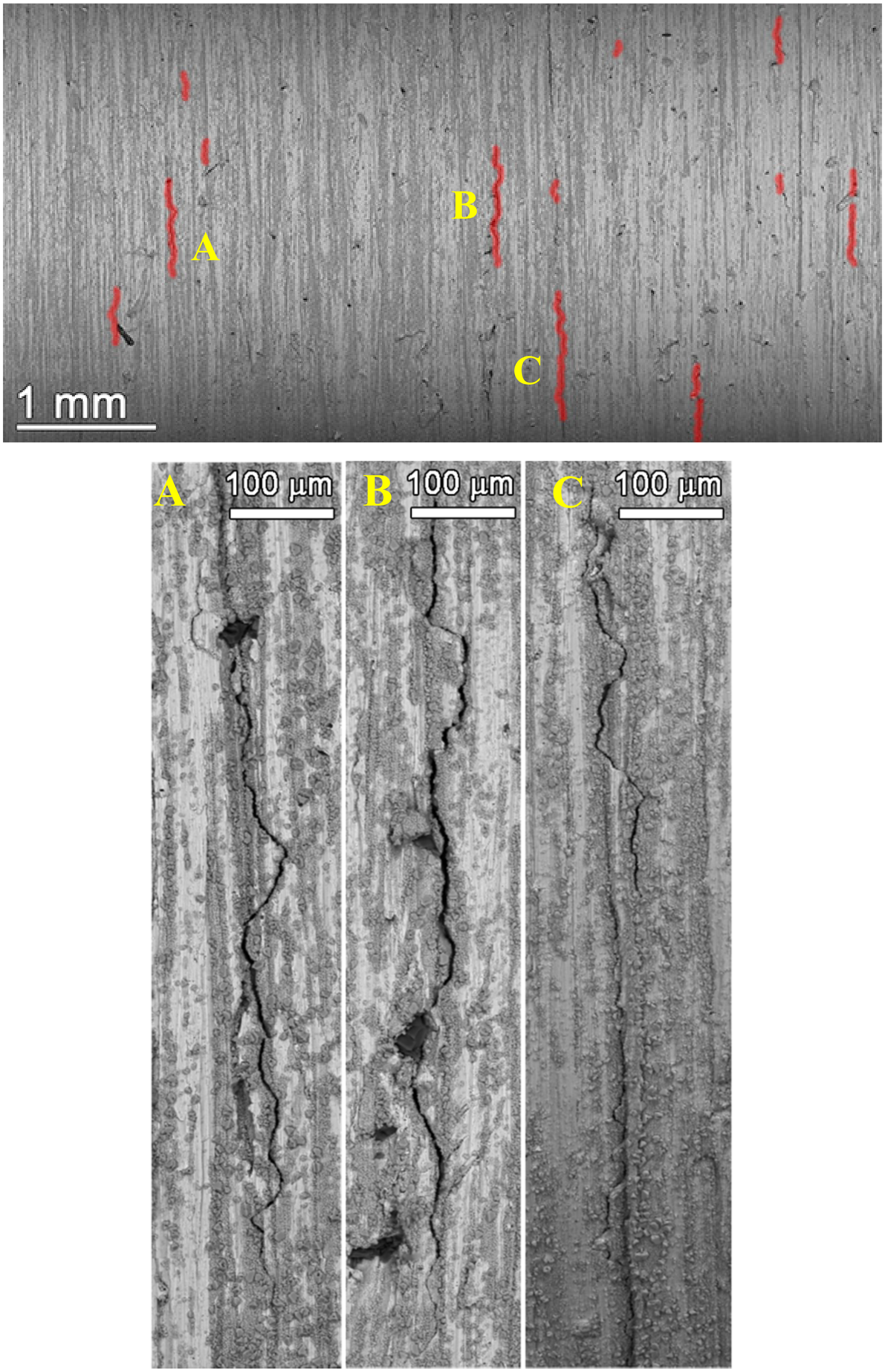

Figure 25. SCC cracks observed on the surface of IN014 (AR plate specimen) after 8008 h of exposure: (a) Large cracks are highlighted in red on the BSE montage images of part of the gauge surface, and (b) corresponding morphology of cracks A, B and C marked in (a).

Detailed Crack Morphology Investigations

The focus of this section is to present data obtained by ex-situ quantitative characterization describing the evolution of crack formation in selected alloy 600 specimens to provide information to better understand SCC initiation and link the DCPD response to crack morphologies. Detailed experimental results on three AR and two CW alloy 600 specimens from two heats that were polished to a 1 μm finish will be described. Observations will be discussed with respect to three observed phenomena: (1) the transition from precursor damage to short cracks; (2) crack growth and coalescence and (3) changes observed in DCPD strain rate response (increased strain rate and/or a step change in strain). The role of crack geometry on crack initiation and short crack growth will also be evaluated with respect to estimated crack tip K values.

Background on Analyzed As-Received Alloy 600 Specimens

Two specimens (IN048 and IN049) from the alloy 600 service CRDM heat (M3935) and one specimen (IN013) from the MA alloy 600 plate heat (NX6106XK-11) have been characterized in detail. More information on these specimens can be found in Table 4 . IN048 and IN049 were tested in-series with a third specimen of the same material, while IN013 was loaded in-series with two other initiation specimens of the same material in a second test system. After bringing the autoclaves up to target pressure and temperature, the specimens were loaded to their yield strength (initial values of ~255 MPa for IN048 and IN049, ~315 MPa for IN013) at a constant extension rate of ~10^{-5}/s and then maintained at this stress. No two specimens yielded at exactly the same load, and since it was desired to ensure that all specimens have reached their yield stress, almost all specimens were given a small amount of plastic strain at 360°C. The detailed loading condition and plastic strain for each specimen are provided in Table 5.

Table 5: Loading Conditions for SCC Initiation Tests

	Applied stress (MPa)	Plastic pre-strain (%)	Applied stress (MPa)	Plastic pre-strain (%)	Applied stress (MPa)	Plastic pre-strain (%)
	Stage* 1 (0–1840 h)		Stage 2 (1840–3806 h)			
IN048	255	0.4	240	0.6		
IN049	255	2.5	240	0		
	Stage 1 (0–3392 h)		Stage 2 (3392–4529 h)		Stage 3 (4529–6021 h)	
IN013	315	0.7	320	0.9	350	0

*The various stages in a test were separated by interruptions for surface examination.

In order to investigate the evolution of IGA and surface cracking, tests were interrupted before an indication of initiation was detected in the DCPD signal. Specimens were removed from the test systems to document surface microstructures during each interruption and then put back into test at or near the prior load. The tests were continued until an obvious change in DCPD strain rate response was detected at ~3760 hours for IN048 (Figure 26) and ~5492 hours for IN013 (Figure 27) that was in the form of a sudden DCPD-based strain jump. Test systems were then shut down after a total exposure time of 3806 hours for IN048 and IN049 and after 6021 hours for IN013. No DCPD indication of crack nucleation was identified for the IN049 specimen. So far the total number of cracks that have been measured in IN048 is 24 and IN049 is 36 for this large grained material. Many more cracks (525) have been measured in IN013 that has a much smaller grain size.

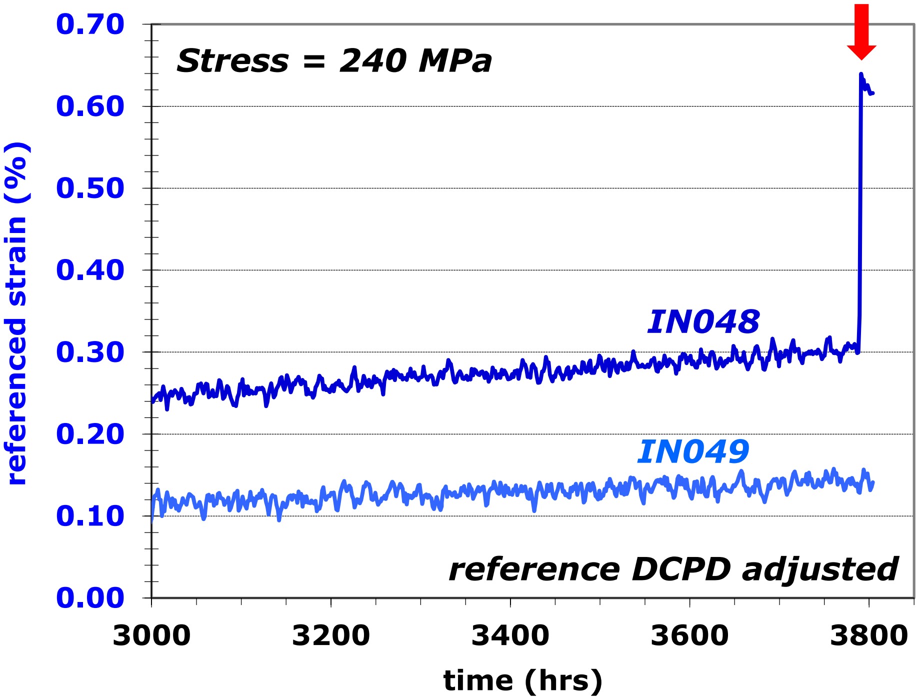

Figure 26. Referenced DCPD strain rate response for the IN048 and IN049 near the end of the tests. The step change observed in IN048 is indicated by an arrow.

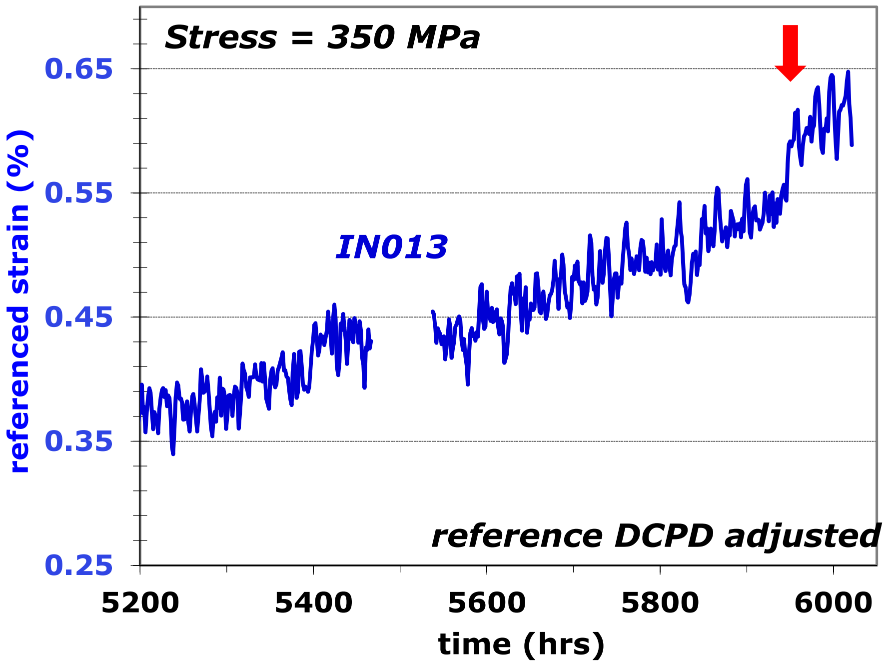

Figure 27. Referenced DCPD strain rate response for the IN013 near the end of the tests. The step change observed in IN013 is indicated by an arrow.

IGA and SCC Crack Morphologies of As-Received Alloy 600

Gauge surface characterizations of the three non-CW specimens at the first test interruption revealed tight groove features with a surface length of normally less than 1–2 grains (identified by arrows) at a large number of high energy grain boundaries as shown in Figures 28(a) and 29(a). Cross-section observation at the conclusion of the test in Figures 28(b,c) and 29(b,c) revealed that these surface features were correlated to IGA and small tight cracks, normally very shallow with no more than 5 µm in depth.

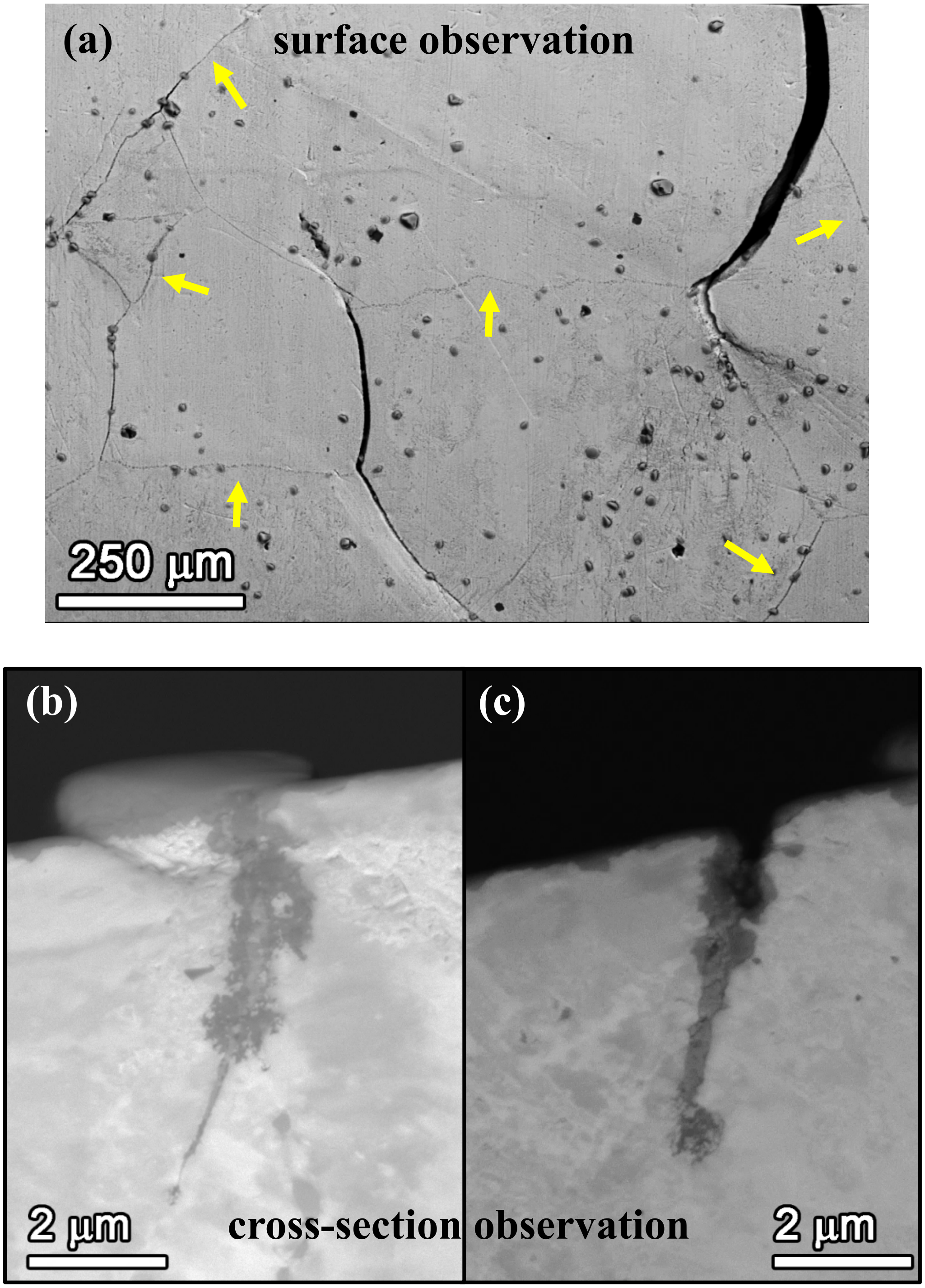

Figure 28. SEM-BSE images of the typical morphology for IGA, small tight cracks and occasional larger cracks on the IN048 surface (a). IGA and small surface cracks are identified by arrows and had shallow depths as shown in cross-section (b, c) on the CRDM specimens.

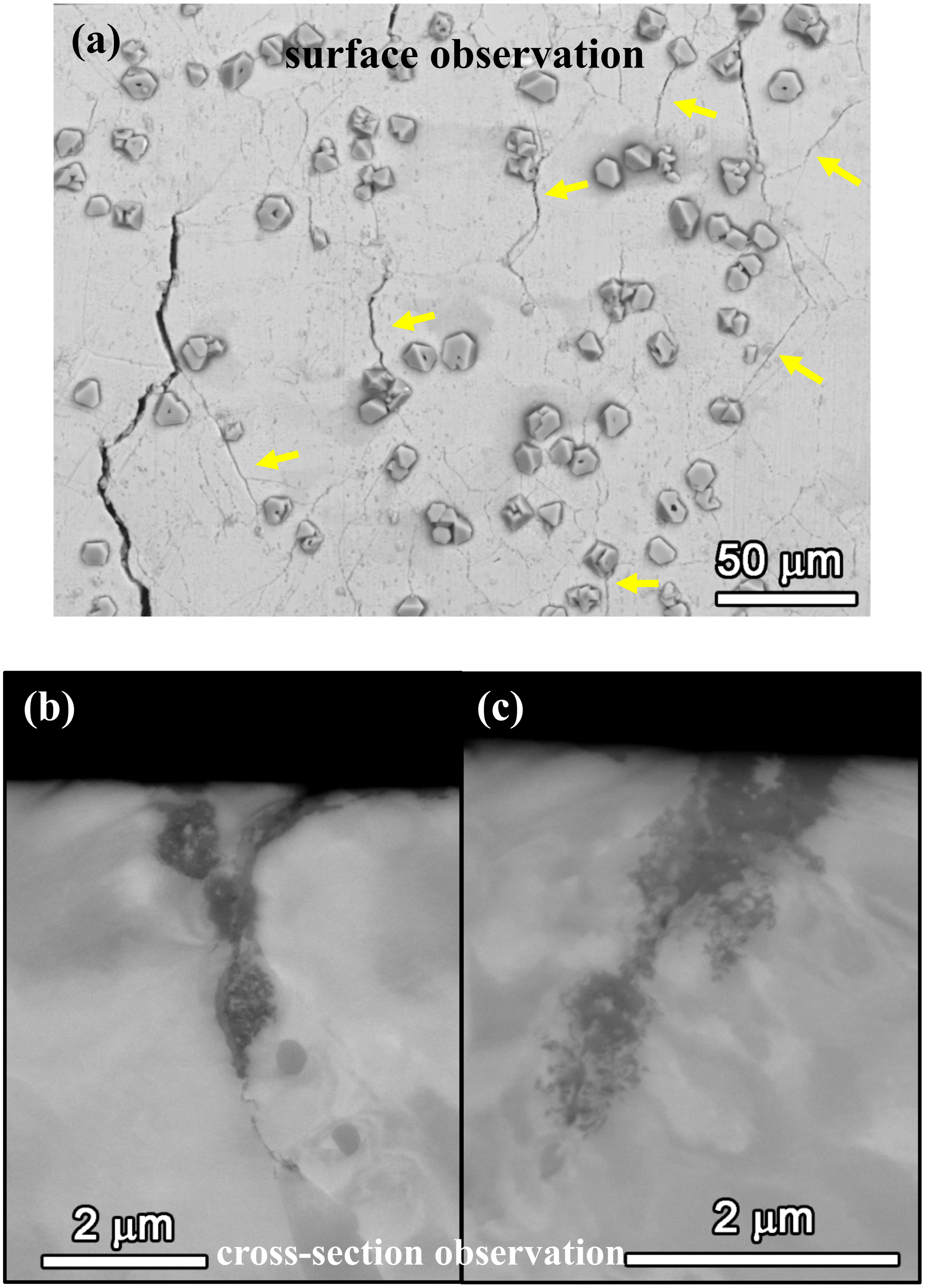

Figure 29. SEM-BSE images of typical morphology of IGA and small crack (identified by arrows) along with few larger cracks observed on the IN013 surface (a). Shallow depths for IGA and small surface cracks are illustrated in cross-section (b,c).

While IGA and small cracks described here and in the previous section generally made up 70-90% of all the cracks observed on these three specimens, some cracks with distinctly longer surface length and wider opening were found. Examples of these cracks are shown in Figures 28(a) and 29(a). By the end of the test, the longest crack reached a surface length of ~1.5 mm on IN048 and IN013 (both exhibited a DCPD jump), and ~1.0 mm on IN049 (no DCPD jump). All cracks were IG with openings tending to scale with crack depth. The deepest cracks observed so far in these specimens (examinations are still ongoing) have similar depths of ~250 µm and all have maximum openings approaching ~10 µm. Surface morphologies of these cracks are presented in Figure 30(a,c,e) with examples of the crack morphologies in depth at the location marked by the dashed red line are given in Figure 30(b,d,f). The maximum depth of each crack measured as a function of its surface length is illustrated in Figure 31. For IN048 and IN013 that showed a jump in DCPD signal, a general increasing trend can be seen in crack depth up to ~200 µm. As the surface crack lengths increase up to ~600 µm, the crack depth becomes invariant, maintaining a value of 150–250 µm. For IN049 with no an obvious change in DCPD signal, almost all cracks were less ~150 µm in depth except two that reached ~240 µm.

In addition, crack depth profiles were established on several of the long circumferential cracks that had been intersected and examined multiple times through iterative polishing (Figure 32). The available observations suggest that the longer cracks can generally be represented by an elliptical shape. All the multi-grain long cracks were oriented normal to the loading direction.

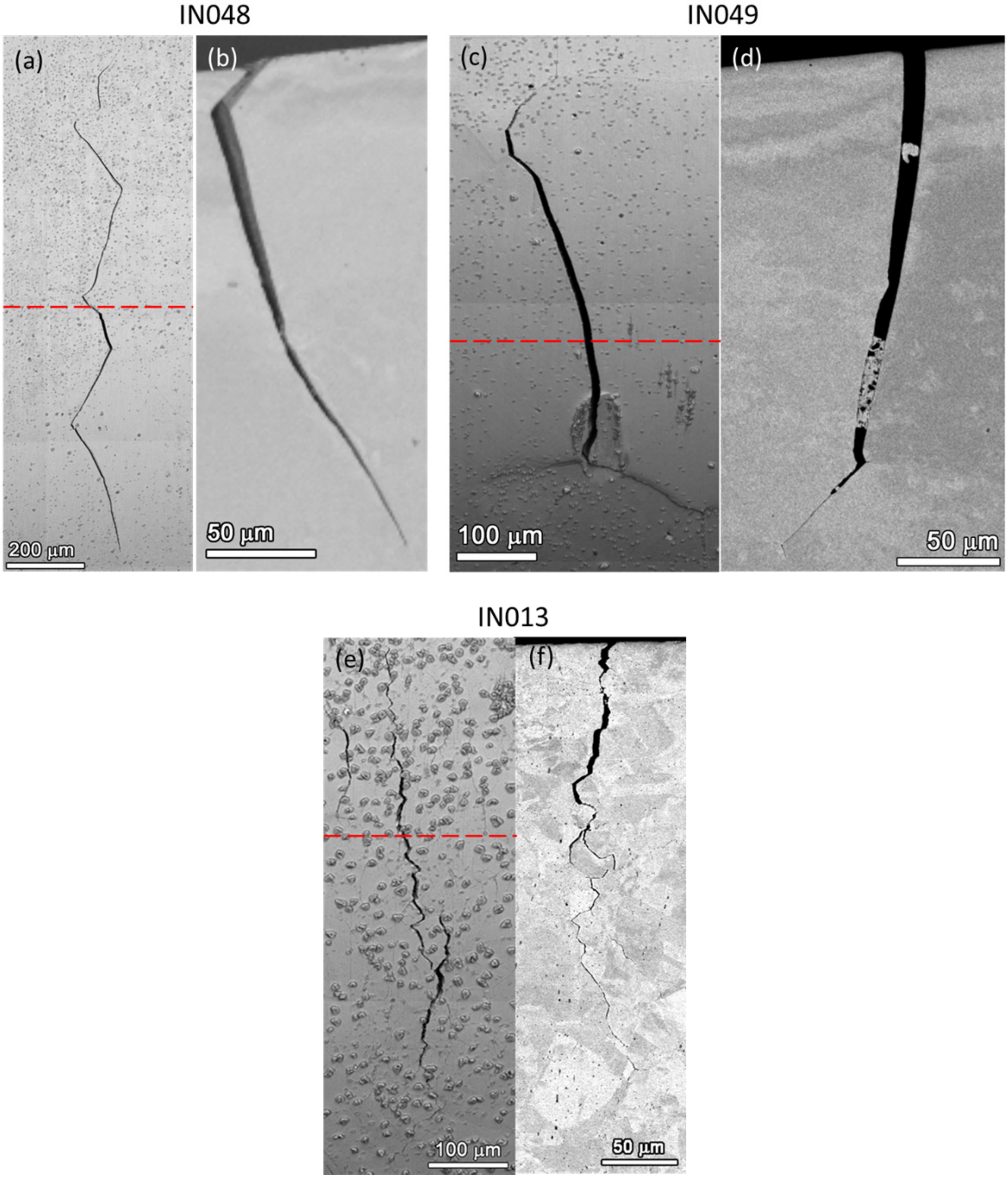

Figure 30. SEM-BSE images of surface morphology of the deepest cracks found in (a) IN048, (c) IN049 and (e) IN013 and examples of crack morphology at the cross-section plane (marked by dashed line in the figure displayed to the left) in (b) IN048, (d) IN049 and (f) IN013.

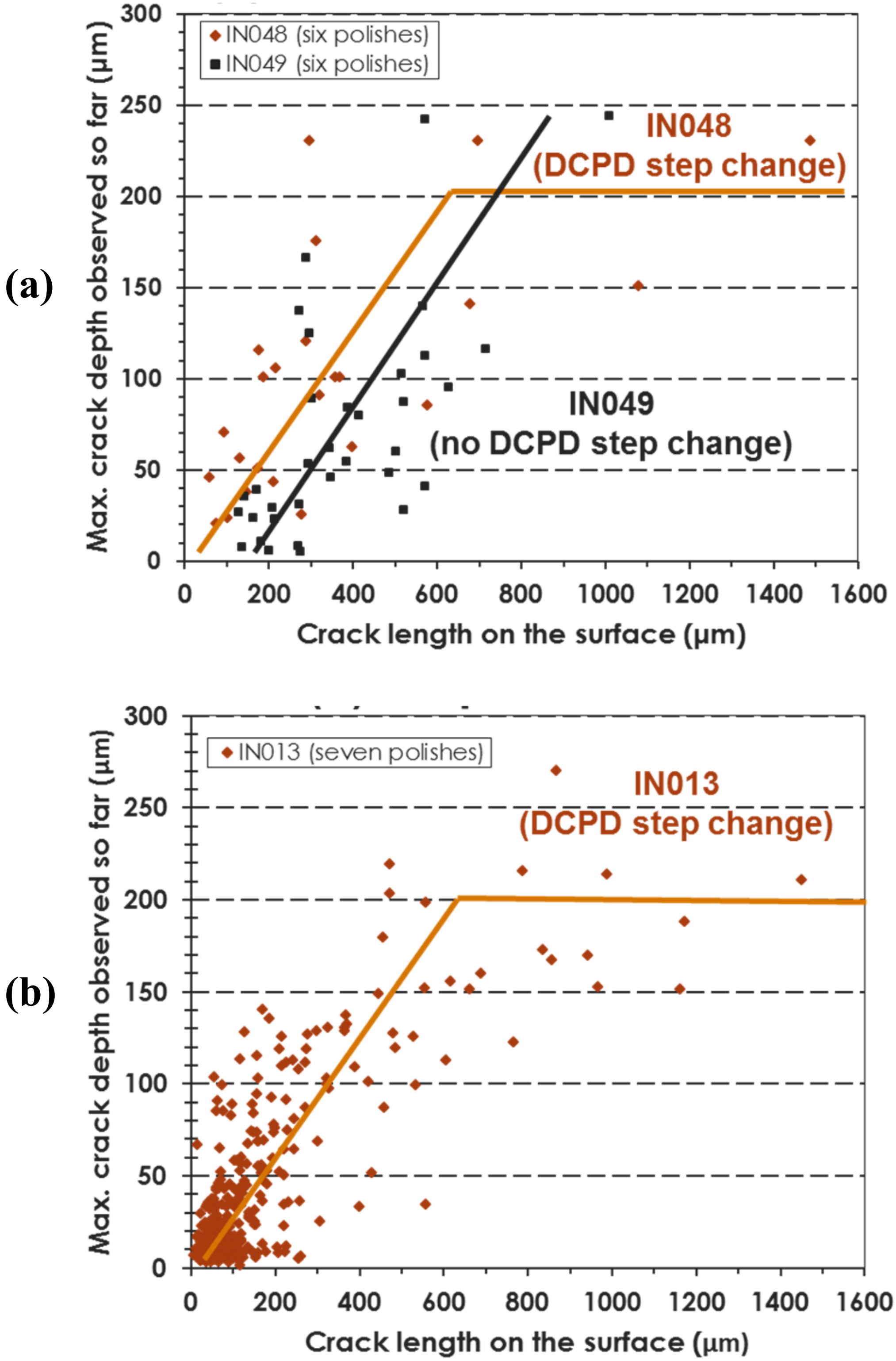

Figure 31. Distribution of maximum depth observed so far on each crack as a function of its surface length for (a) the CRDM specimens and (b) the plate specimen. The total number of cracks measured in IN048, IN049 and IN013 is 24, 36 and 525, respectively.

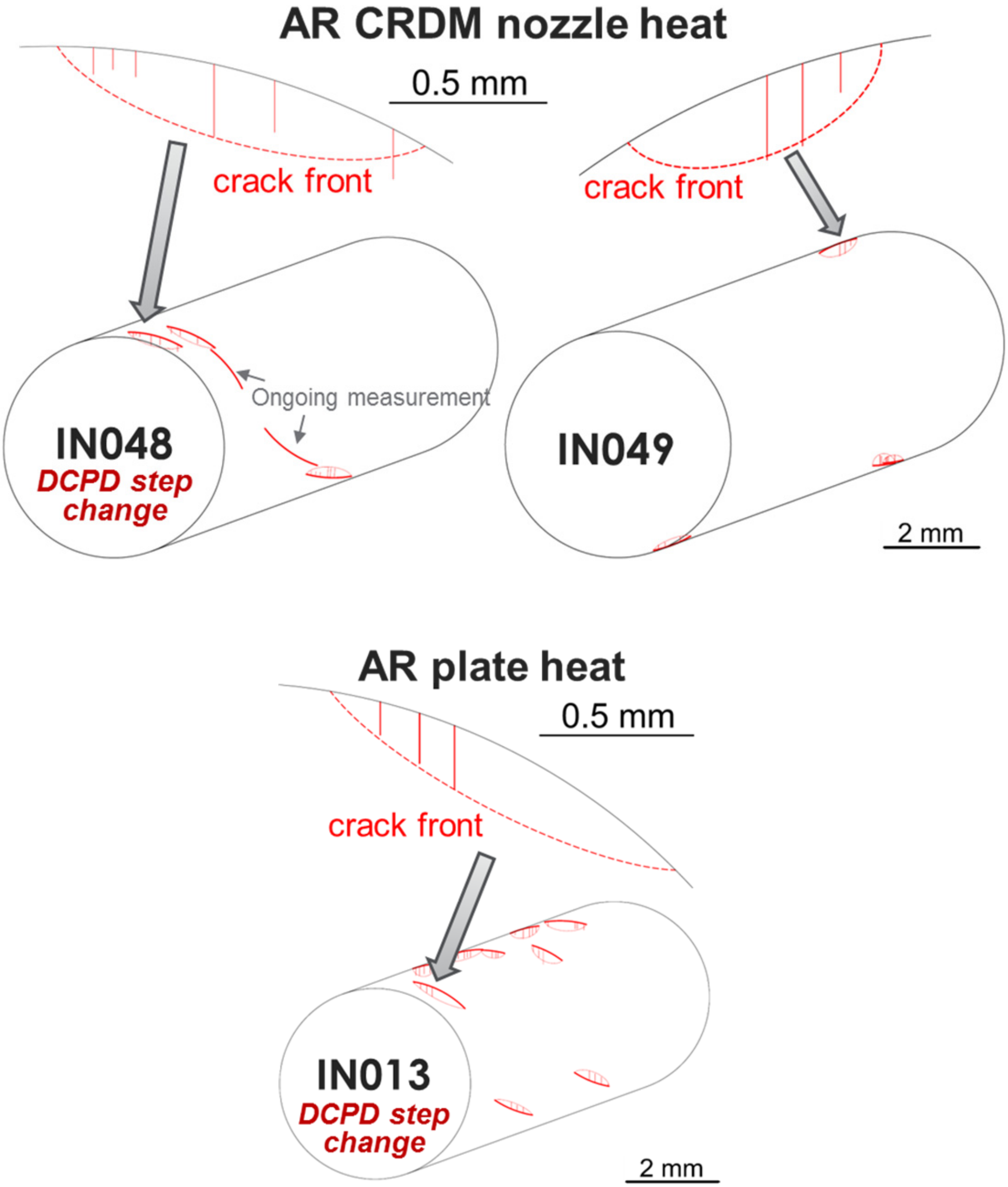

Figure 32. Schematics illustrating location and depth profiles for the major large circumferential cracks on gauge surface of the three AR alloy 600 specimens.

Crack Evolution

In order to better visualize crack distribution and evolution on the gauge section surfaces for each specimen, two-dimensional (2D) contour maps were constructed in terms of unit crack density and unit total crack length for after each interruption as well as the end of the test. An obvious increase in unit crack density and unit total crack length with increasing exposure time can be seen for the IN048/IN049 (Figure 33) and IN013 (Figure 34) specimens. The trend is also quantitatively reflected in average unit crack density and average total crack length for IN048/IN049 (Figure 35) and IN013 (Figure 36). Since IGA/small cracks and large cracks were not differentiated when plotting Figures 33 and 34, their contributions to the average unit crack density and average total crack length were separated in Figures 35 and 36. This provides a clearer indication of the actual crack evolution on these specimens. It is interesting to note that while the number and total length of large cracks in IN048 and IN013 increased constantly with time, the formation and growth of large cracks on the gauge surface of IN049 appears to be dramatically lower, if not completely stopped, after the one test interruption for this specimen. However, density and surface lengths for the IGA and small cracks increased during the second stage of the test for IN048 and IN049 as illustrated in Figure 35.

Crack Coalescence

Multiple test interruptions also made it possible to track the evolution of individual surface cracks. Observations revealed that most of the large circumferential cracks in IN048 and IN013 were formed by the growth and coalescence of separate smaller cracks instead of growth of a single crack as demonstrated in Figure 37. Consistent with the indicated lack of growth for large surface cracks in IN049 during the second stage of the test, no apparent crack coalescence was found on this specimen.

Evidence for two mechanisms of crack coalescence was discovered. For IN048 that had large grains of 150–500 μm in size, coalescence tended to occur after several short IG cracks nucleated at separated sections of a continuous grain boundary and gradually linked together during prolonged exposure as shown in Figure 37(a). For IN013 that had an ~65 μm grain size, it was more common to see two slightly offset cracks on different grain boundaries approaching and propagating beyond each other with the crack fronts turning toward one another (Figure 38). In the latter case, coalescence was also evidenced in depth below the proximity where two cracks joined each other on the surface as shown in Figure 39. This suggests that the depths of two previously separated cracks would become quite uniform after they coalesced.

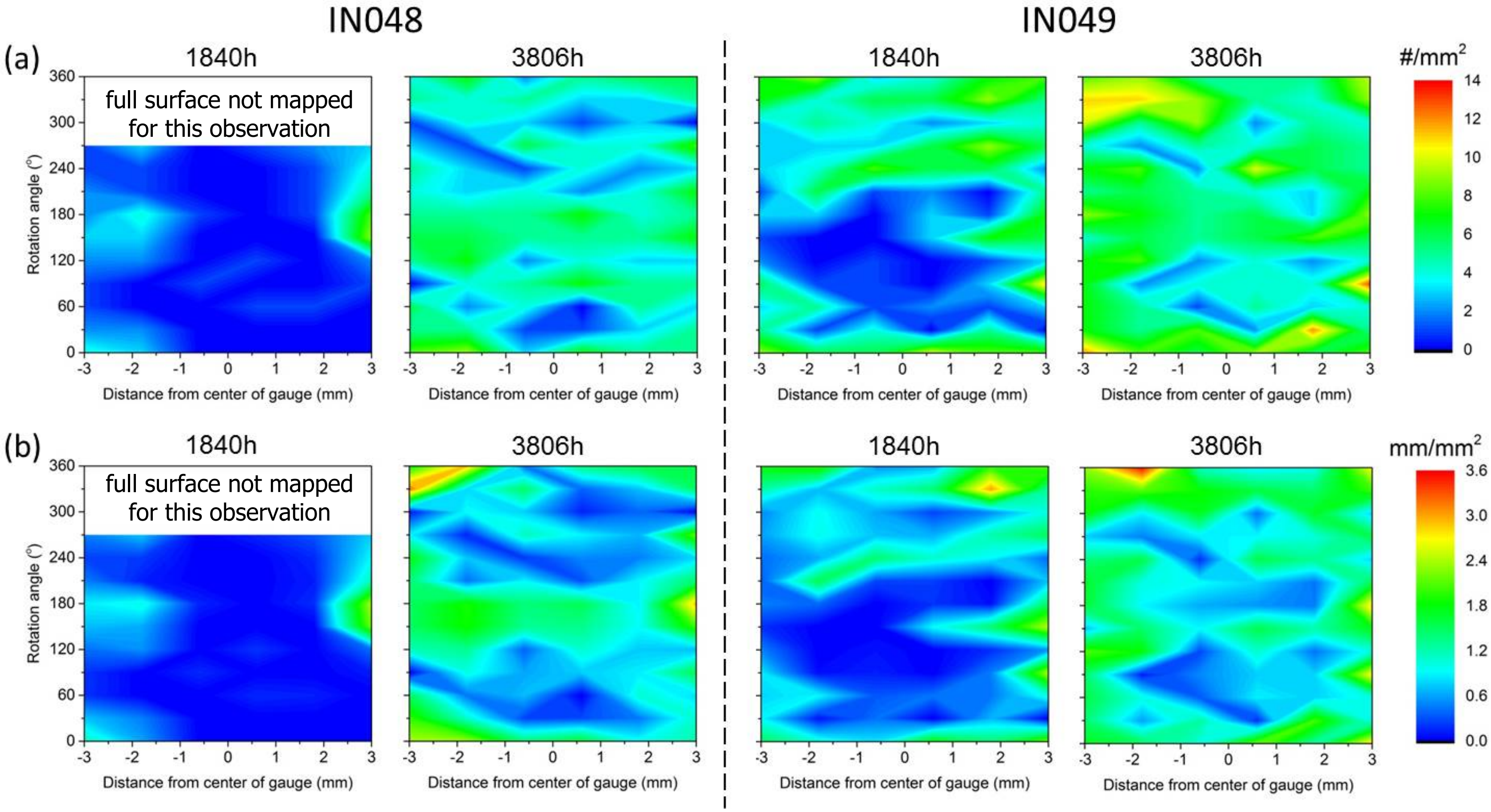

Figure 33. 2D mapping of the time evolution of (a) unit number density (#/mm^2) and (b) unit total crack length (mm/mm^2) on the gauge section of IN048 and IN049.

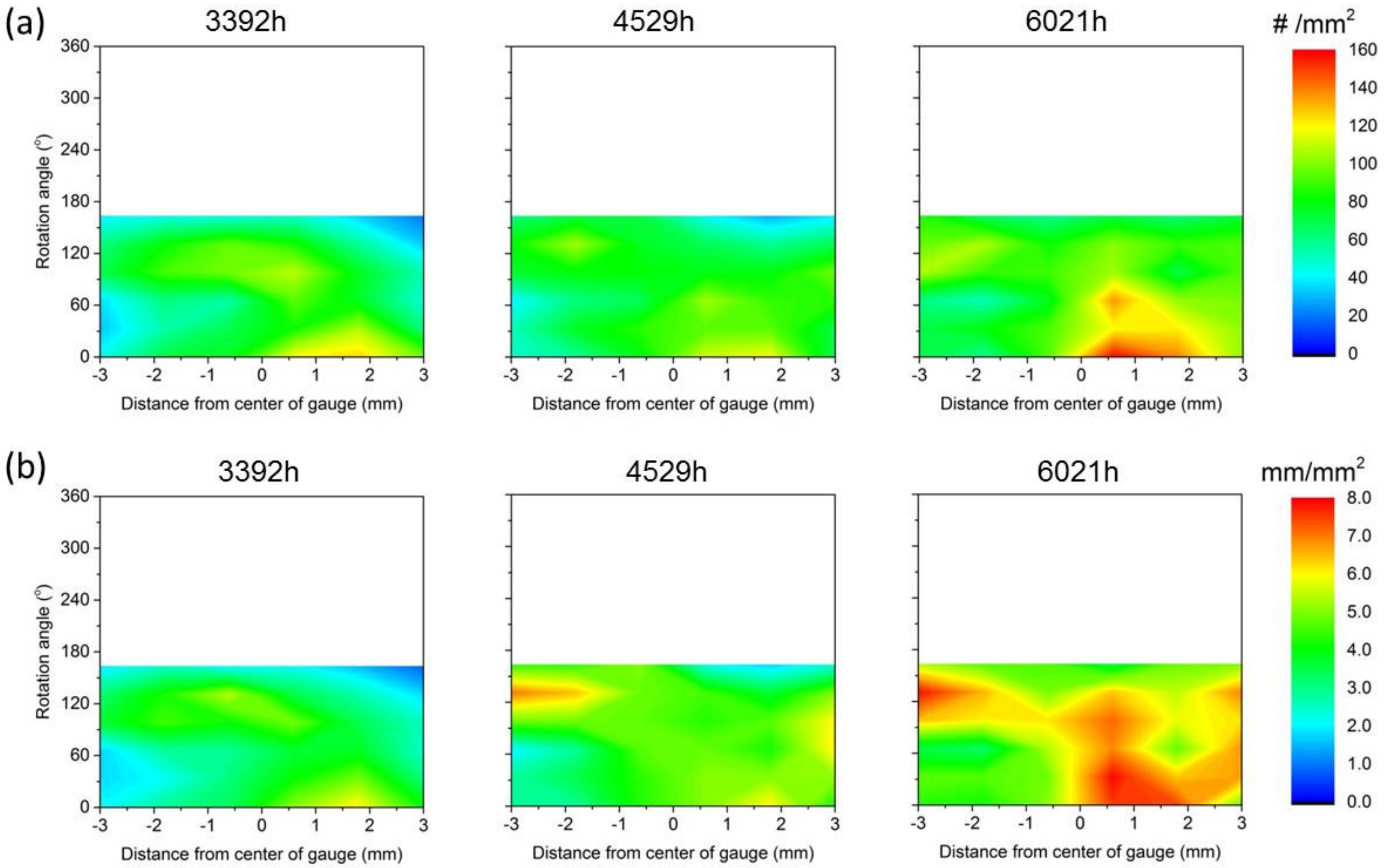

Figure 34. 2D mapping of the time evolution of (a) unit number density (#/mm^2) and (b) unit total crack length (mm/mm^2) on the gauge section of IN013. Only half of the entire gauge section was measured because of the large number of IGA and short cracks. The unmeasured half is left blank in this figure.

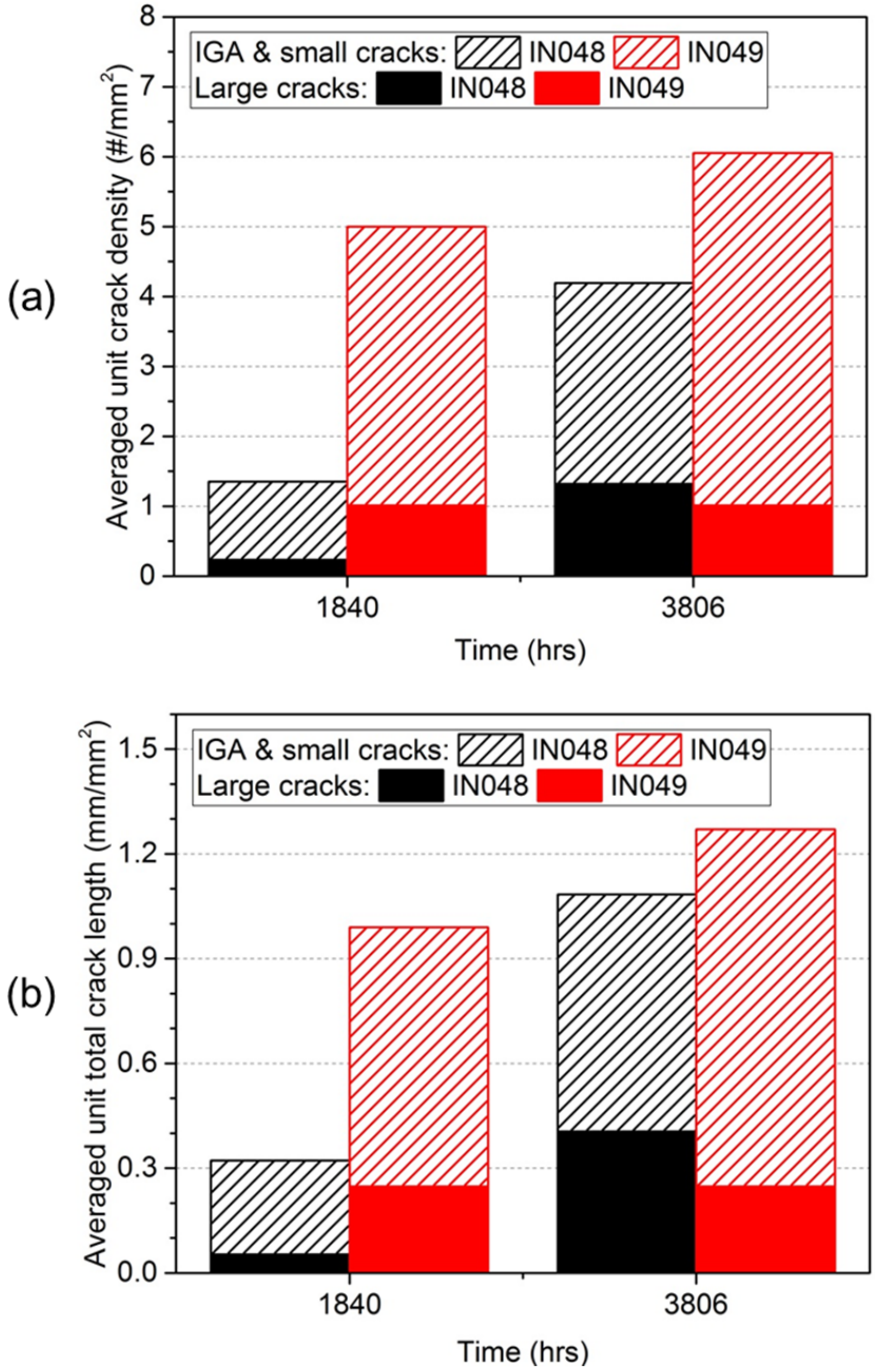

Figure 35. Time evolution of (a) the average unit number density (#/mm^2) and (b) the average unit total crack length (mm/mm^2) on the gauge section of IN048 and IN049.

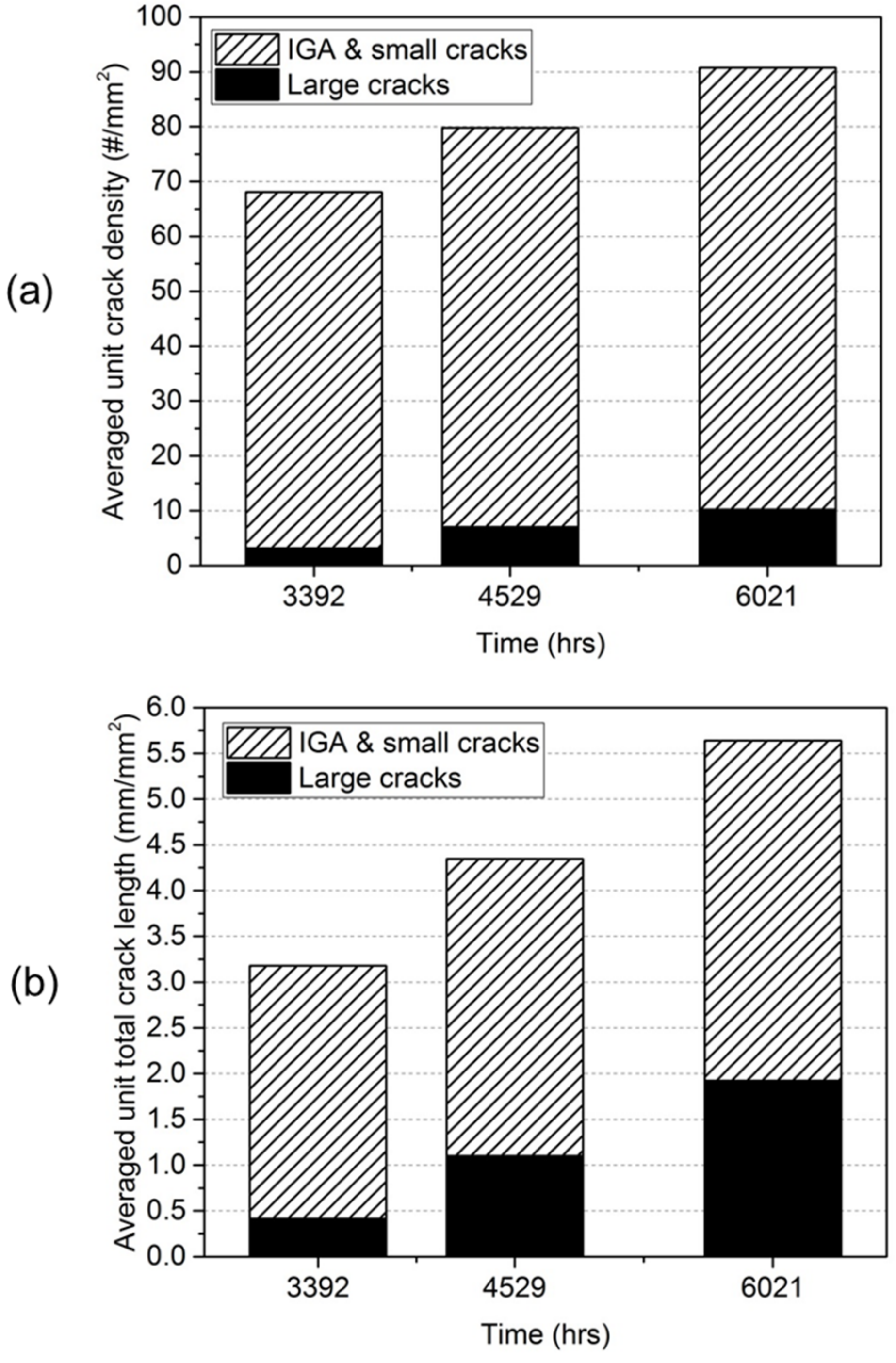

Figure 36. Time evolution of (a) the average unit number density (#/mm^2) and (b) the average unit total crack length (mm/mm^2) on the gauge section of MA plate 1.

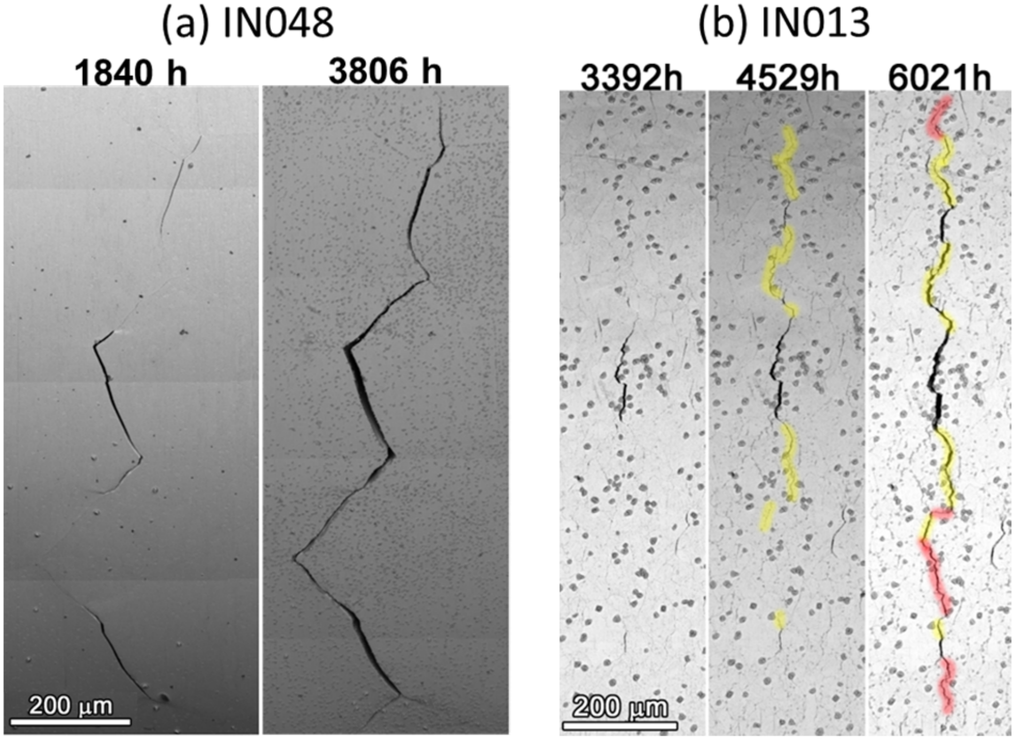

Figure 37. SEM-BSE images of coalescence of multiple cracks with progress in exposure time in (a) IN048 and (b) IN013.

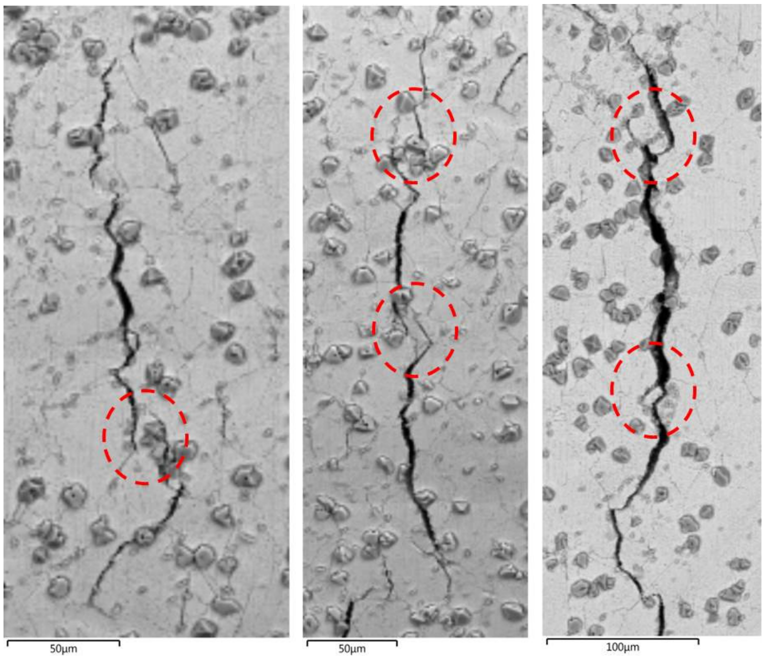

Figure 38. SEM-BSE images of examples of coalesced cracks in IN013 with fronts approaching each other (highlighted with circles).

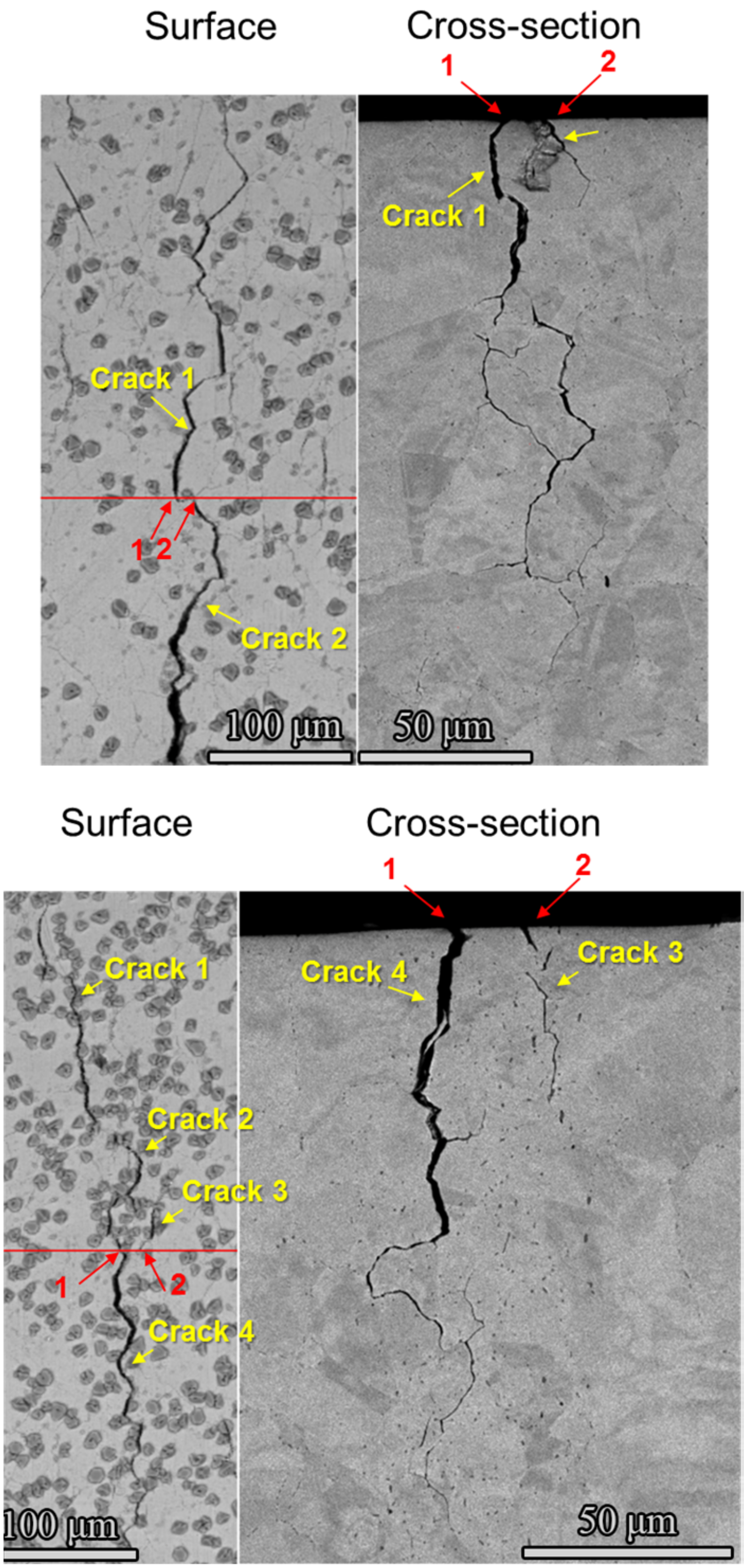

Figure 39. SEM-BSE images presenting two examples of crack coalescence for specimen IN013 observed as a function in depth.

Background on Analyzed Cold-Worked Alloy 600 Specimens

One CW specimen (IN022) from the alloy 600 service CRDM heat (M3935) and one CW specimen (IN052) from the alloy 600 plate heat (NX6106XK-11) have been characterized in detail. More information on these specimens can be found in Table 4.

As noted previously, the IN022 (20%CTS service CRDM) specimen was stopped early at ~385 hours due to a much higher than expected indicated DCPD strain rate from the very start of the test (Figure 18). The IN052 (8%CTS plate) specimen was stopped at ~1334 hours after a steady upward trend was observed in the DCPD strain rate response starting at ~1250 hours (Figure 40). Because of their relatively short exposure times, the tests on these specimens hadn't been interrupted before a DCPD indication of initiation. These two specimens were cross-sectioned and serially polished after surface examination to document crack depth distributions.

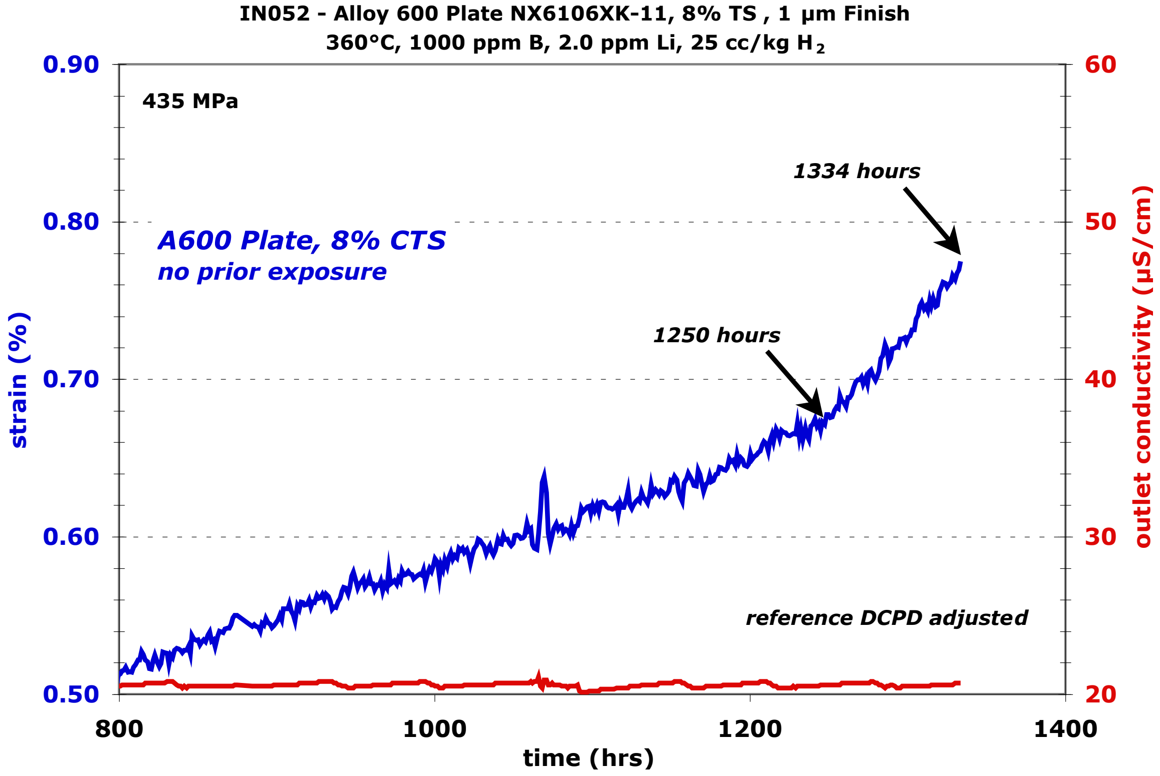

Figure 40. SCC initiation plot for the 8%CTS alloy 600 specimen IN052 revealing evidence for crack nucleation at ~1250 hours.

Detailed IGA and SCC Crack Morphologies of Cold-Worked Alloy 600

A unique feature of the CW service CRDM material was the presence of regions of local deformation on the surface as shown in Figure 41. These are likely to be grains that were oriented to allow easy slip in response to the applied stress as suggested by the slip steps on the surface that are generally perpendicular to the tensile axis. This behavior is thought to be due to the large grain size of this material.

Unlike the AR specimens, it was very difficult to identify IGA on the surface of the CW specimens from the same heats (Figures 41 and 42). Subsequent SEM examination on cross-sections revealed that IGA had formed at many high energy grain boundaries in both specimens. As shown in Figure 43, these features are generally tighter and shallower than those observed in the AR materials making them more difficult to identify from the surface examinations.

An interesting observation on several CW alloy 600 specimens is that IGA appears to end when reaching grain boundary carbides, as illustrated in Figure 44. Even though the grain boundary carbide distributions are far from continuous, interactions with the Cr-rich carbides may slow the progression of IGA.

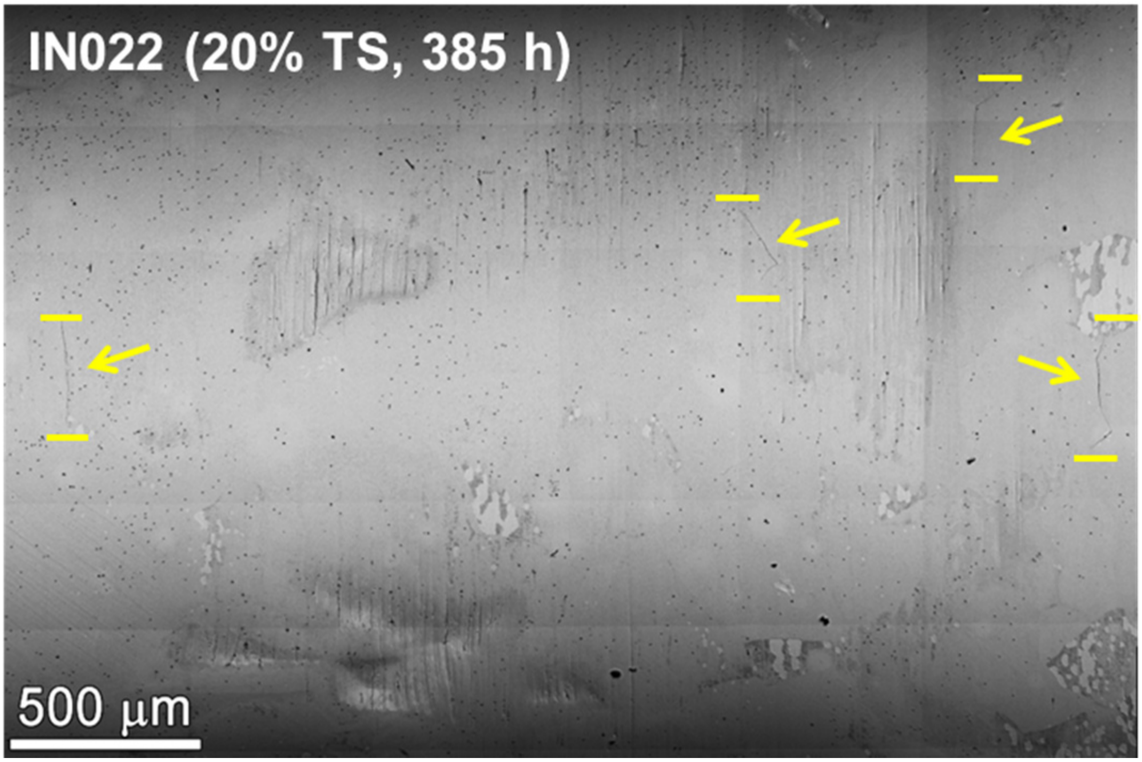

Figure 41. SEM-BSE montage images of typical surface morphology of the 20%CTS service CRDM specimen IN022 by the end of the test. Obvious cracks are identified by arrows with upper and lower end marked by short horizontal lines.

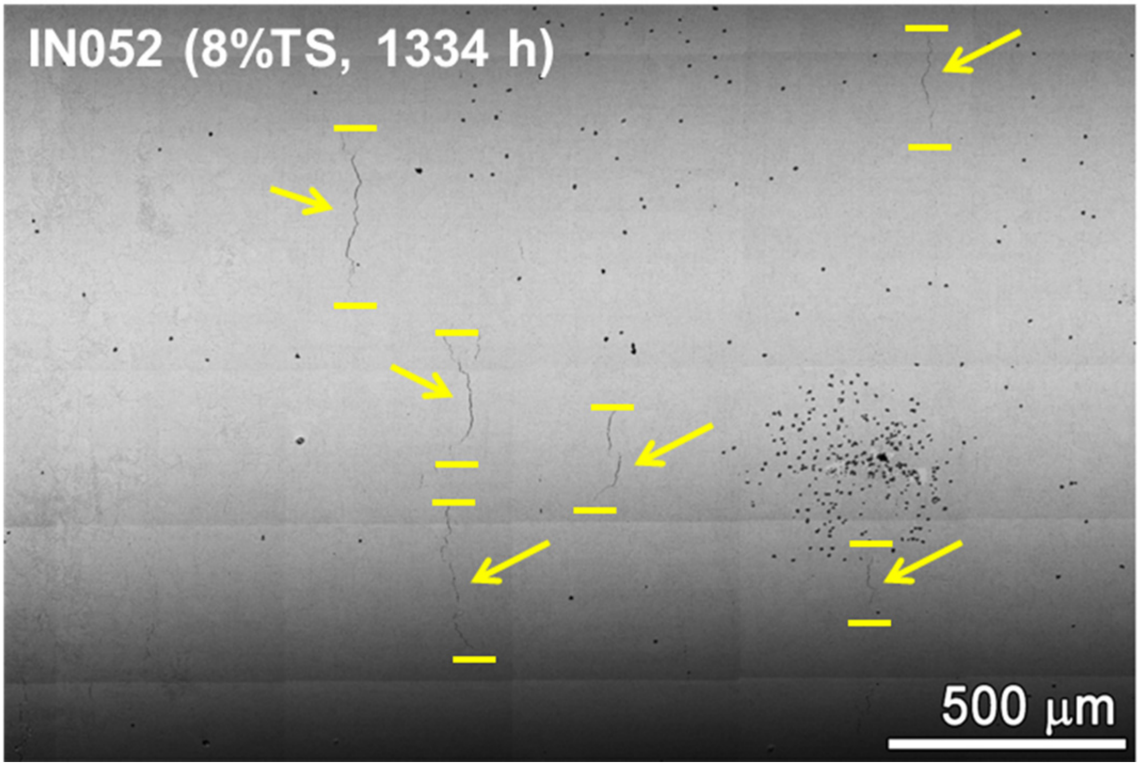

Figure 42. SEM-BSE montage images of typical surface morphology of the 8%CTS plate specimen IN052 by the end of the test. Obvious cracks are identified by arrows with upper and lower end marked by short horizontal lines.

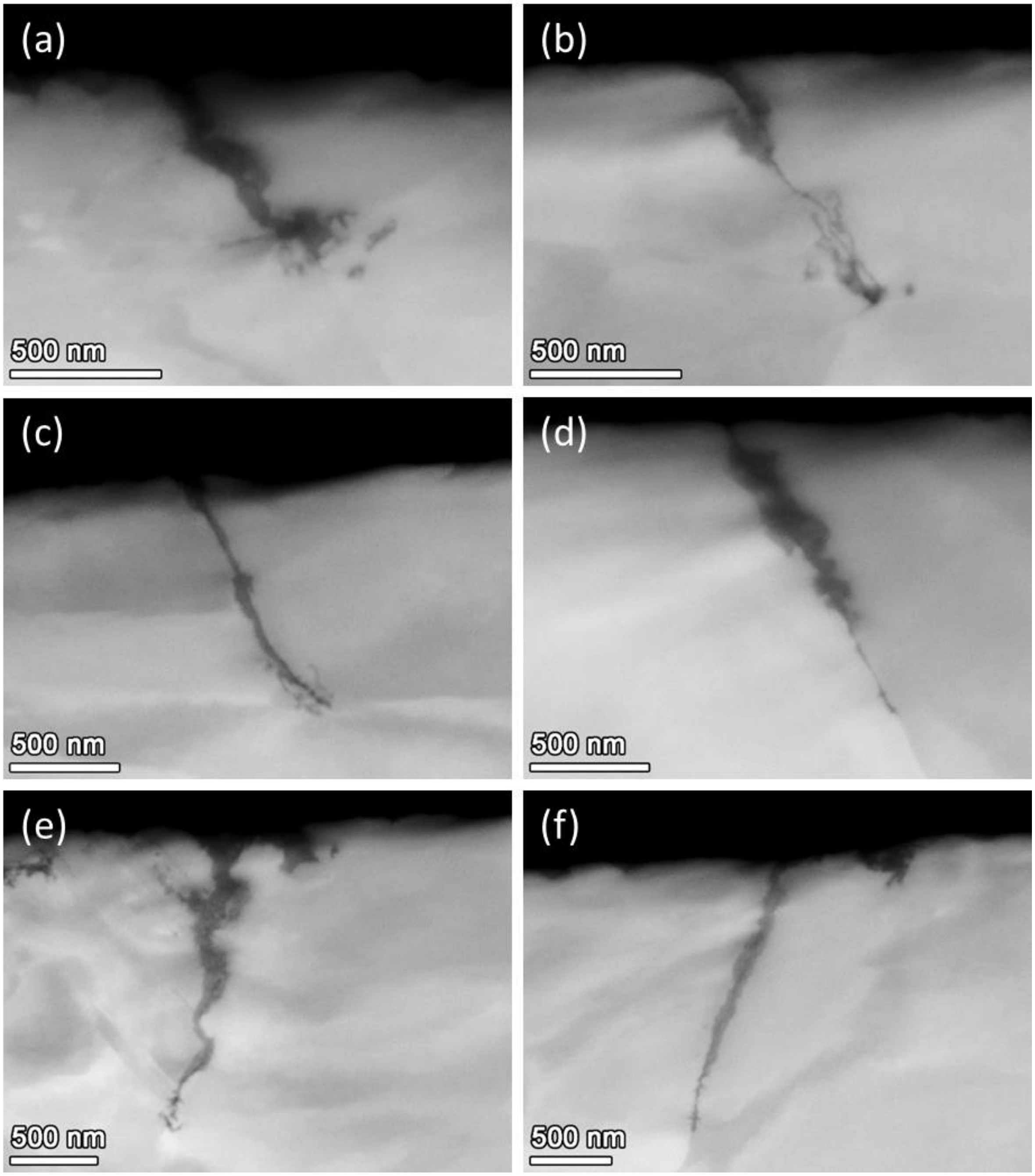

Figure 43. SEM-BSE images of typical IGA morphologies observed in cross-sections for the IN052 specimen. The images are displayed in ascending IGA length L: (a,b) L ≈ 500 nm, (c,d) L ≈ 1 µm, (e,f) L ≈ 1.5 µm.

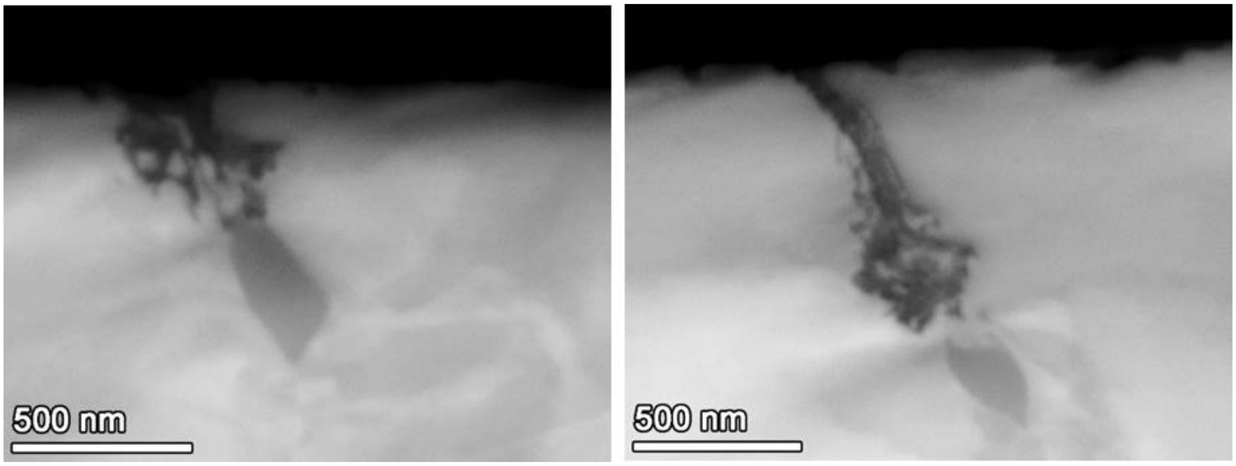

Figure 44. SEM-BSE images of typical IGA morphologies ending at grain boundary carbides in cross-section samples for the IN052 specimen.

As shown in Figures 41 and 42, obvious cracks were formed at several high energy grain boundaries in the two CW specimens. While the crack surface lengths in the large-grained IN022 are usually shorter than the average grain size, most cracks in IN052 had propagated along multiple grains boundaries on the surface. Crack depth profiles were established on the longest cracks that had been intersected and examined multiple times through iterative polishing (Figure 45). Observations indicate that these large cracks can be reasonably well represented by a semi-elliptical shape.

The surface morphology of cracks marked A and B on IN052 in Figure 45 are shown in Figures 46 and 47 respectively, accompanied with the morphology at selected cross-sections revealed by serial polishing. It is worthwhile to note that in Figure 46, one crack joined the other spaced ~20 µm apart at ~150 µm deep below the surface. Interestingly, Figure 47 clearly suggests that the largest crack in IN052 is formed by coalescence of two offset cracks showing similar depths. It is not clear that the similar depths of these two cracks developed before or after coalescence. Although exact crack evolution was unknown for this specimen because the test had never been interrupted, the above evidence suggests that coalescence may have played an important role in crack growth both on the surface and in depth for the CW plate specimen.

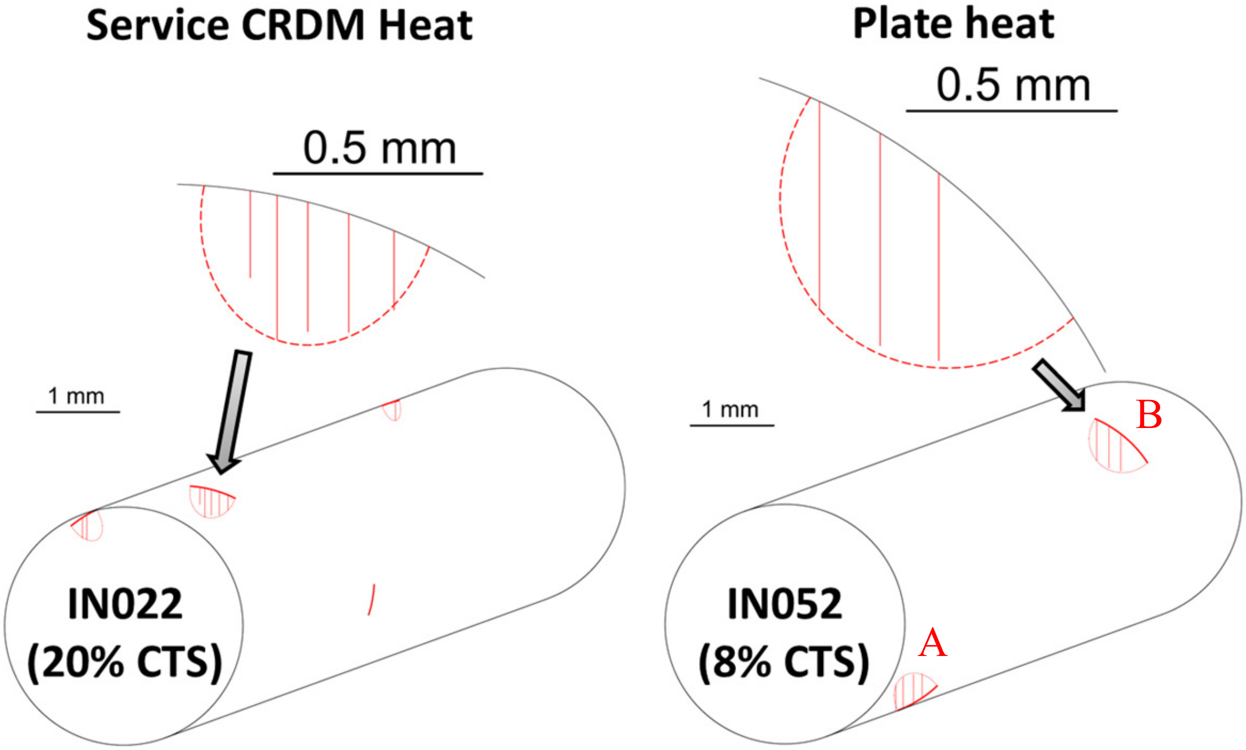

Figure 45. Schematics illustrating location and depth profiles for the major large circumferential cracks on gauge surface of the two CW alloy 600 specimens.

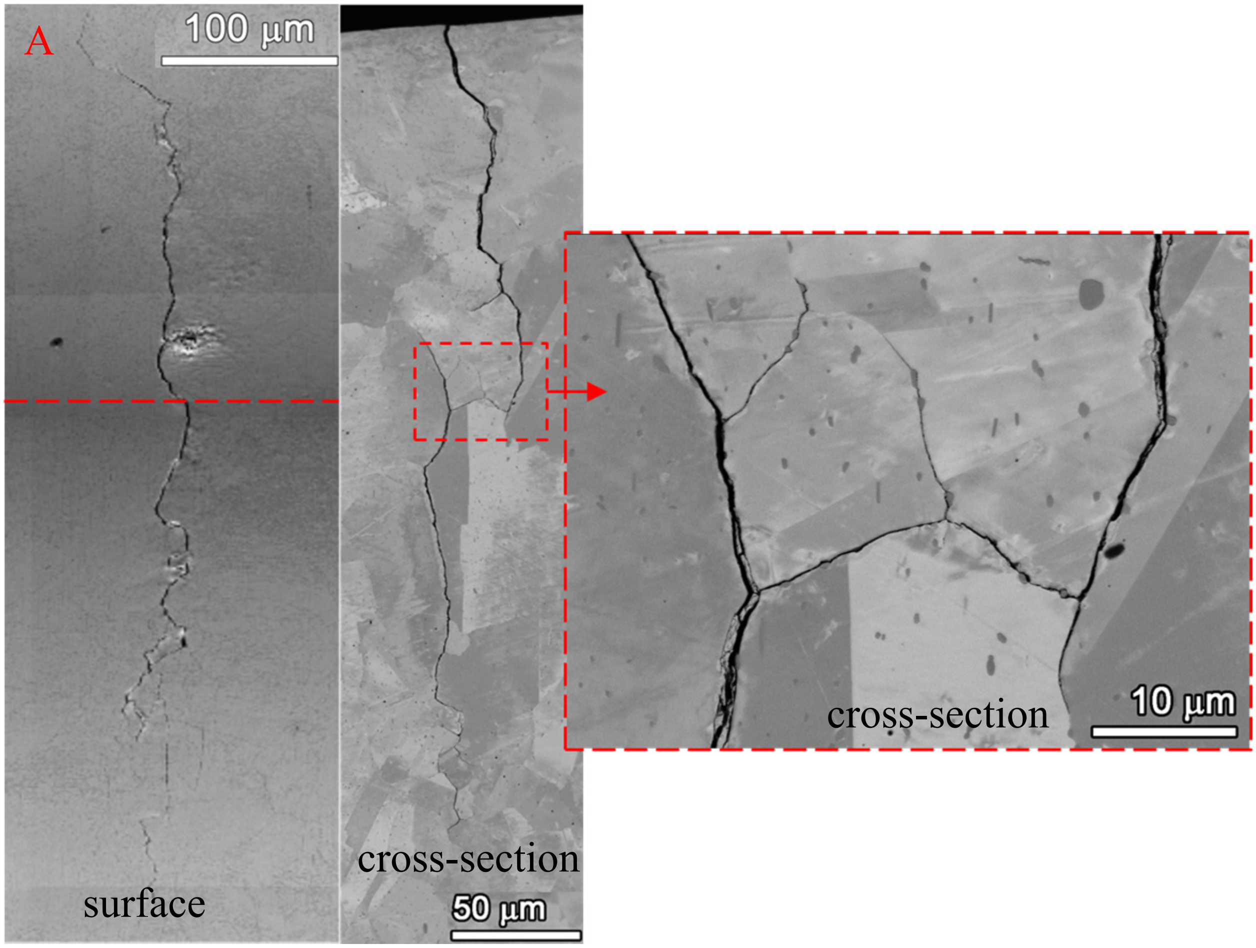

Figure 46. SEM-BSE images of crack A surface morphology for the IN052 specimen in Figure 45 and example of crack morphology at the cross-section plane (marked by dashed line).

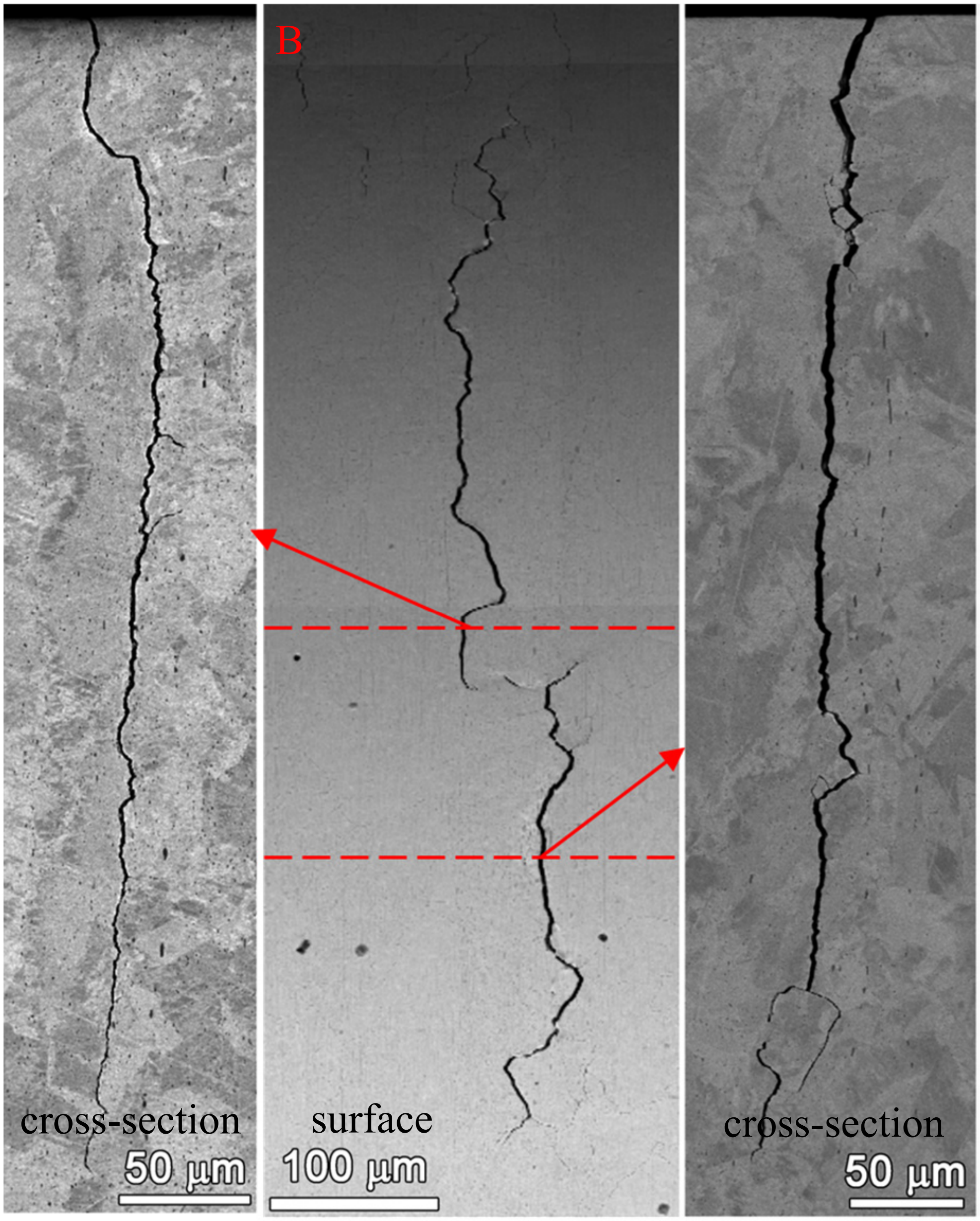

Figure 47. SEM-BSE images of crack B surface morphology for IN052 in Figure 45 and examples of crack morphology at two cross-section planes (marked by dashed lines).

Microstructure Comparison Between As-Received and Cold-Worked Materials

In order to quantitatively compare the difference in crack distribution on the surface between the AR specimens and CW specimens, frequency distribution as a function of crack surface length has been established as shown in Figure 48. For both heats, the number of cracks within the same length group is always higher in the AR specimen than in the CW specimen. In addition, the longest surface crack in the CW specimen from both heats are ~600–700 µm in length, whereas the AR specimens have more cracks with longer surface lengths reaching a maximum length of ~1.5 mm.

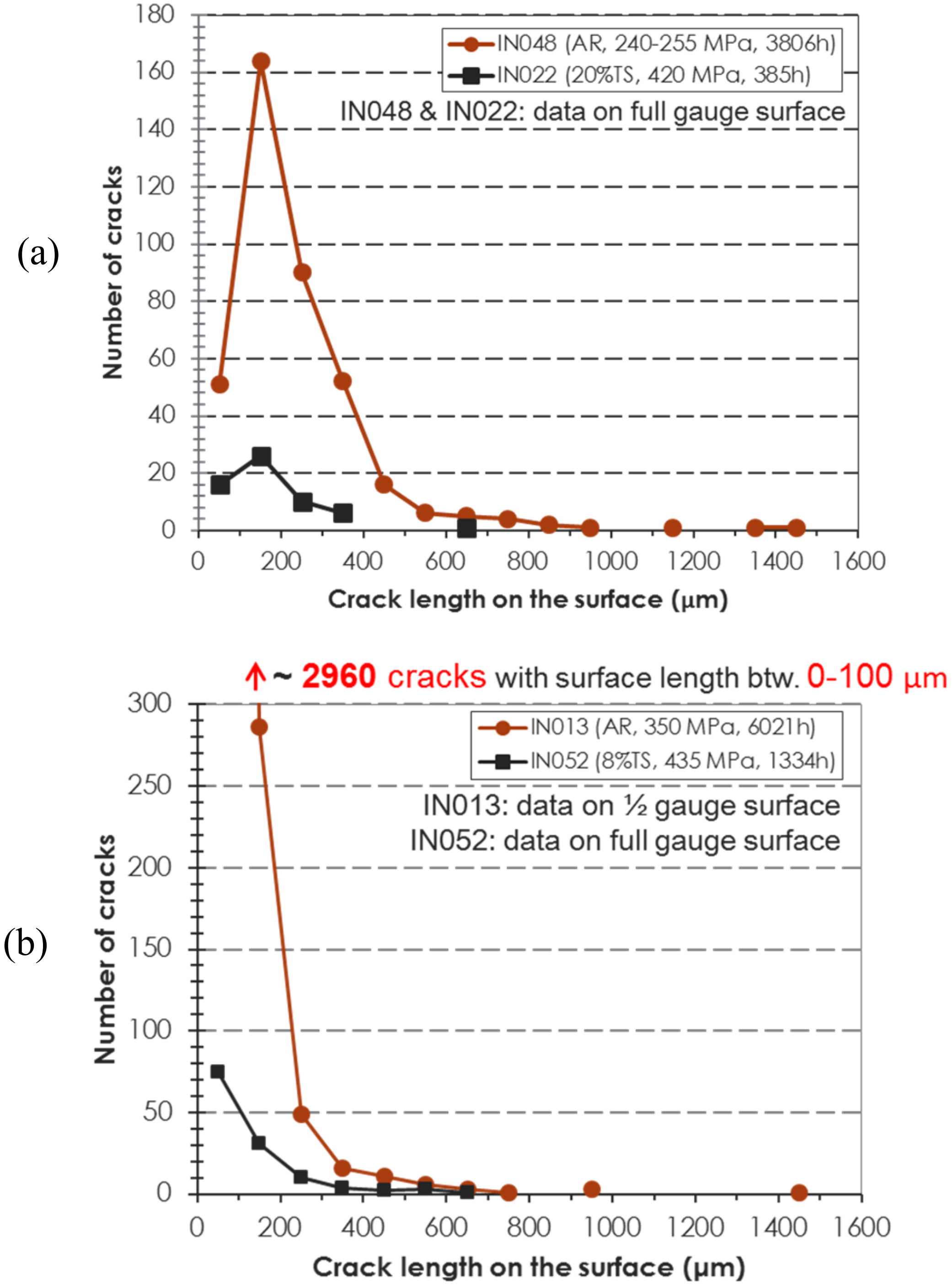

Figure 48. Frequency distribution of crack surface length of the AR and CW specimens in (a) service CRDM heat and (b) plate heat.

As mentioned previously, a difference was found in the shape of the large cracks in the AR and CW specimens. This is clearly shown in Figures 49 and 50 where maximum depth of every crack observed and measured during serial polishing and SEM examination is plotted as a function of its surface length. For both the service CRDM and plate heats, the aspect ratios (crack depth divided by ½ the crack surface length) of relatively short surface cracks in the AR and CW specimens are similar. However, distinctively different crack growth behavior seemed to have been triggered by the surface length reaching a "transition" point. In the CW materials, the crack aspect ratio increased dramatically after the transition point indicating the onset of rapid crack propagation. For the AR materials, the crack depth saturated after the transition point despite further growth of cracks on the surface.

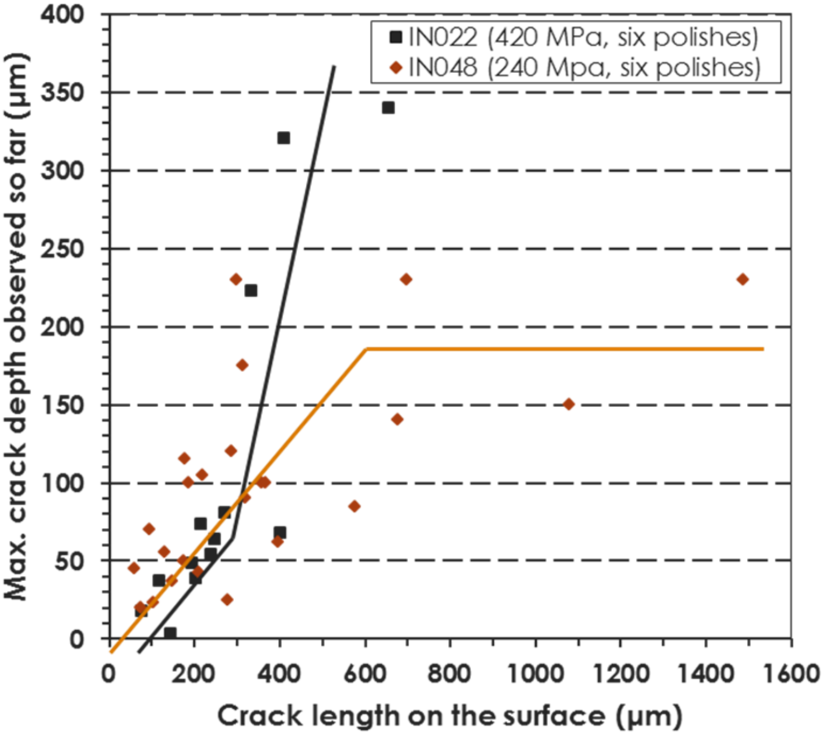

Figure 49. Distribution of maximum depth observed on each crack as a function of its surface length for the service CRDM specimens. The total number of cracks measured in IN048 and IN022 is 24 and 13, respectively.

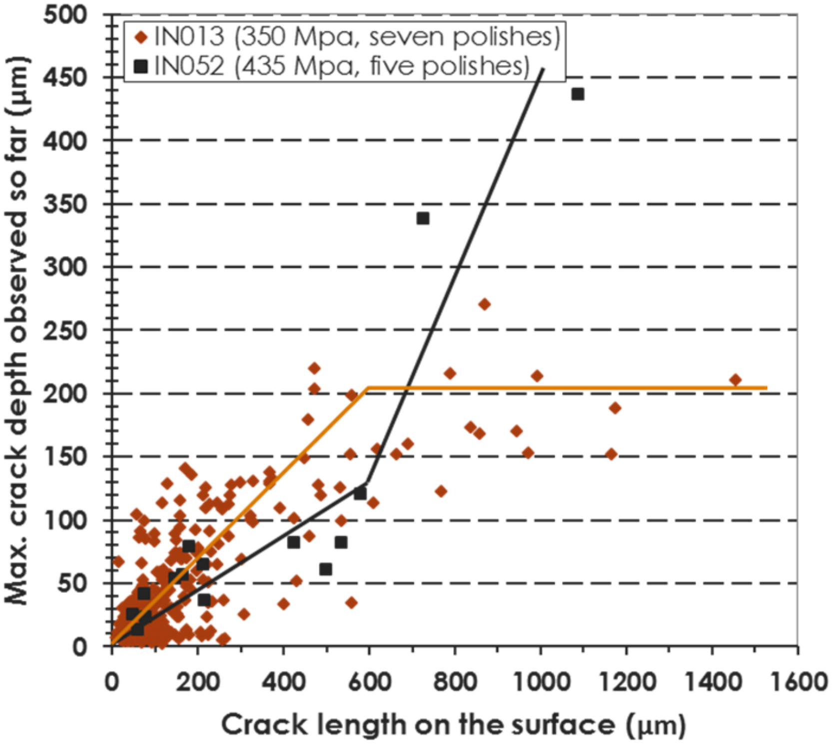

Figure 50. Distribution of maximum depth observed on each crack as a function of its surface length for the plate specimens. The total number of cracks measured in IN013 and IN052 is 525 and 15, respectively.

Discussion

Effect of Surface Condition on SCC Initiation

The available data indicate a consistent trend for the ground specimens to initiate slightly after the polished specimens. Limited post-test microstructural observations have been performed and suggest that additional time is required for corrosion and cracking to proceed through the ground region. Several possible reasons for this exist. For less aggressive grinding (e.g., 1200 grit), a thin layer of recrystallized nanocrystalline grains is created at the surface and may accelerate Cr diffusion to the surface producing a more protective oxide. More aggressive grinding produces a more complex and deeper near-surface damage microstructure that may also promote the formation of a more protective oxide layer and further isolate the bulk grain boundaries from the water. In comparison, a highly polished surface ensures that all grain boundaries reaching the surface have direct access to the corrosion environment and IGA can begin immediately on exposure. Morris, et al. [12] examined the effect of surface condition on IGA for alloy 600 in some detail and reached similar conclusions. This behavior is in contrast to service experience [13-16] where the first initiation events have been observed on heavily damaged or ground surfaces. It is thought that the extremely high residual tensile stresses can develop at the deformed surface during assembly procedures or plant operating variations. These much higher stresses along with potential local surface flaws produced by grinding are believed to cause more rapid SCC initiation through the heavily damaged surface layer.

Correlation of Crack Initiation to Stress Intensity

Since IG cracks of significant depth have been observed in all the characterized AR and CW specimens, consideration has been given to the relationship between crack geometry and the local K value. A number of finite element modeling (FEM) studies based on linear elastic fracture mechanics have already been published that estimate the K for a thumbnail surface crack growing through a rod under tension [17-22]. The cracks are generally considered to be of straight, elliptical or circular in shape, and a dimensionless factor F is introduced to account for the geometrical impact on K as given by:

$$K = F\sigma\sqrt{\pi a} \tag{4}$$

where a is the crack depth, σ is the applied stress. F is typically calculated by FEM based on the geometry in Figure 51 using relative crack depth (a/D), crack aspect ratio (a/b) and relative distance from the center of crack front (s/s_0 in Figure 51a or x/h in Figure 51b) as inputs.

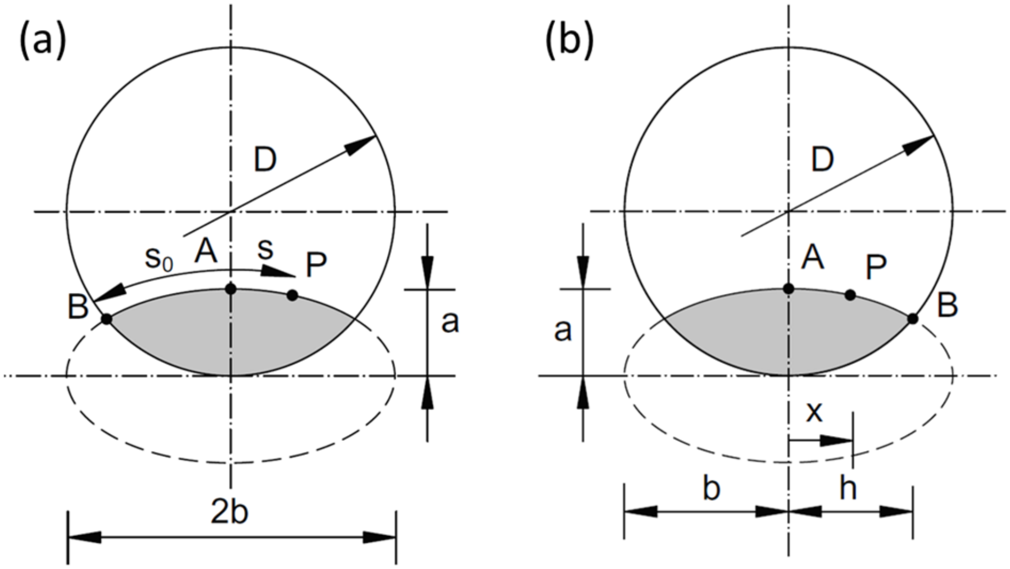

Figure 51. Crack dimension definitions used for K factor calculation in (a) Ref. [22] and (b) Ref. [17].

Assuming an elliptical crack shape, the range of K at the crack center of the most significant crack in each specimen has been estimated using values of F provided in selected FEM studies [17,19,22]. The results are summarized in Table 6. The variability of the peak stress intensity is due to slightly different F values produced by each of the published FEM studies.

Table 6. Estimated K (MPa√m) at the front center of the largest crack observed in each specimen.

	Service CRDM heat (M3935)		Plate heat (NX6106XK-11)	
	Spec. ID	K at front center	Spec. ID	K at front center
As-Received	IN048	6.0–7.0	IN013	9.0–9.6
	IN049	5.5–6.0		
Cold Worked	IN022 (CTS 22%)	9.0–10.5	IN052 (CTS 8%)	10.5–12.5

Estimates of local K have also been made as a function of position along the crack front. Although many FEM studies provided solutions for F when crack aspect ratio a/b ≤ 1, Ref. [22] appears to be the only one that considered the situation where a/b > 1, which is the case for the large cracks observed in the two CW specimens. Therefore Ref. [22] was used for this estimation and K evolution from the center to the end along the crack front is illustrated in Figure 52.

It is shown that for the three AR specimens, K decreases from the center to the end of the long circumferential cracks. For the non-CW materials, IN013 had a higher K predominantly because of the higher applied stress to this specimen. IN048 and IN049 have nearly identical K profiles suggesting that while IN049 did not exhibit an indication of initiation, it was very close in evolution to IN048. In addition, these K values are generally below the threshold K of 9 MPa√m for SCC growth proposed for MA alloy 600 [23-26] consistent with the fact that no fast growing cracks were observed in these specimens. It is also important to note that the strain jump observed in these non-CW specimens may not be true indication of SCC initiation as discussed earlier, and instead an upward trend in strain rate may be the more appropriate indicator of SCC initiation like for the CW materials.

For the two CW specimens, K keeps increasing from the center to the end of the large cracks. Results show that the K at the center is typically higher than 10 MPa√m and rises up to 15–20 MPa√m at the point where the crack meets the surface. SCC crack growth has a strong dependence on K within this range [25], and it is believed that one of the key contributors to the onset of rapidly growing SCC crack is this increase in K [27]. On the other hand, it has been reported [18] that a critical aspect ratio $(a/b)_c$ exists for each relative crack depth (a/D), and the dimensionless K factor F is higher at the crack center when a/b < (a/b)c. However when $a/b > (a/b)_c$, F is higher at the crack surface. Combined with the observation results, it seems very likely that the transition from a nascent crack to an actively growing SCC crack is influenced strongly by a crack reaching a critical shape (both in crack aspect ratio and relative crack depth), so that K values sufficient to sustain a faster CGR are produced across the entire crack front.

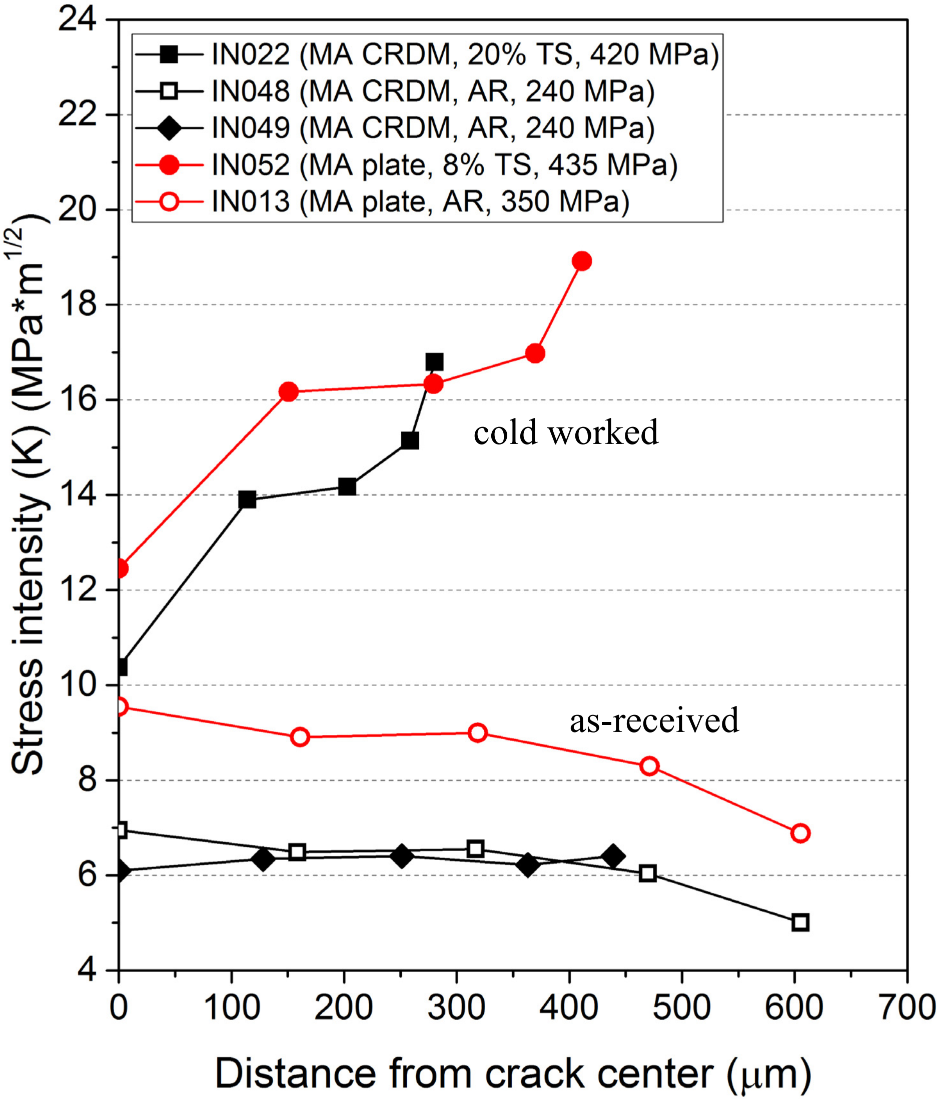

Figure 52. *K* estimated from crack center to crack surface of the largest crack observed in all the five specimens.

Correlation of Crack Development to DCPD Response

In order for DCPD to detect initiation, the cracking component of the signal must be discernable above the components due to creep and resistivity evolution. This can be accomplished in two ways. The first is that the increase in DCPD voltage due to a unit change in crack length would have to be very large. A slow growing crack with this attribute would be readily detected above the creep and resistivity evolution components. If the increase in DCPD voltage due to a unit change in crack length is small, then crack growth would have be rapid enough to cause a sufficient increase in the signal to be detectable above creep and resistivity evolution components. Because the microstructural investigations show that extensive cracking occurs before DCPD-based initiation occurs, it is thought that this latter scenario best describes what is taking place when SCC initiation is detected by DCPD, and that the crack growth rate has to be sufficiently high before it can be detected.

A common feature to all the alloy 600 materials that have been examined is for extensive IGA to form on high energy grain boundaries intersecting the surface with some of these converting to shallow IG cracks. DCPD is not sufficiently sensitive to detect this evolution of crack precursors for the current specimen design. Instead, significant growth of these shallow cracks is required for detection. Evidence for this behavior can be seen in the rate of change of the DCPD signal for the highly CW materials such as the 18%CTS plate (Figure 14). The initiation response is very dramatic with progression to potential failure taking place within a day of SCC initiation detection. The lower CW materials, such as the 7%CTS CRDM (Figure 15), exhibit a progression from initiation to potential failure that takes place over a period of a few weeks. This varied response is caused by differences in the material SCC growth rates under the given test conditions. For AR non-CW materials that did not exhibit a strain jump, the time it takes for cracks to reach this resolvable CGR is even longer (Figure 16). A number of factors may play a role in the time it takes, but two factors are strongly believed to be important: (1) the highly CW materials are tested at a higher applied stress (equivalent to its yield stress) and (2) SCC growth rates increase with the degree of cold work. As a result, the transition from a nucleated surface crack to long crack growth is much easier for the highly CW materials under a higher applied stress. A third factor whose effect that is yet to be sufficiently evaluated, but may play a role, is crack coalescence. In the majority of the specimens that have been examined, the deepest cracks appear to be the product of coalescence events.

Prior work [23-26] has proposed that a critical K is needed for SCC initiation, and this has been supported by the MRP alloy 600 disposition curve (Figure 21) where SCC growth rates are predicted to have a threshold response starting at 9 MPa√m [25]. However, the observations made to date for this report require a much more continuous response as a function of K in order for short precursor cracks starting from a length of <10 μm to reach lengths of >250 μm. Initiation times of ~4000-8000 h in the non-CW materials where crack depths of 250-350 μm are observed require an average crack growth rate of 1-2x10^{-8} mm/s. Crack growth rates in CW materials prior to detected initiation must be even higher. This suggests that relatively fast crack growth may be occurring for stress intensities as low as 2-3 MPa√m, quite surprising particularly for the AR materials. These apparently high SCC growth rates may be influenced by a rising K due to the increasing crack length under constant loading that is known to accelerate SCC growth rates [28].

Attention has also been given to the DCPD responses measured prior to the detection of obvious changes in the strain rate. The referenced strain rate reflected by DCPD in the 20%CTS service CRDM specimen IN022 is ~4X faster than the ones observed in the AR service CRDM specimens IN048 and IN049 prior to conclusion of their tests (6.5x10^{-4} %ε/h vs. 1.6x10^{-4} %ε/h and 1.5x10^{-4} % ε/h). Similarly, the referenced strain rate prior to the indicated SCC initiation time in the 8%CTS plate specimen IN052 is ~2X faster than the one in the AR plate specimen

IN013 prior to the step change (5.4×10^{-4} %ε/h vs. 2.0×10^{-4} %ε/h). These differences probably result from multiple factors such as the higher loading stress, more susceptible microstructures and relatively fast formation/propagation of a few major cracks in the CW materials. Compared to the AR specimens, most IGA penetrations in the CW materials are very shallow (<1 µm), and there are only a very limited number of small cracks, thus their contribution to the increase in DCPD strain rate by these features is considered to be small.

The other DCPD response that was detected above the creep and resistivity evolution signals was a sudden jump observed in IN048 (Figure 26) and IN013 (Figure 27). Such phenomenon has been reported by KAPL [29] for ~40% of their alloy 600 tensile specimens tested at or above their yield strength in 360°C hydrogenated water, as well as for other Ni-Cr-Fe alloys (e.g., alloy 618, alloy 690) during creep testing by others [30] at temperatures between 454–566°C in air. Figures 31 and 32 show that the geometry of the large cracks observed after the DCPD jump in IN048 and IN013 are quite similar to each other, both with a length of ~1.5 mm and a maximum depth of ~230 µm. In contrast, no cracks longer than ~1 mm were observed in IN049 which did not exhibit a DCPD jump. Based on these observations, it seems that a critical crack size or geometry relative to specimen size may exist for this event and might be associated with a critical value in reduction of cross-sectional area and/or K value at the crack front.

A variety of microstructural processes could account for the DCPD jump because it could be due to either strain or rapid crack growth. One possible explanation is the slow formation and rapid release of dislocation pile-ups as localized strain propagates from one grain to the next, producing a strain burst [30]. Another is dynamic strain aging where an increase in stress that drives dislocation motion is caused by local changes in stress due to reduction in cross-sectional area by cracking. In either case, crack growth and coalescence could have played an important role in driving up stress and local K. Alternatively, a sudden decrease in the cross-sectional area of the gauge section could have been caused by a rapid coalescence event. A simple estimation based on how the strain rate was calculated from DCPD response was carried out to verify this hypothesis. The result revealed that in order to produce an equivalent level of strain jump observed in IN013 (0.08%) and IN048 (0.3%), an instantaneous reduction in cross-sectional area of ~1×10^5 µm^2 and ~5×10^5 µm^2 is required. For comparison, the largest cracks had a surface area of ~3×10^5 µm^2 at most, indicating that such a large reduction in cross-sectional area is unlikely to happen in these specimens that show no sign of stable fast crack growth. Additional research is clearly needed to elucidate what controls this DCPD response in the AR alloy 600 materials.

Relationship Between Microstructure and SCC Initiation Time

A variety of definitions of "SCC initiation" have been proposed ranging from microscopically small cracks that are usually less than one grain diameter to larger ones that can be detected by non-destructive examination (typically >1 mm) [31]. In this study, SCC initiation has been based on in-situ DCPD response combined with insights from specimen characterizations.

Combining DCPD strain response (Figures 14 and 40) and characterization results of crack distributions and geometries (Figures 45, 49 and 50), it seems reasonable to consider that for the CW materials, DCPD detection of SCC initiation is when one (or a few) dominant cracks begin to experience faster crack propagation. The process leading to the formation of a dominant crack is likely due to a combination of material microstructural and specimen stress factors. These factors may change as the crack progresses from one grain to the next into the specimen until the dominant cracks reach a critical depth and K prompting higher CGRs.

SCC initiation response for AR materials is much more difficult to define because of the mixed DCPD observations where some specimens have exhibited a strain jump and others have undergone a smooth but slow transition to a higher indicated strain rate. It is interesting to note that after the detection of a DCPD jump in the 1 µm finish specimens IN048 and IN013, the DCPD strain rate dropped back to a level similar to the one prior to the occurrence of the jump. This suggests that the crack evolution after the strain burst had not changed appreciably despite the presence of some large cracks exceeding 200 µm in depth. Quite differently, the DCPD responses of the IN014 and IN015 specimens showed a similar upward pattern with a much more gradual slope as those observed in the CW materials. Whether this phenomenon is the result of accelerated growth of a few dominant cracks remained unclear as these specimens have yet to be examined in cross-section. Detailed characterizations of crack depths and overall crack morphologies are continuing to better understand SCC initiation behavior in the AR materials.

While the data in this report suggest a much greater sensitivity to early crack evolution at low K values, it does indicate that the K at which SCC initiation become discernable by DCPD is closer to the ~9 MPa√m value suggested as a threshold for SCC growth [25]. Thus, the current hypothesis is that stress-assisted IGA drives the formation of shallow precursor cracks in alloy 600 and their conversion to a fully initiated SCC crack takes place when the K reaches a critical value. This more readily occurs in higher strength materials at a higher applied stress for the reasons just described and is pictorially represented in Figure 53. This description of SCC initiation is consistent with that given by LeHong [27] for a combination of constant load and constant extension rate tests.

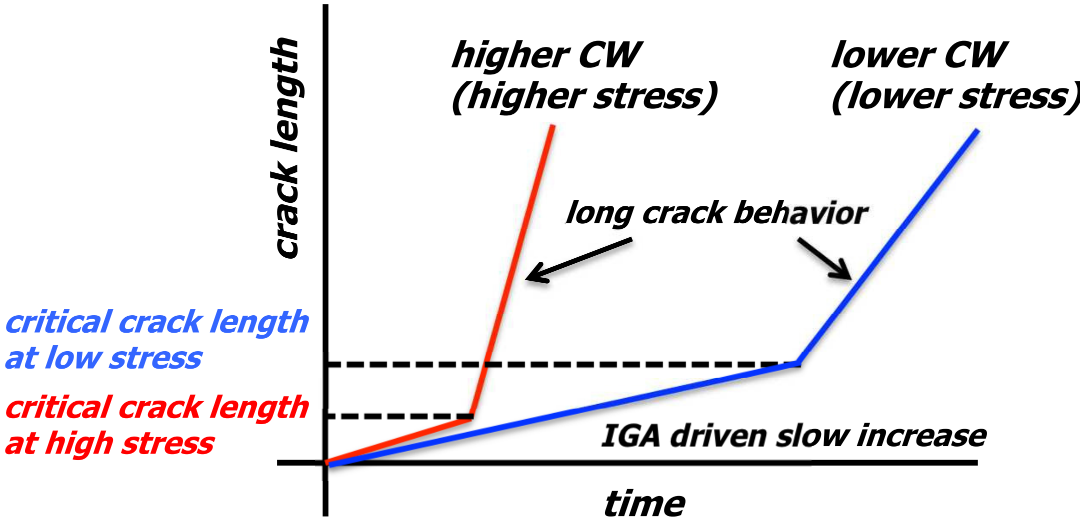

Figure 53. Qualitative representation of possible differences in initiation response between a material in a low cold work and a high cold work condition that are tested at their yield stress.

Summary Comments on Alloy 600

Considerable information has been generated from these SCC initiation tests on alloy 600. The initiation data show a strong decrease in SCC initiation time for a relatively small cold work level of 7-8% when specimens are tested at their yield strength. Preliminary examinations of cracks suggest that the initiation time detected by DCPD represents a transition to rapid crack growth that occurs after IGA and the formation of short cracks. The applied stress and crack length associated with this transition gives rise to crack tip stress intensities that are consistent with the transition to higher propagation rates measured during SCC crack growth testing of MA alloy 600. This indicates that DCPD detects the evolution from short crack to long crack behavior and is not sufficiently sensitive to detect SCC precursors or microcrack formation.

The detailed SEM characterizations and analyses presented in this chapter tracked the initiation process for two different alloy 600 heats. While the shape of large cracks differed significantly between the AR and the CW materials, consistency was found in crack shape distributions. These findings provide a better understanding of the PWSCC initiation process in alloy 600 and the detection capability of DCPD techniques. The emerging trend is that the high strength, CW specimens loaded to their yield strength exhibit a very distinct initiation point and rapid transition from precursor damage to short cracks and then to stable macroscopic SCC growth. Quite differently, the AR specimens with lower strength show a very gradual transition from precursor damage to short crack growth linking surface cracks. These specimens exhibited two different deviations from creep strain evolution, one being a step change in DCPD response and the other being an upward trend in DCPD (similar to the CW materials). The causes for the differing response are currently under investigation and will be discussed in a future report.

Estimations of K at the crack fronts suggest that a change in DCPD response may be related to a critical value being reached after cracks reach a critical shape in both aspect ratio (a/b) and relative depth (a/D). The significance of crack interaction and coalescence in SCC initiation in both AR and CW alloy 600 materials has been recognized. This phenomenon complicates the stress/strain field around crack tips and crack growth kinetics and needs to be investigated in more detail.

The determination of factors controlling SCC crack formation and evolution remain a critical focus of the ongoing and future research. More extensive destructive examinations are underway to better quantify the length, depth and distributions of IGA and initiated cracks in these alloy 600 specimens. Targeted tests will be performed to help clarify the roles of applied stress, cold work, material strength and microstructure on SCC initiation processes.

SCC initiation Tests on Alloy 690 Materials

Alloy 690 Materials Information and Specimens

Six commercial alloy 690 heats were chosen for crack initiation testing: three CRDM heats from Valinox, Sumitomo and TK-VDM (Doosan) along with three plate heats from ATI Wah Chang (ANL), ATI Allvac (GEG) and TK-VDM. Heat designations, product forms, bulk compositions and material conditions for these materials are documented in Table 7. All six of these alloy 690 heats have been extensively characterized and SCC crack-growth response has been determined [32-34] in several different CW conditions. Microstructural information is summarized in Table 8 with an emphasis on grain boundary precipitation and SCC behavior is indicated in Figures 54 and 55. The SCC plots illustrate the increase in susceptibility with the degree of cold work for the alloy 690 heats. Extremely low SCC growth rates ($\leq 10^{-9}$ mm/s) were observed in simulated PWR primary water at 360°C for AR materials, but exhibit high propagation rates ($\sim 10^{-7}$ mm/s) for materials cold worked to ~30% reduction. It is interesting to note that the rates measured for the highly CW alloy 690 heats approach the disposition curve for MA alloy 600 (Figure 54).

Table 7. Alloy 690 Materials for SCC Initiation Testing

Material and Heat Number	Description	Composition, wt%	Heat Treatments and Cold Work Level
Valinox Alloy 690TT RE243	CRDM Tube 2360 1.4” wall	Ni-28.9Cr-10.4Fe-0.02C-0.3Mn-0.35Si-0.14Al-0.23Ti-0.024N-0.008P-0.0005S	1122°C/~1 min, WQ + 716-725°C/10.5 h, air cool 12.7%, 21%, 31%CF
Sumitomo Alloy 690TT E67074C	CRDM Tube 1.31” wall	Ni-29.8Cr-9.8Fe-0.020C-0.29Mn-0.23Si-0.0002S	725°C/10 h/AC 21%, 31%CF
TK-VDM (Doosan) Alloy 690TT 133454	CRDM Round Bar 6.0” OD	Ni-29.1Cr-8.9Fe-0.020C-0.26Mn-0.29Si-0.26Al-0.32Ti-0.02N-0.005P-<0.002S	1045°C/3.9 h/WQ + 720°C/10 h/AC 21.6%, 31%CF
ANL Alloy 690MA NX3297HK12	ATI Wah Chang 2.125” Plate	Ni-30.8Cr-8.5Fe-0.04C-0.33Mn-0.02Si-0.18Al-0.27Ti-0.037N-0.0006S-0.006P	1038°C/2 h, air cool 26%CR
GEG Alloy 690MA B25K	ATI Allvac 3.25” Plate	Ni-29.3Cr-9.2Fe-0.034C-0.22Mn-0.06Si-0.26Al-0.37Ti-0.026N-0.006P-<0.0003S	996°C/0.33 h, air cool 12.4%, 18.3%CF
TK-VDM Alloy 690TT 114092	Plate	Ni-29.2Cr-9.5Fe-0.020C-0.25Mn-0.26Si-0.32Al-0.36Ti-<0.002S-0.003P	1030°C/1.08 h/WQ + 715°C/10 h/AC 21%, 31.9%CF

Table 8. Microstructure for Alloy 690 Materials

Sample	Microstructure
Valinox CRDM Tube Alloy 690TT RE243	Equiaxed, large grains (~90 µm in diameter); semi-continuous (discrete + cellular) IG carbides and Cr depletion to ~21 wt%, few IG and matrix TiN
Sumitomo CRDM Tube Alloy 690TT	Equiaxed, smaller grains (~35 µm in diameter) with twins; Semi-continuous (discrete + occasional cellular) IG carbides; isolated matrix TiN
TK-VDM (Doosan) CRDM Bar Alloy 690TT	Equiaxed, large grains (~90 µm in diameter); semi-continuous IG carbides; isolated matrix TiN
GEG Bar Alloy 690MA B25K	Small grains (~15 µm in diameter); well-spaced IG carbides and no grain boundary Cr depletion, higher density in banded areas, IG and matrix TiN
ANL Plate Alloy 690MA NX3297HK12	Moderate sized grains (~50 µm in diameter) in general with regions of compositional banding; semi-continuous IG carbides and grain boundary Cr depletion to ~22 wt%, IG and matrix TiN
TK-VDM Plate Alloy 690 TT	Equiaxed, smaller grains (~30 µm in diameter); semi-continuous IG carbides, matrix TiN

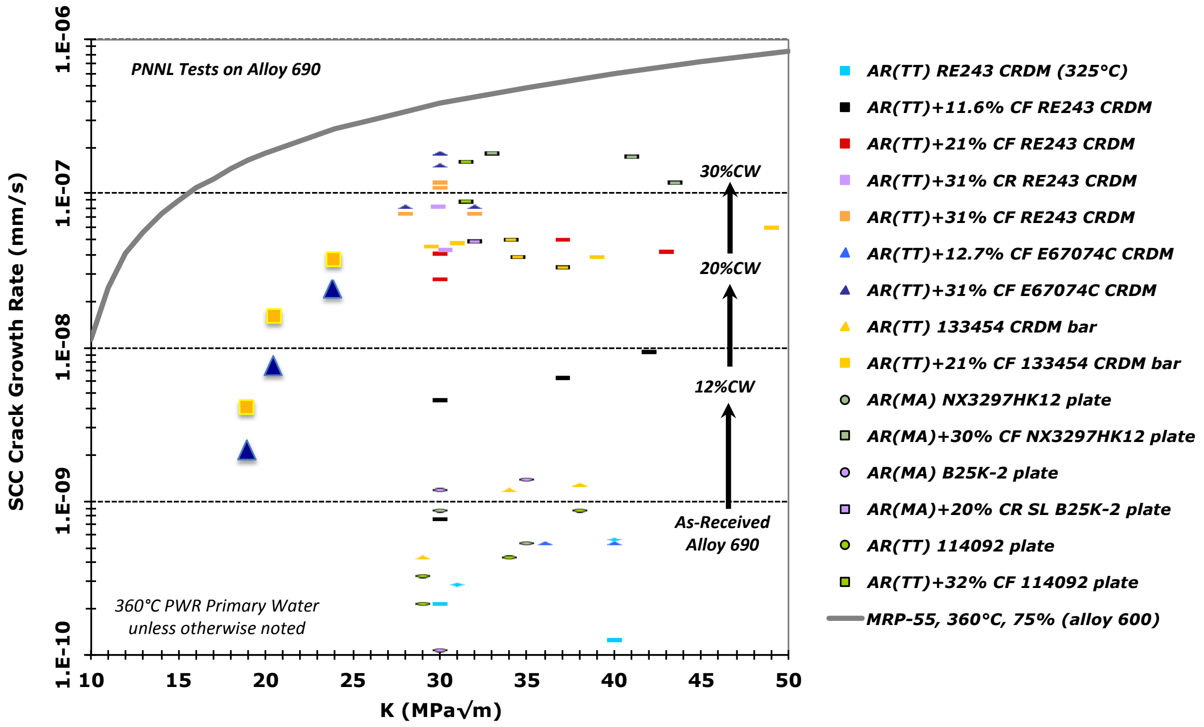

Figure 54. Measured SCC propagation rates in PWR primary water as a function of K for the alloy 690 heats being evaluated for SCC initiation response.

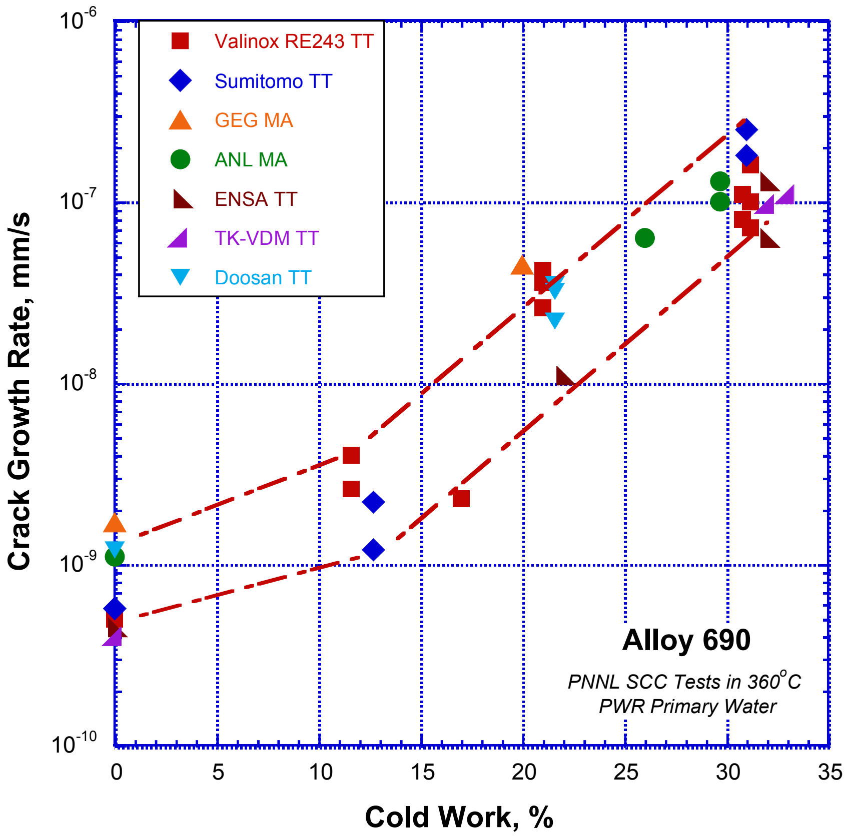

Figure 55. Measured SCC propagation rates in PWR primary water as a function of cold work level for the alloy 690 heats being evaluated for SCC initiation response.

Approach for SCC Initiation Testing for Alloy 690

As described earlier in this report, crack initiation of CW alloy 600 was successfully detected in less than ~2000 hours while AR non-CW alloy 600 required longer test times. First observations of SCC initiation for a non-CW alloy 600 were ~3800 hours for the very susceptible CRDM service material, in comparison to 6000-7500 hours for the MA plate material. Measured SCC growth rates for these two alloy 600 heats were presented (Figure 21) and discussed earlier revealing that the service CRDM heat (M3925) response with *K* was very similar to the MRP-55 disposition curve. The MA plate heat exhibited lower propagation rates particularly at lower *K* levels important to SCC initiation behavior. Because highly CW alloy 690 can exhibit SCC growth rates comparable to AR alloy 600, it was decided to begin alloy 690 crack initiation testing on highly CW materials. The intent for the first tests was to start with materials highly susceptible to SCC and run them at high stress (equal to their yield stress) to produce a baseline minimum crack initiation time for alloy 690. After long-term testing at constant load did not produce crack initiation, alternate testing conditions were considered. Because unstressed samples were observed to form a protective Cr_2O_3 film formed at grain boundaries intersecting the surface, it was decided to evaluate dynamic straining as a means to accelerate the formation of precursor surface cracks. First tests were performed with periodic loading ramps to produce very small amounts of plastic tensile extension. Other methods (load cycling within the elastic strain region and slow, continuous plastic straining) were also explored on CW alloy 690 specimens and were described in a previous report [3].

Another aspect of the crack initiation testing approach on alloy 690 has been periodic inspections of the specimens to look for initiation precursor microstructures, in particular, to look for small cracks that might not yet have been detected by DCPD. Examinations were initially limited to documenting the surface of the gauge section using SEM, however after small cracks had nucleated from corroded TiN particles, it was decided to employ focused ion beam (FIB) milling to create shallow trenches to probe the structure of these cracks in cross-section. The trenches were quite small, typically ~5-10 μm wide in both directions on the surface and ~5 μm deep, and present minimal if any stress riser on the specimen or the crack. This technique enables surface and near-surface SCC precursor damage to be investigated without destructive sectioning that would render continued testing impossible.

Blunt Notch SCC Initiation Tests on Cold-Worked CRDM Specimens

Mechanisms controlling crack initiation in CW alloy 690 are also being evaluated using blunt-notch CT specimens at GEG under a PNNL subcontract. Standard 0.5T CT specimens are used, but the notch tip is "wet ground" to a ~0.75 mm radius using a diamond wheel and given a final polish at PNNL to a 1 μm diamond finish. This created a well-controlled surface matches the surface condition for the tensile specimens from which crack initiation can better resolved by SEM examinations of the notch and compared to in-situ DCPD measurements. First tests were performed last year on two 31%CF alloy 690 CRDM specimens, c672 (Valinox heat RE243) and c673 (Sumitomo heat E67074C) provided by PNNL and tested in series. Preliminary results on these specimens were described in a previous report [3], however aspects will be reviewed here for comparisons to the new blunt notch experiments. Overall test response for blunt notch specimens c672 and c673 is presented in Figures 56 and 57 showing DCPD-measured crack length versus test time. After confirming a lack of SCC nucleation and growth at the baseline K of 27.5 MPa√m (pseudo K assuming a tight crack rather than a blunt notch), several load ramps between 27.5 and 44 MPa√m were applied. The 31%CF Valinox specimen c672 exhibited a change in crack-growth rate during the 3rd hold at ~2050 hours (Figure 56). Crack initiation clearly occurred, and the growth rate evolved from ~$6x10^{-9}$ to $2.5x10^{-8}$ mm/s as the crack developed. Similar behavior was observed for the 31%CF Sumitomo specimen c673 that showed a change in crack-growth rate during the 3rd hold at ~2200 hours. The growth rate evolved from ~$3x10^{-9}$ to $1.8x10^{-8}$ mm/s as the crack developed. Unfortunately, the test was not stopped at this point to investigate the blunt notch surface for evidence of cracks, and a 4th cycle was applied. This produced a significant increase in the DCPD-measured crack growth rates likely due to sharp increase in the depth of cracks. The test was ended after 2560 hours and specimens were sent to PNNL for optical and SEM examinations.

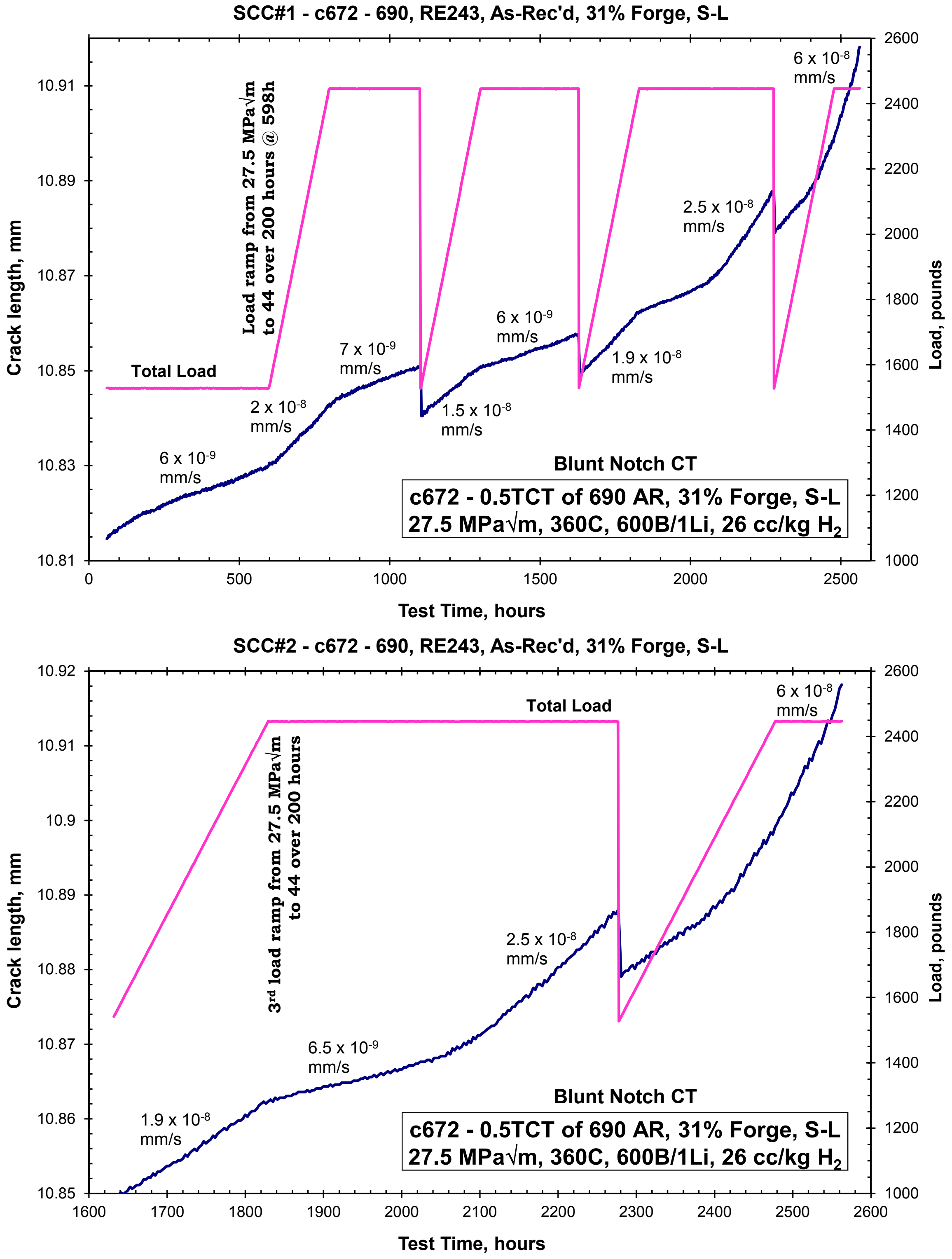

Figure 56. Crack length versus time response for the 31%CF Valinox CRDM specimen c672 blunt notch specimen.

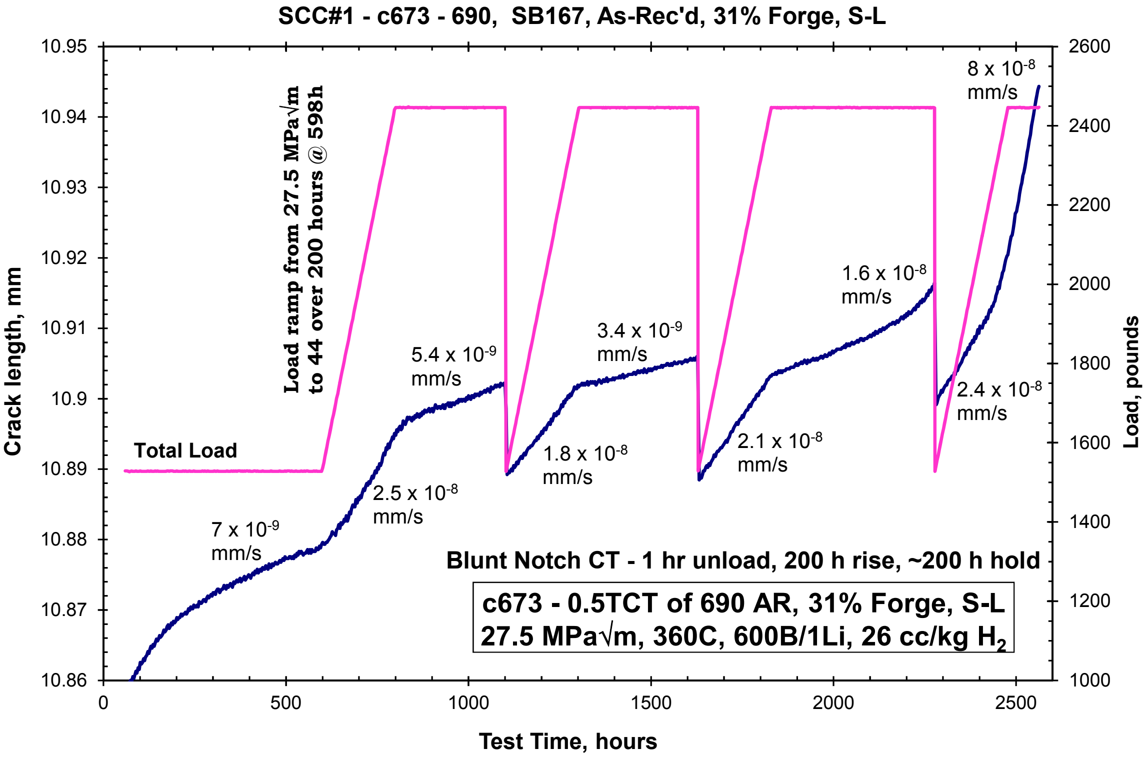

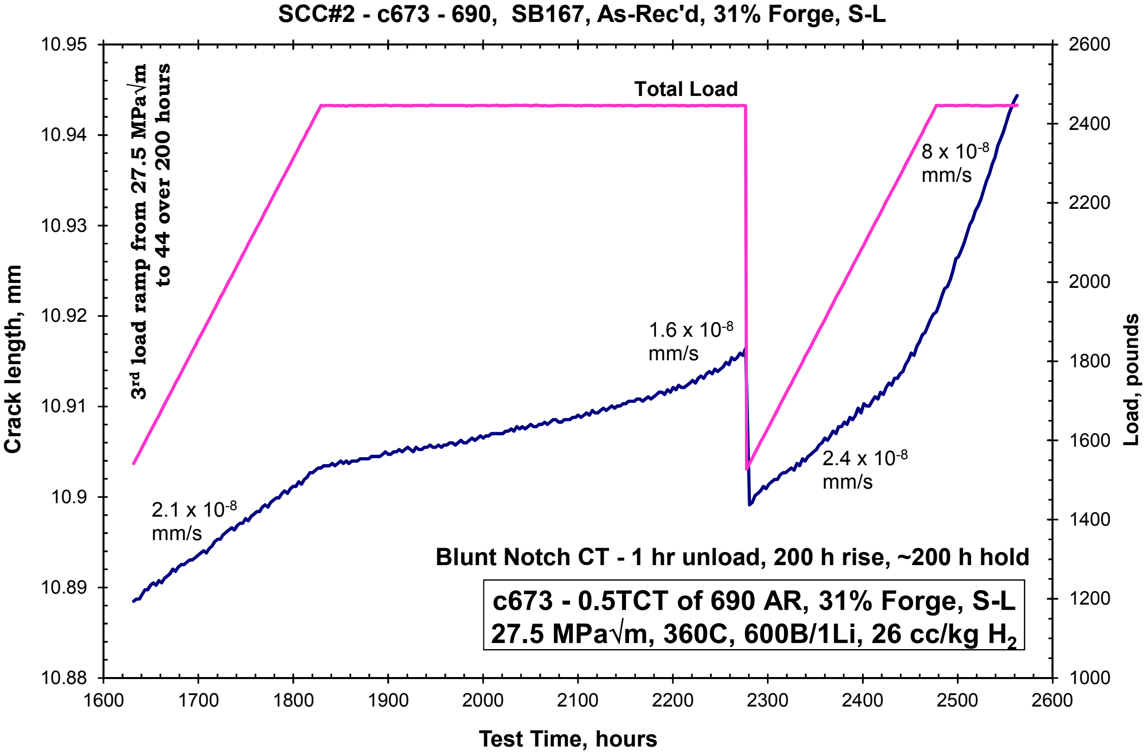

Figure 57. Crack length versus time response for the 31%CF Sumitomo CRDM specimen c673 blunt notch specimen.

Cracks were readily identified by SEM-BSE imaging on the polished notch surfaces for the c672 and c673 specimens. Crack distributions from a single area on both specimens were documented as indicated in Figures 58 and 59 with individual cracks further highlighted in red. In order to better illustrate the morphology and size of the surface cracks, higher magnification images are presented in Figures 60 and 61 for specimen c672 and in Figures 62 and 63 for specimen c673. The cracks are clearly IG and surface features suggest significant deformation had occurred during crack nucleation.

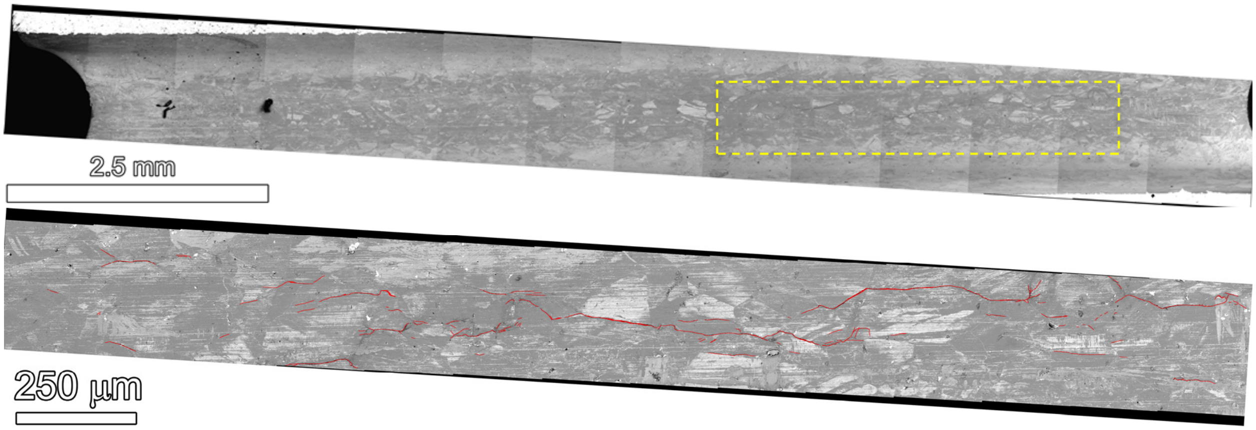

Figure 58. SEM-BSE montage of a) the entire notch of c672 (31%CF Valinox CRDM) and b) a selected higher magnification montage of the dashed yellow box in a) showing cracks.

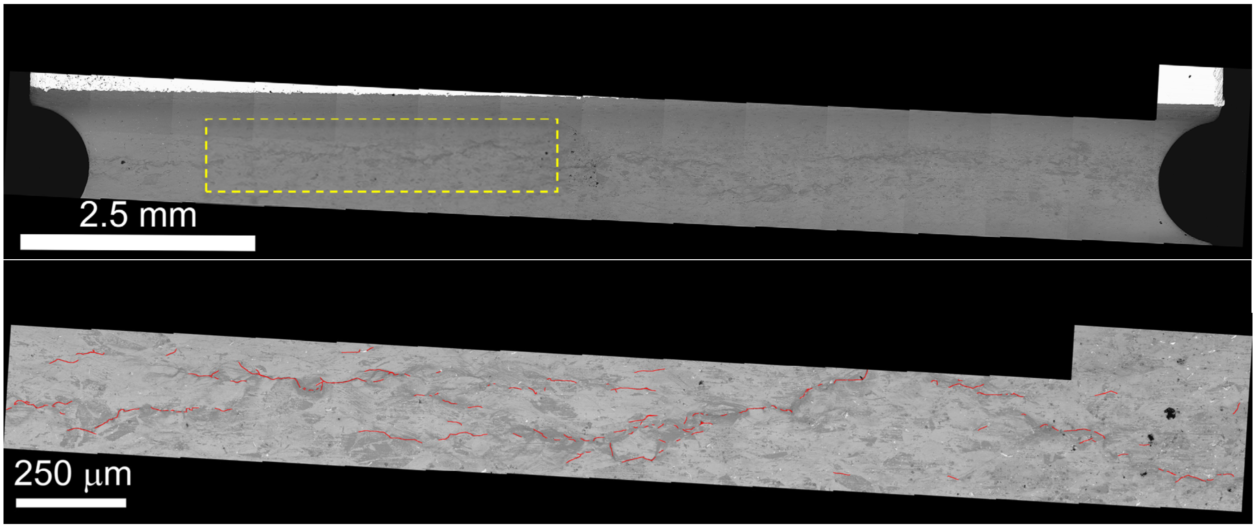

Figure 59. SEM-BSE montage of a) the entire notch of c673 (31%CF Sumitomo CRDM) and b) a selected higher magnification montage of the dashed yellow box in a) showing cracks.

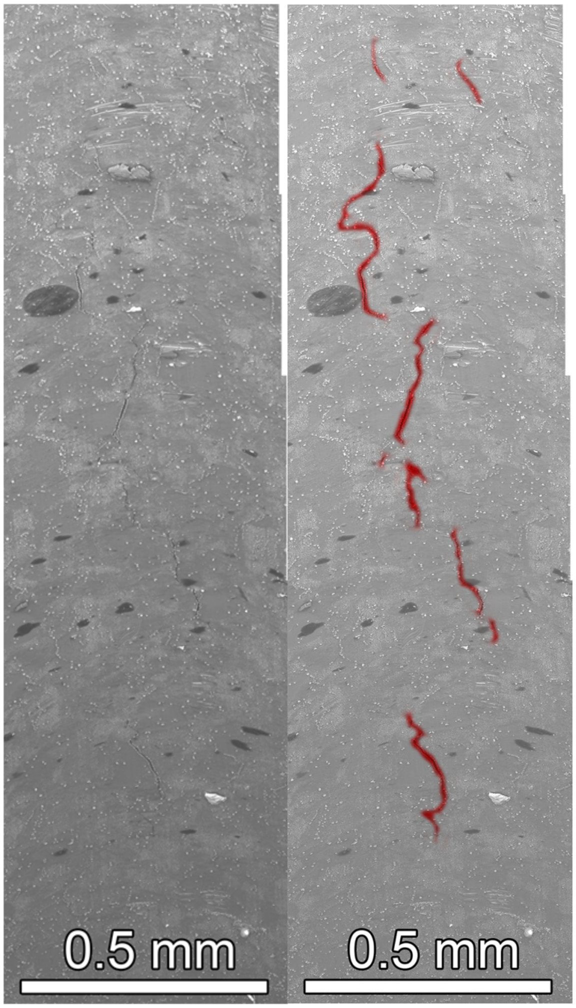

Figure 60. SEM-SE image of a portion of the 31%CF Valinox CRDM specimen c672 notch showing several nucleated cracks (highlighted by red marker in right image). Note that the image was taken at an oblique angle.

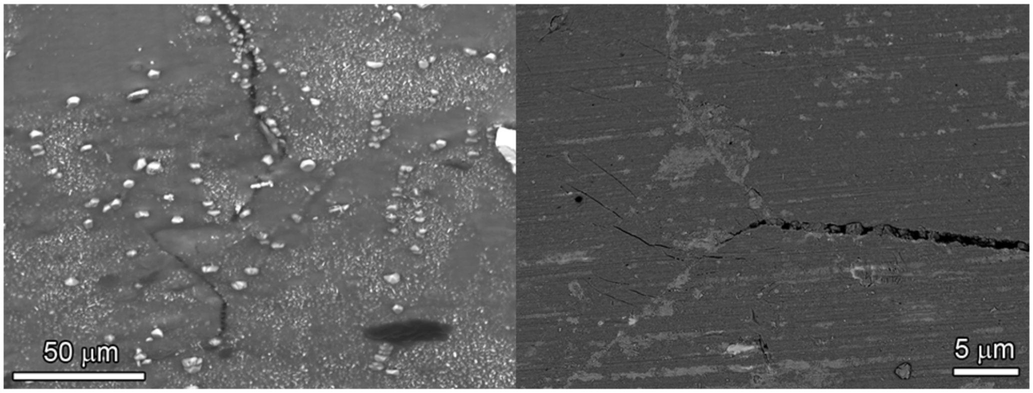

Figure 61. Higher magnification SEM-SE images showing cracks on the notch surface of the 31%CF Valinox CRDM specimen c672.

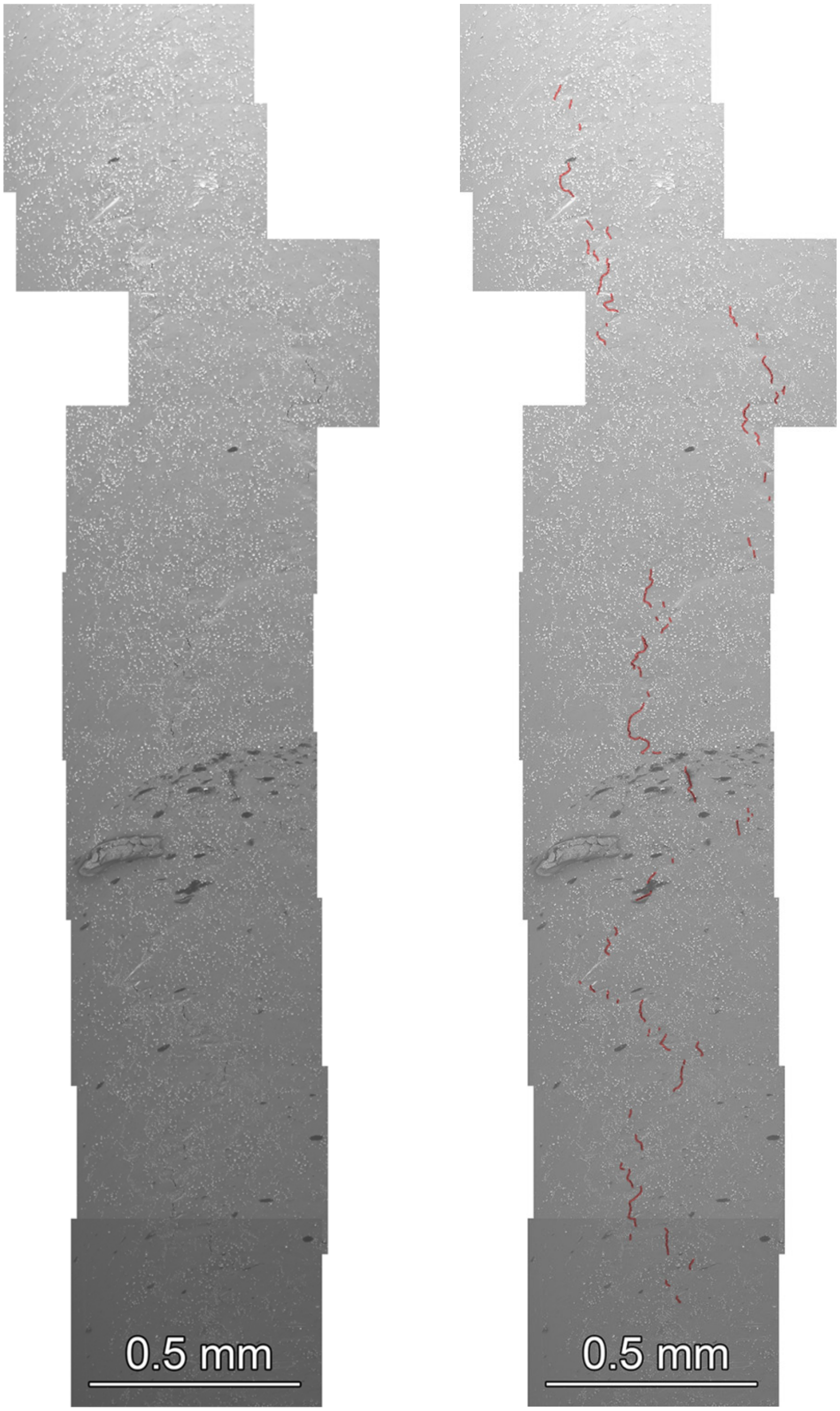

Figure 62. SEM-SE image of a portion of the 31%CF Sumitomo CRDM specimen c673 notch showing several nucleated cracks (highlighted by red marker in right image).

Electrospark discharge machining (EDM) sectioning was then performed to obtain 5 slices (each ~2 mm thick), equally spaced across the thickness of the specimen so that subsurface cracks could be mapped in cross-section.

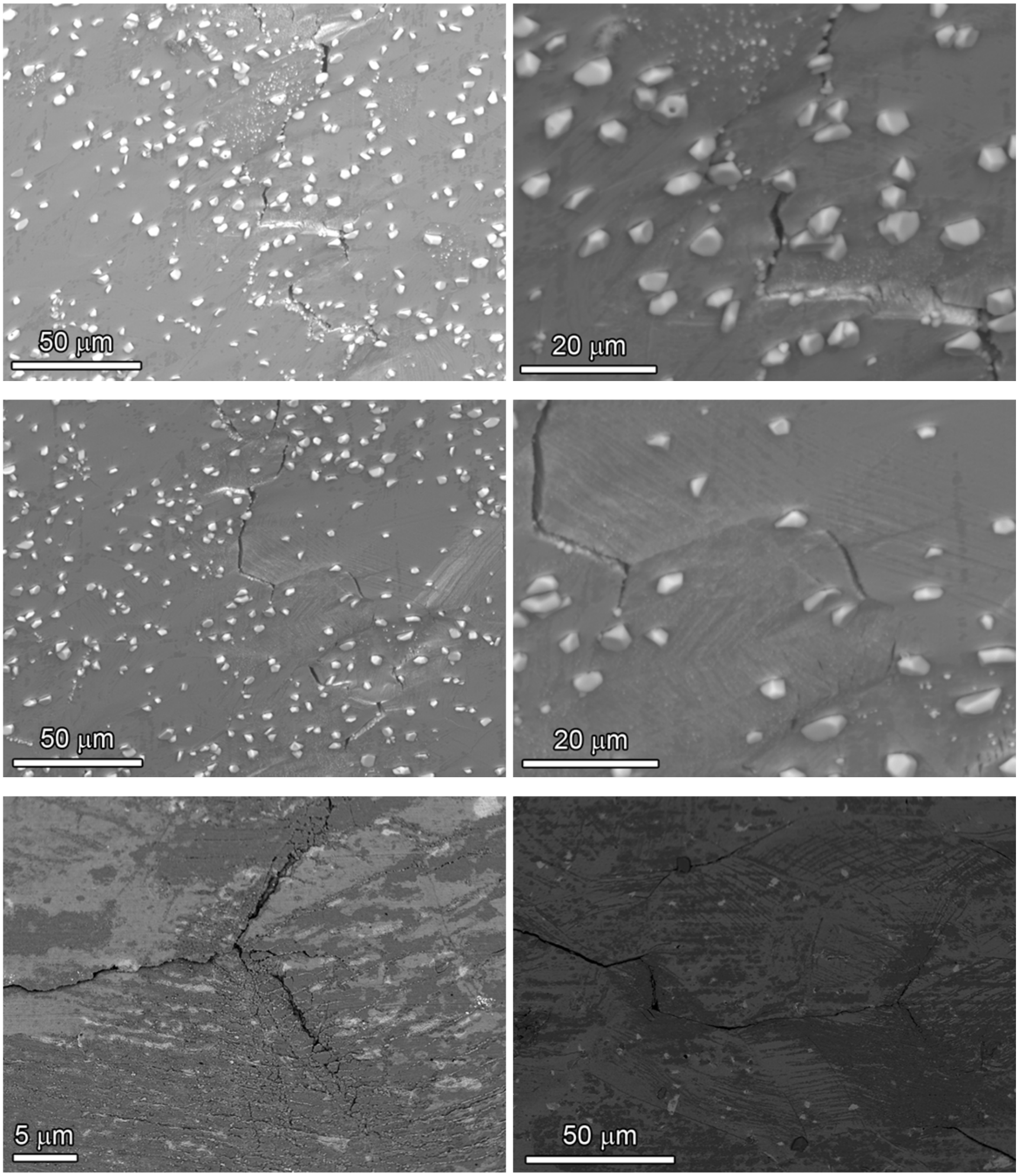

Figure 63. Higher magnification SEM images showing cracks on the notch of 31%CF Sumitomo CRDM specimen c673.

SEM-BSE and optical images for the 5 cross-sections are shown in Figures 64 and 65 for c672 and c673, respectively. Much more extensive cracking can be seen for specimen c673 (Figure 65) particularly with slices 1-4 showing major cracks that had propagated to a depth >0.3 mm. This is in comparison to specimen c672 (Figure 64) where only side 3 revealed deep IG cracks during these low magnification characterizations.

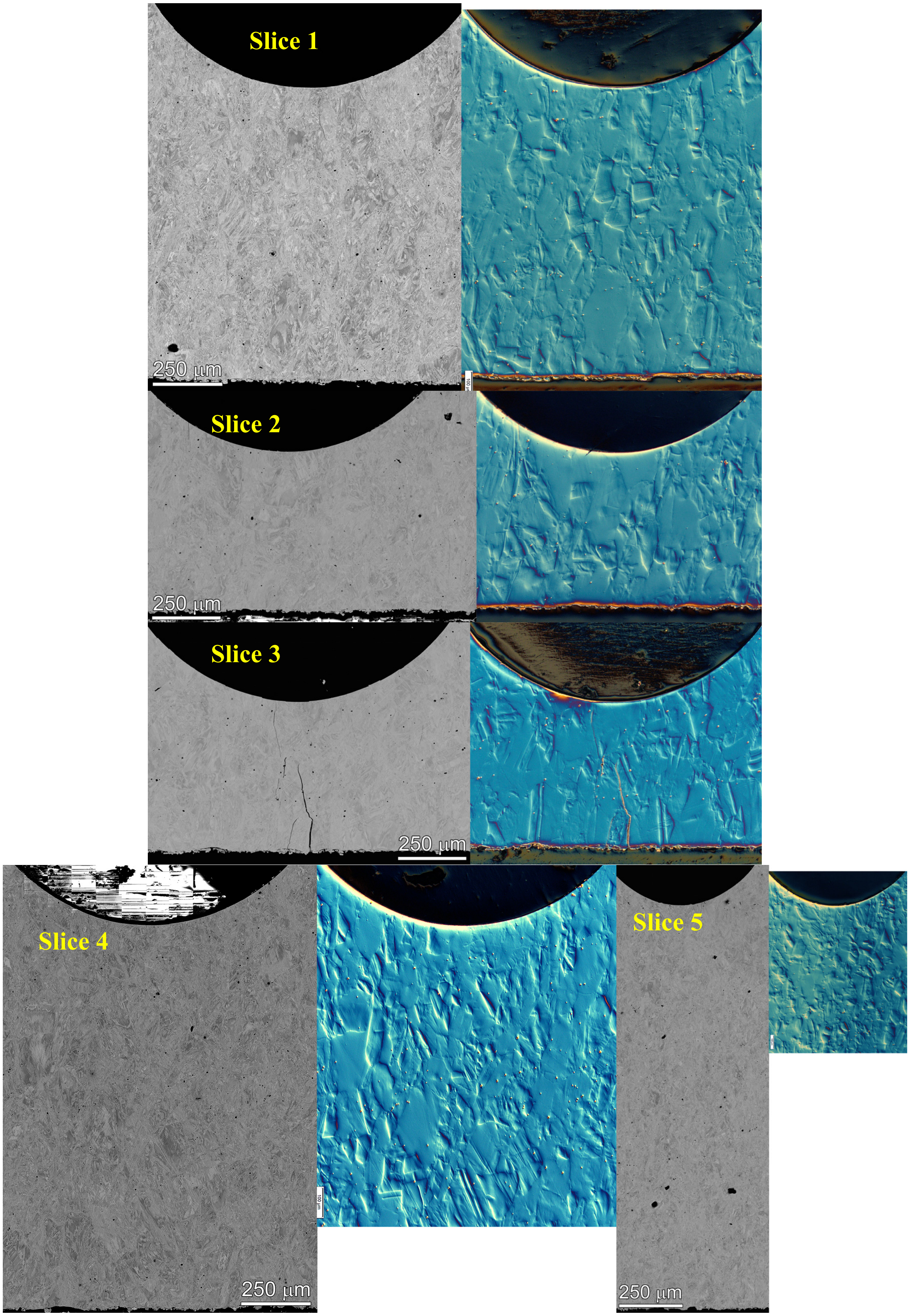

Figure 64. SEM-BSE and optical micrographs of five cross-sections slices in c672.

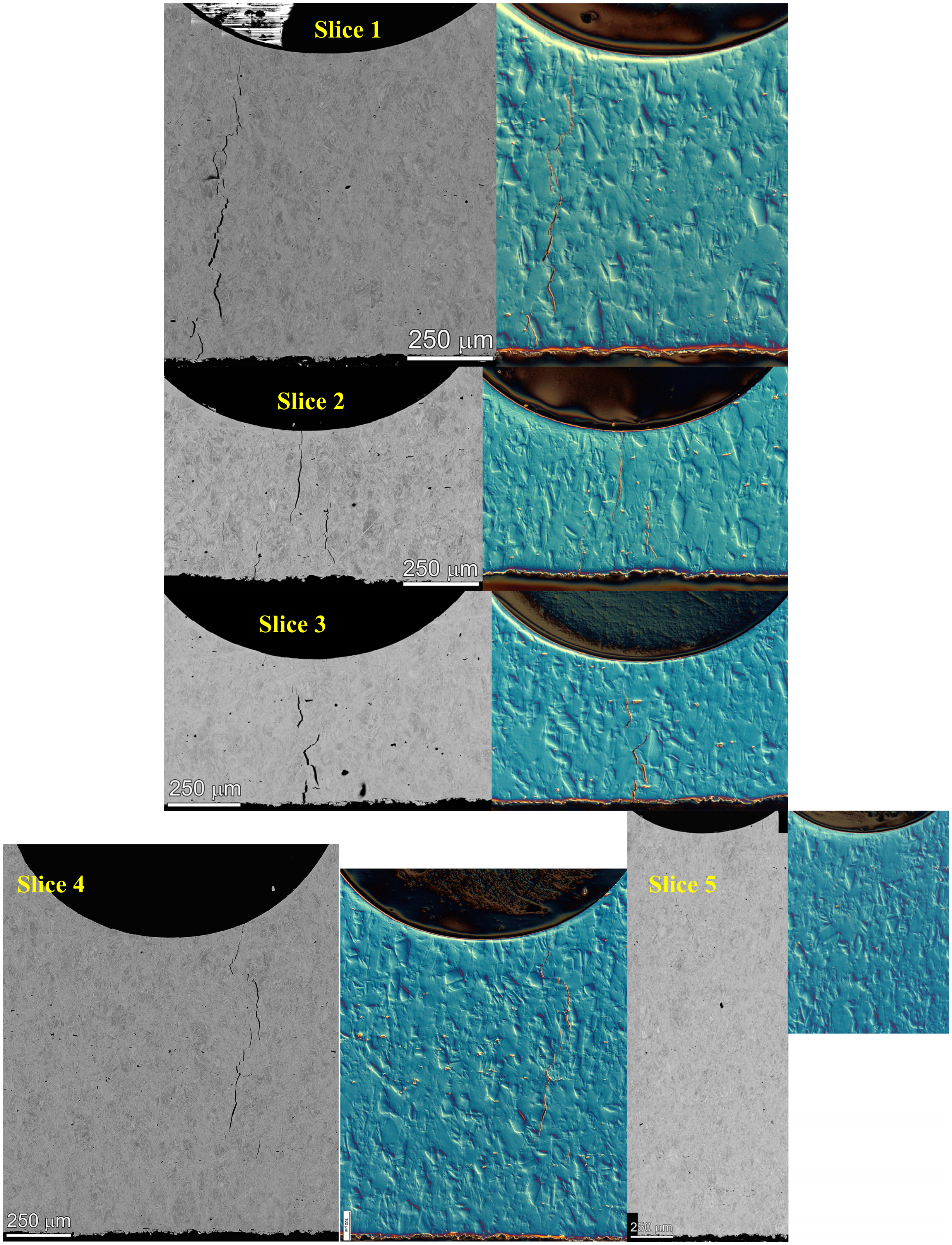

Figure 65. SEM-BSE and optical micrographs of five cross-section slices in c673.

Closer examinations of crack characteristics were made at higher magnifications and identified two fundamentally different types of cracks. Typical examples of these cracks are shown in Figure 66 from the c672 cross-section slice #1. Larger and more open cracks were found to have obvious crack wall oxidation and crack-tip structures consistent with that expected for SCC cracks. Crack-wall penetrative oxidation nanostructures and sharp IG crack tips are illustrated in Figure 67. These characteristics are entirely consistent with our previous measurements on IGSCC tips from crack-growth test specimens. The second type of crack present was quite different as documented in Figure 68. These cracks were found at distances >100 µm from the notch surface and were reasonably tight with evidence for grain boundary cavity formation. Most important is that there was no evidence for corrosion/oxidation along the crack walls indicating that these cracks had not been exposed to high-temperature water. Because of these features, they have been identified as IG "creep" cracks and were found in most cross-sections. Two other examples are shown in Figures 69 and 70. Cavities can be seen at the crack tip region that formed at the grain boundary - carbide interfaces, and the evidence for the cavities is present along the main crack in the form of a dimpled appearance. It seems clear that creep cavitation and cracking occurred during the blunt notch loading ramps.

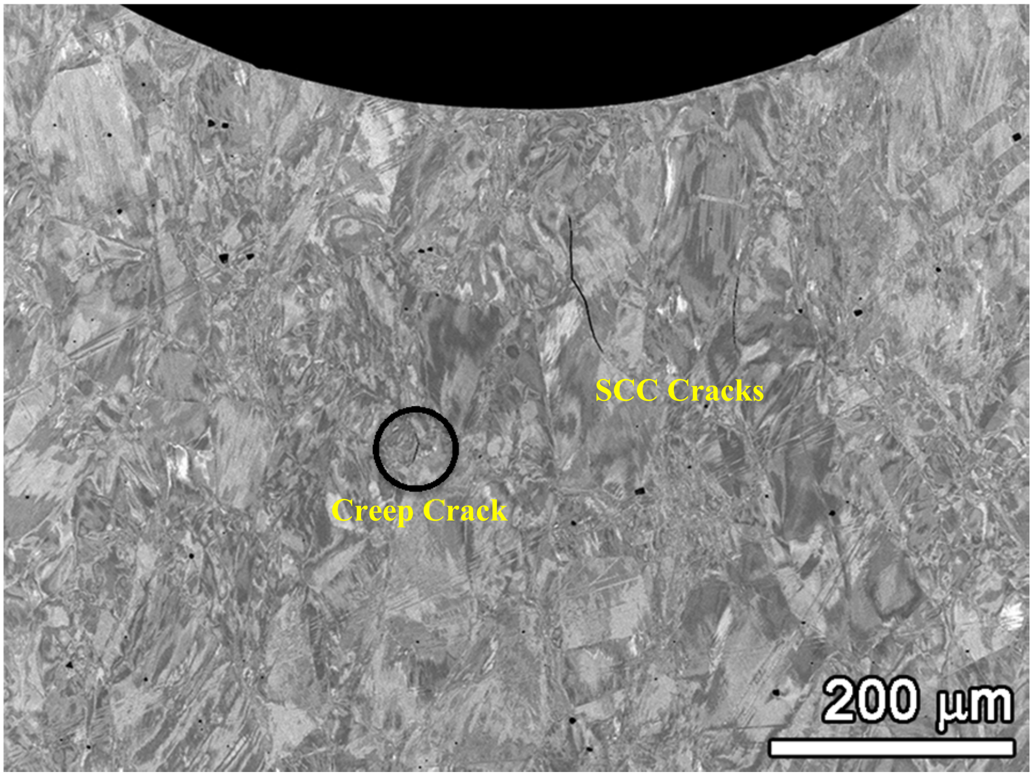

Figure 66. Blunt notch c672 cross-section slice #1 showing what are identified as SCC and creep cracks.

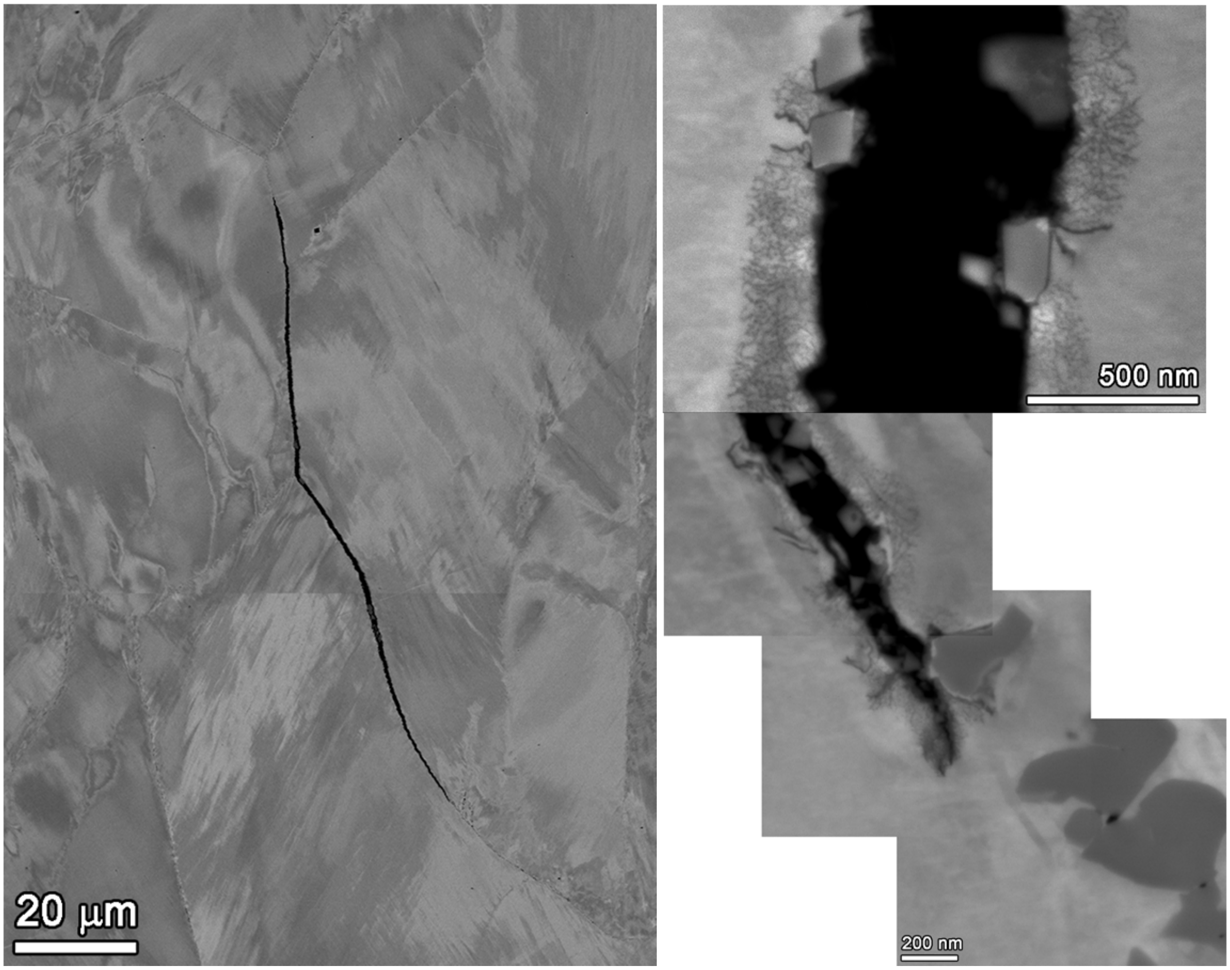

Figure 67. IGSCC crack in blunt notch specimen c672 cross-section slice #1 that clearly shows crack wall and crack tip corrosion.

Figure 68. Apparent creep cracks in blunt notch specimen c672 cross-section slice #1 showing no evidence for corrosion or oxidation along the crack walls.

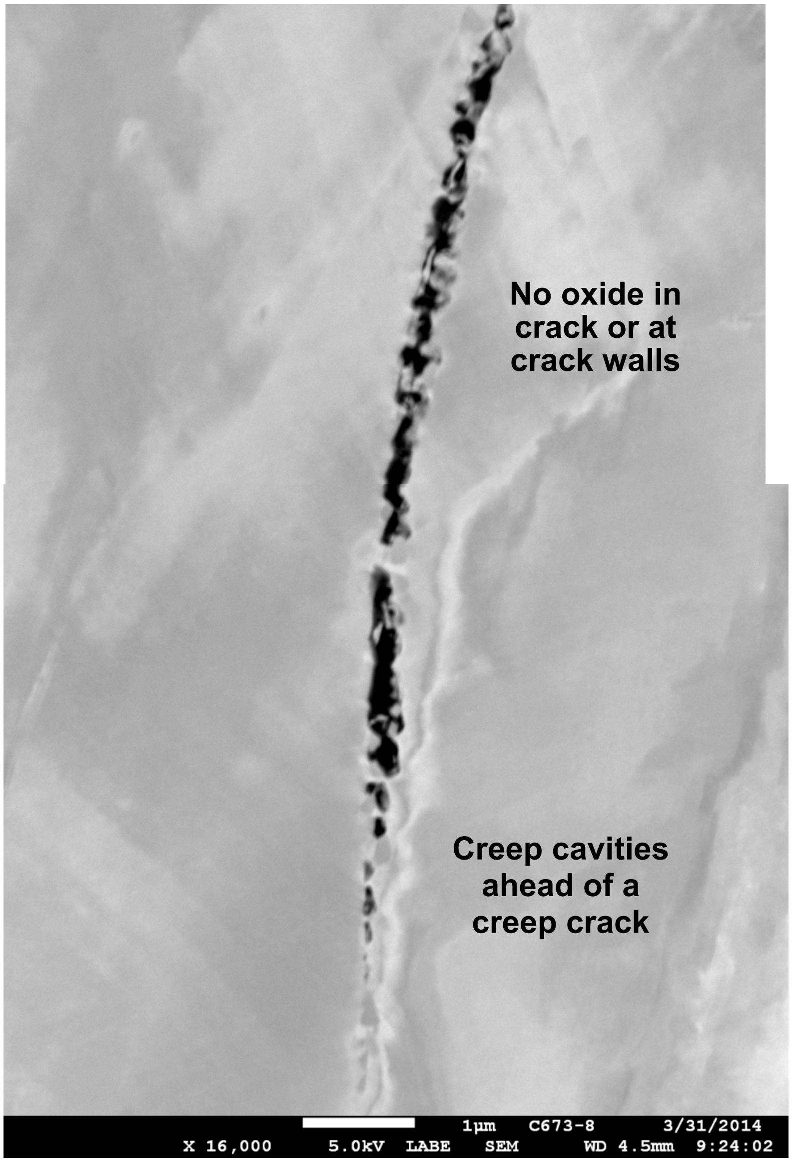

Figure 69. Example of IG creep crack and cavities in cross-section slice #2 from blunt notch specimen c672.

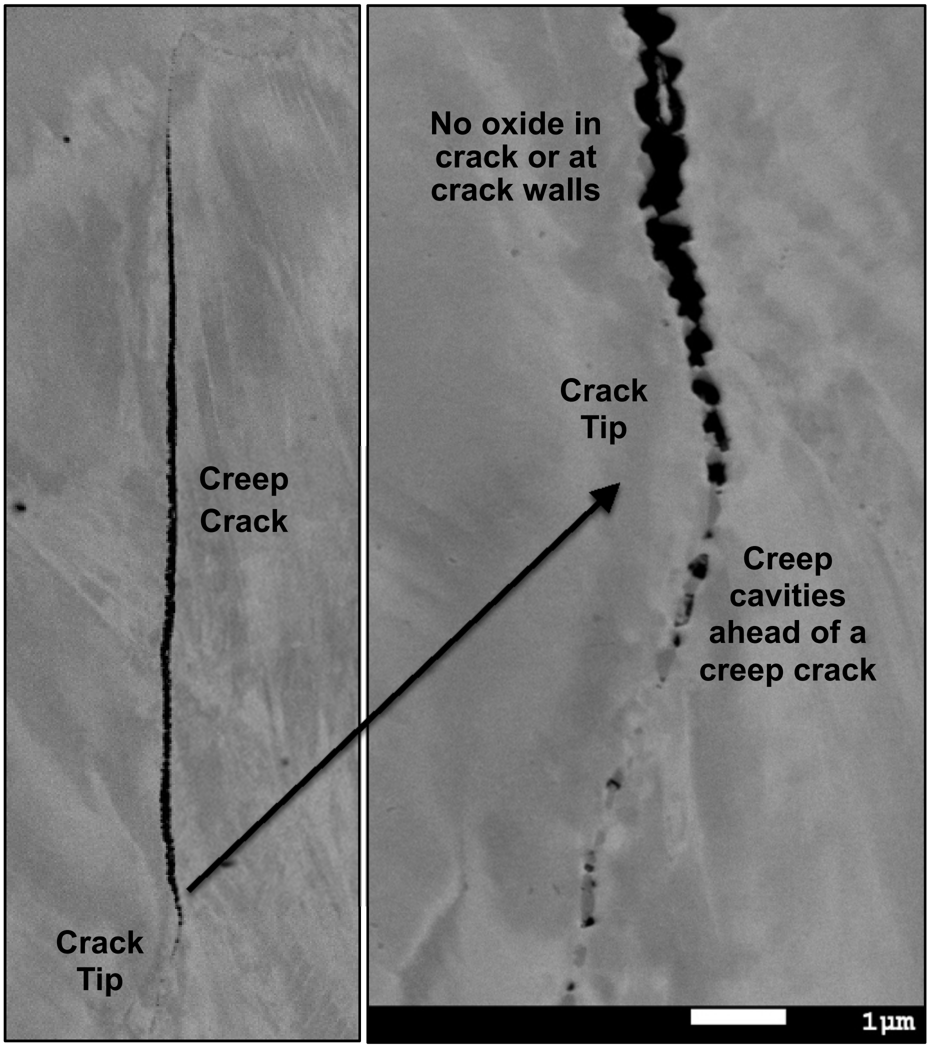

Figure 70. SEM-BSE cross-section image of c673 slice #4 showing creep crack tips. This slice had many large SCC cracks.

An important question is whether creep cracking is responsible for the SCC crack formation and growth observed in the blunt notch tests through a process whereby either a creep crack grows to the surface or creep cracks near the surface increase the local *K* and promoting formation of IGSCC cracks from the surface. To get a better assessment of the creep crack distributions, their locations were mapped on several cross-sections as presented in Figures 71 and 72 for c672 and c673, respectively. Small creep cracks are identified across the notch with a few close to the surface, however most were found at a distance >100 µm below the surface.

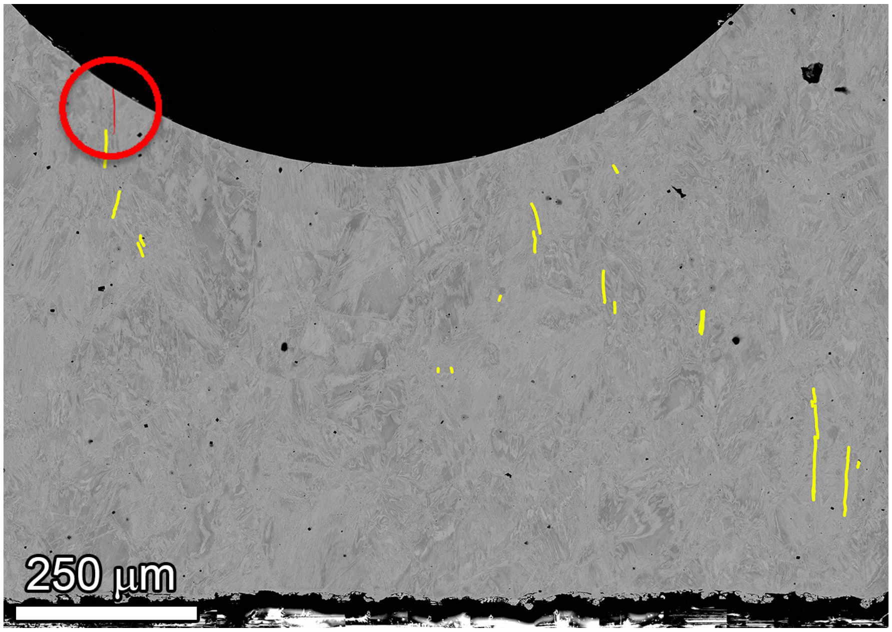

Figure 71. SEM-BSE image of c672 cross-section slice #2 showing cracks identified as SCC (red) and creep (yellow).

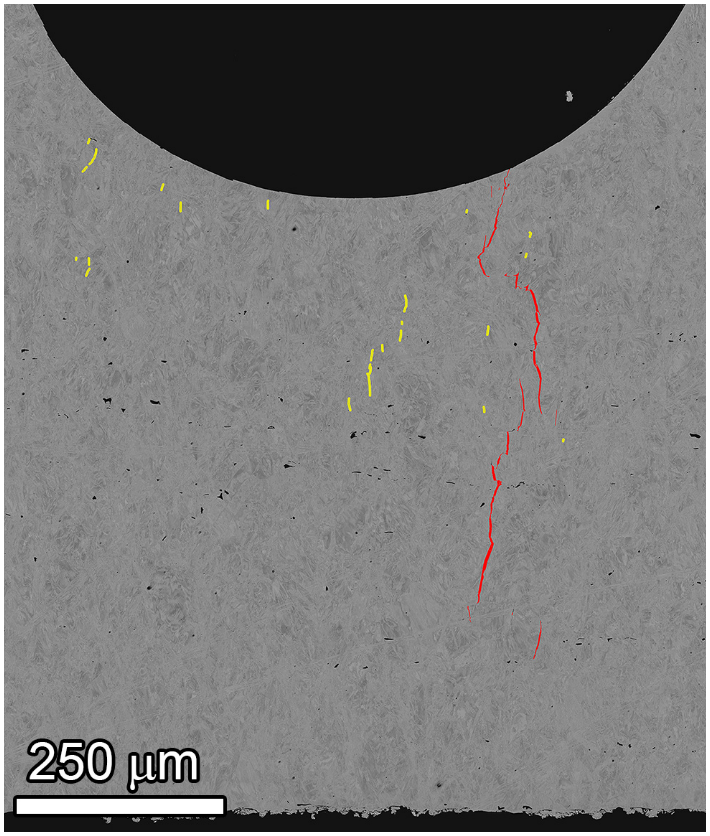

Figure 72. SEM-BSE image of c673 cross-section slice #4 showing cracks identified as SCC (red) and creep (yellow).

In order to better understand how the loading ramps employed in these blunt notch tests can produce such extensive creep cavitation and cracking, a second series of blunt notch experiments were started at GEG in late 2014. Once again, the 31%CF Valinox CRDM and 31%CF Sumitomo CRDM materials were selected along with these same heats in the ~21%CF condition. In an effort to affect the degree of creep cavity formation, the decision was made to limit the strain level to 0.5% for each ramp. Finite element modeling was performed again to estimate the plastic strain generated during slow loading ramps, and the decision was made to reduce the maximum pseudo-K level to 36 MPa√m (previous was 44 MPa√m) to obtain this strain. The two 31%CF specimens (c703 and c704) are being tested in one test system, while the two 21%CF specimens (c707 and c708) are in a second test system. Measured DCPD response for the 31%CF specimens is summarized in Figure 73 and for the 21%CF specimens in Figure 74. The general experimental approach was the same for all specimens - they were equilibrated for several weeks in 360°C PWR primary water followed by initial observation at 27.5 MPa√m for ~1000 hours. The K level was slowly increased to 36 MPa√m over ~200 hours at ~1500 hours, and specimens were held at this higher K for a period of time that increased for each subsequent loading ramp. After establishing the DCPD-indicated crack growth behavior at constant K, a loading ramp was reapplied by first quickly dropping load back to a K level of 27.5 MPa√m and again slowly increasing load to 36 MPa√m over ~200 hours. This sequence was repeated 4 times as shown in Figure 73 for c703/c704 and in Figure 74 for c707/c708. After a final loading ramp at ~4000 hours, constant K conditions were again established and held for ~1300 hours. Quite different than observed in the c672 and c673 specimens that underwent 1.0% plastic strain ramps, DCPD response revealed no indication of crack initiation and growth in these specimens with 0.5% plastic strain ramps. The test on c703/c704 was stopped at 5325 hours and c707/708 were stopped at 5542 hours. All four specimens were removed and sent to PNNL for detailed SEM characterizations of the blunt notch surfaces.

Preliminary examinations again focused on the polished notch surfaces. Small cracks were readily identified on the 31%CF c703 and c704 specimens by SEM-BSE imaging along with other features that were considered to possible small cracks. An overall montage of the blunt notch surface for the Valinox c703 specimen is presented in Figure 75(a) with obvious cracks highlighted in red and possible cracks highlighted in green. Examples of these surface features are given at higher magnification in Figure 75(b) and (c). While these surface cracks are much smaller and less extensive than those documented on c672 and c673, it is clear that crack nucleation had occurred, and the decision was made to section part of the specimen for more detailed characterizations. The yellow band shown across one side of the montage indicates the material that was removed during sectioning, leaving ~30% of the width for cross-section analyses (left of yellow) and the other 70% for further blunt notch SCC testing.

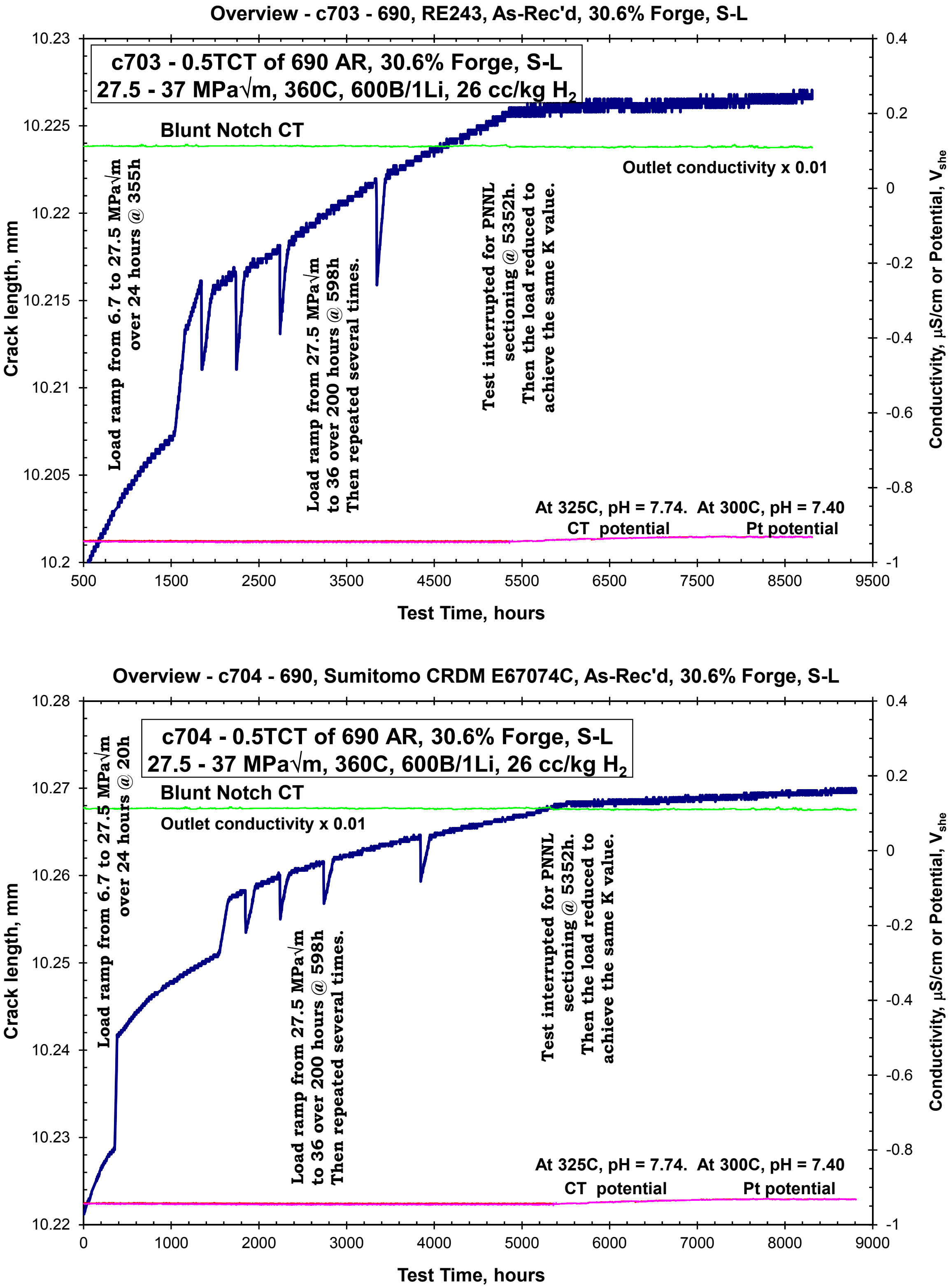

Figure 73. Overall crack length versus time response for the 31%CF Valinox CRDM (c703) and 31%CF Sumitomo CRDM (c704) blunt notch specimens.

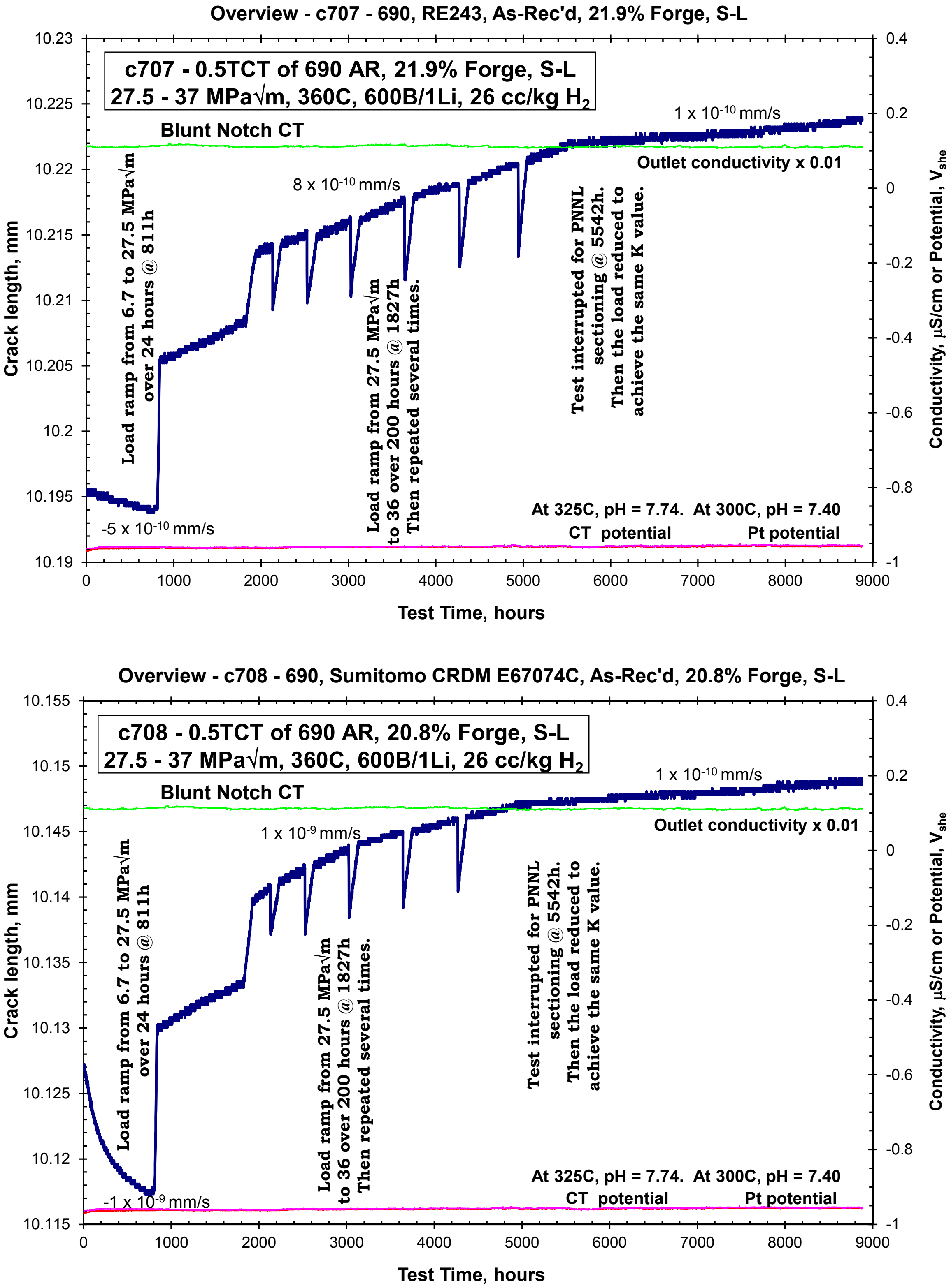

Figure 74. Overall crack length versus time response for the 21%CF Valinox CRDM (c707) and 22%CF Sumitomo CRDM (c708) blunt notch specimens.

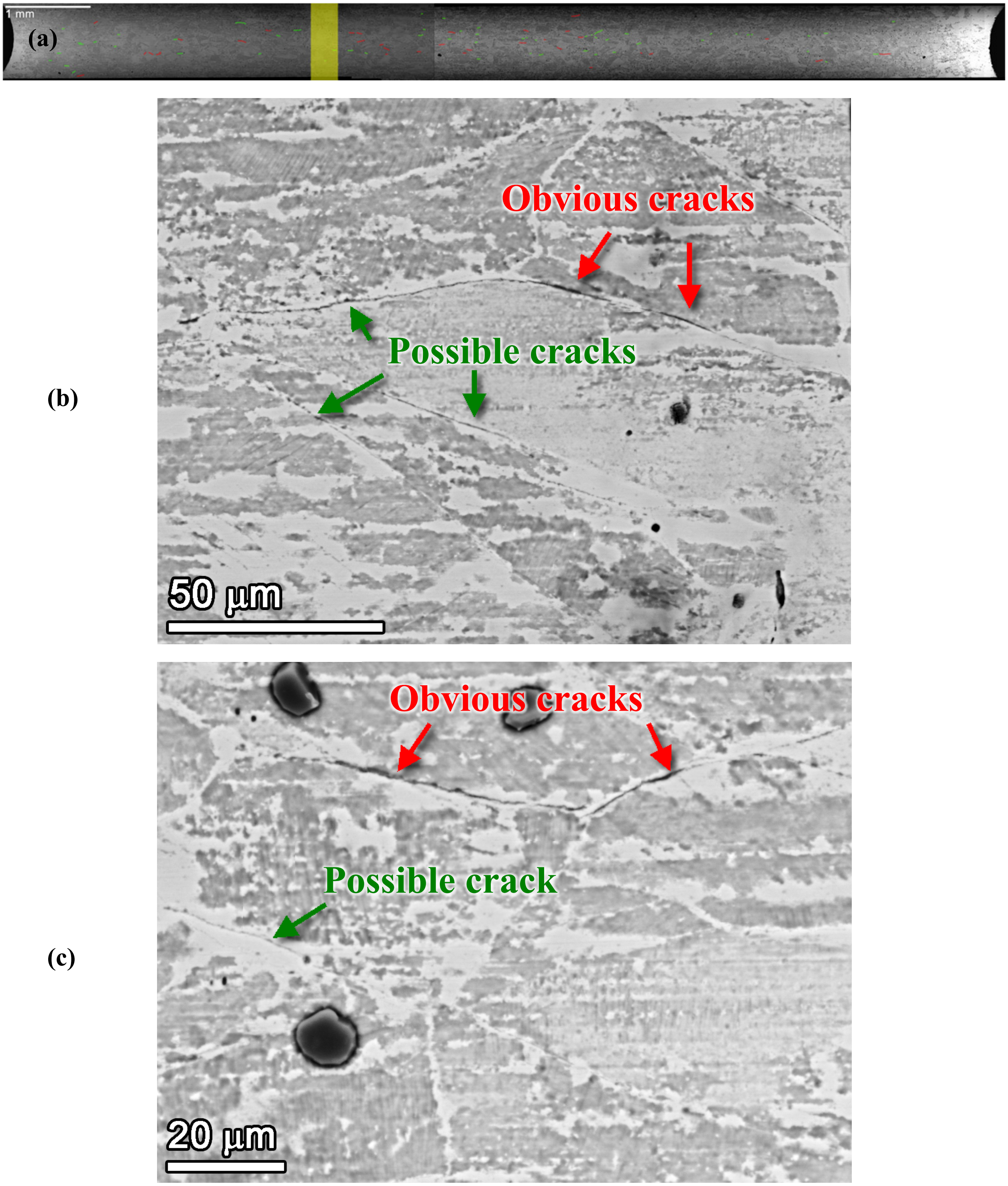

Figure 75. SEM-BSE characterizations of blunt notch specimen c703 (31%CF Valinox CRDM) surface (a) montage of the entire notch with red highlights for definite cracks and green highlights for possible cracks and (b/c) higher magnification examples of cracks detected.

The EDM sectioning and polishing approach to investigate crack morphologies is illustrated for specimen c703 in Figures 76-79. An area of the surface containing cracks along what appears to be incoherent twin boundaries is shown in Figure 76 along with cross-section locations examined after the 1st and 2nd polishing sequences. These locations intersect the twin boundaries (A and B) and a grain boundary (C). The subsurface features in the 1st polish location are presented in Figure 77(a) where an approximately 70 µm long crack is present at the twin boundary location A1. The crack starts at ~20 µm below the surface for the cross-section, but exhibits significant corrosion/oxidation along the crack walls and must be an SCC crack connected to the notch surface. This can be better resolved in Figure 77(b) at higher magnification for the twin boundary crack along with a series of cavities along the adjacent high-energy grain boundary. The IG cavities are thought to have occurred during one or more of the strain ramps. At the 2nd polish location, the SCC crack can be seen to extend to the surface confirming water ingress into the crack causing the observed crack wall corrosion structures. More detailed SEM examinations revealed evidence for cavities associated with the SCC crack. In addition, a series of creep cavities are present ahead of the corroded SCC crack tip. Small creep cracks are also identified across the notch on c703 as shown in Figures 81 and 81. Similar to c672, most of the creep cracks are located at a distance >100 µm below the surface.

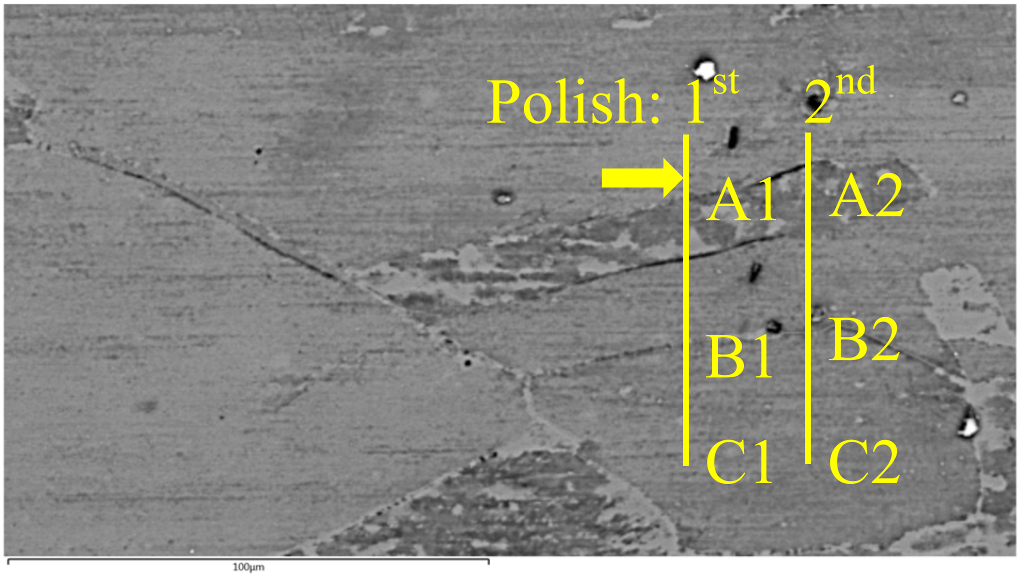

Figure 76. Blunt notch surface region showing cracks that the cross-section specimen intersected at two polishing depths.

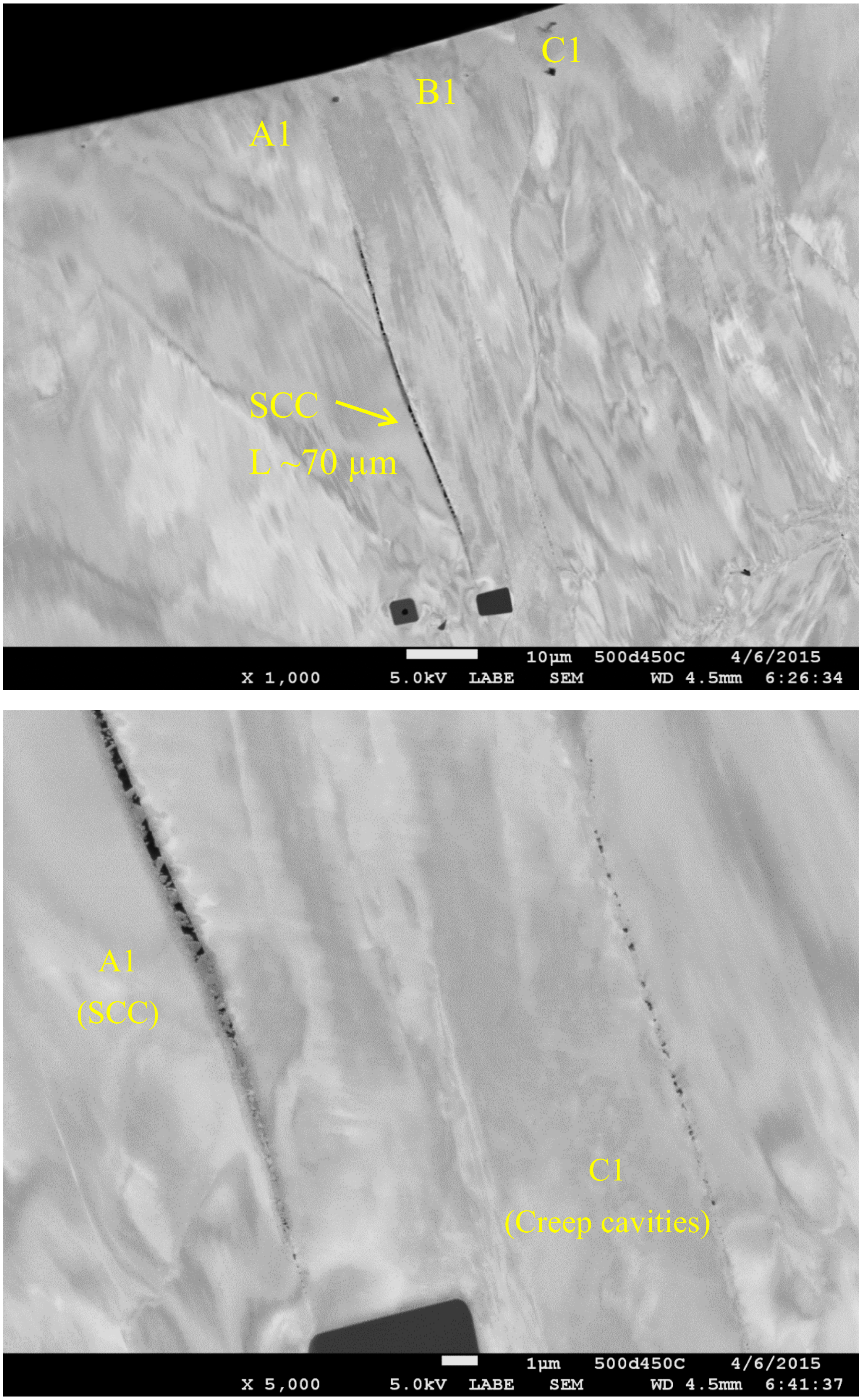

Figure 77. Subsurface SCC crack and grain boundary cavities below the surface shown in Figure 76 in 1st polish cross-section.

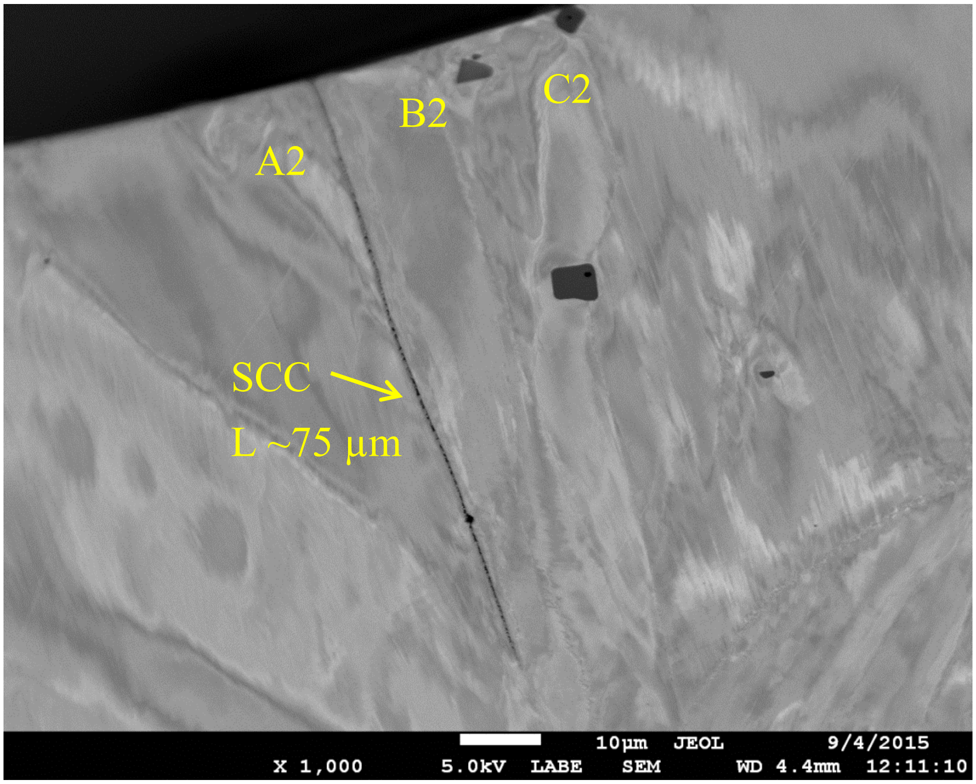

Figure 78. Subsurface SCC crack and grain boundary cavities below the surface shown in Figure 76 in 2nd polish cross-section.

The 31%CF Sumitomo CRDM specimen c704 also exhibited small cracks on the blunt notch surface as illustrated in Figure 82. The density of these cracks was lower than for the 31%CF Valinox specimen c703 and most were difficult to confirm as definite cracks based on the surface examinations. Two polishing sequences and characterizations have been performed on c704 cross-sections with no conclusive observations of SCC cracks. However, grain boundary creep cracks have been detected as documented in Figures 83 and 84 with the density much higher than observed in c703 (Figures 80 and 81). Additional cross-section observations are underway to better map this damage in the 31%CF specimens.

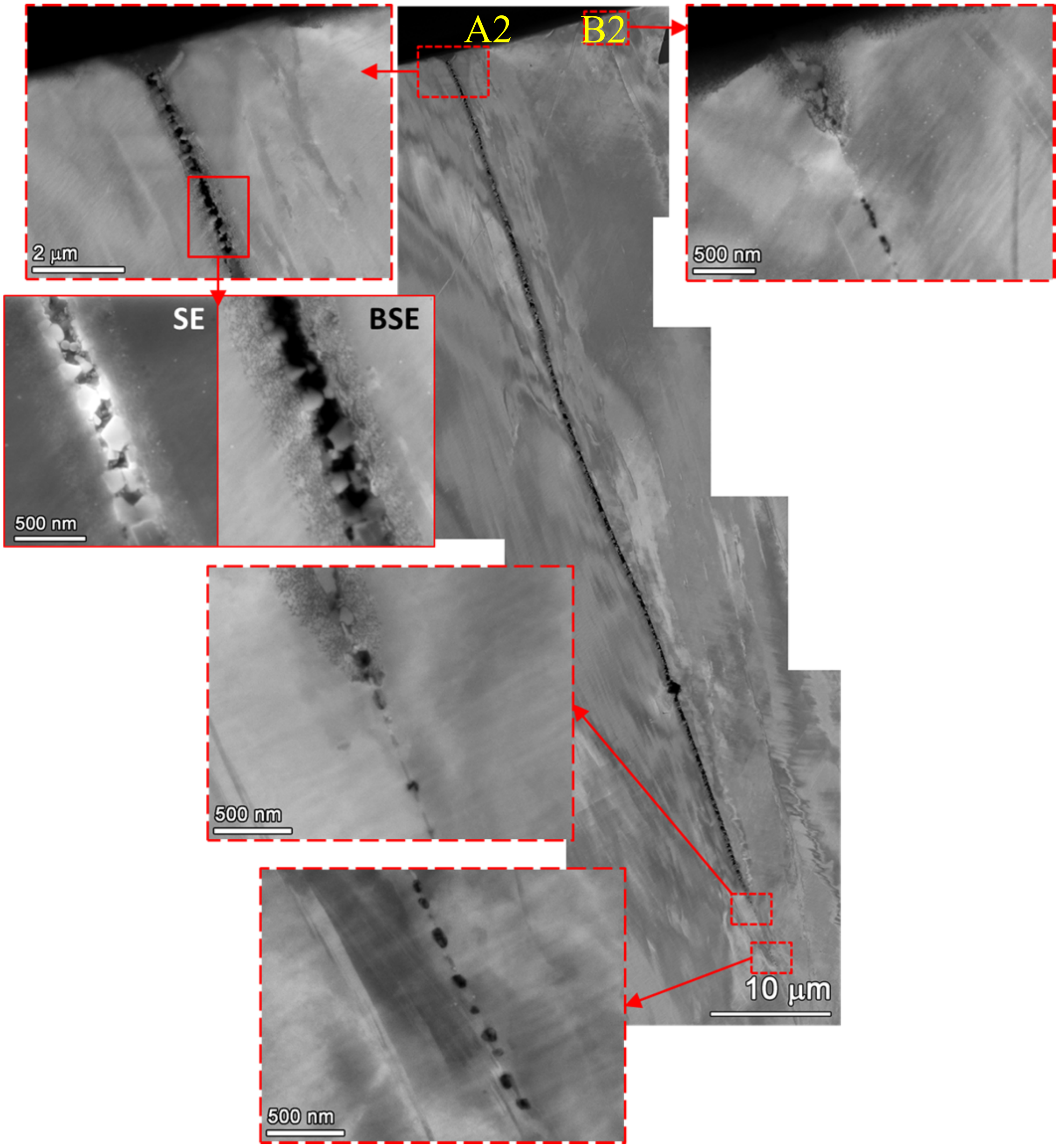

Figure 79. Detailed SEM examinations of the SCC crack in the 2nd polish cross-section. Evidence of creep cavities is seen near the surface and immediately ahead of the SCC crack.

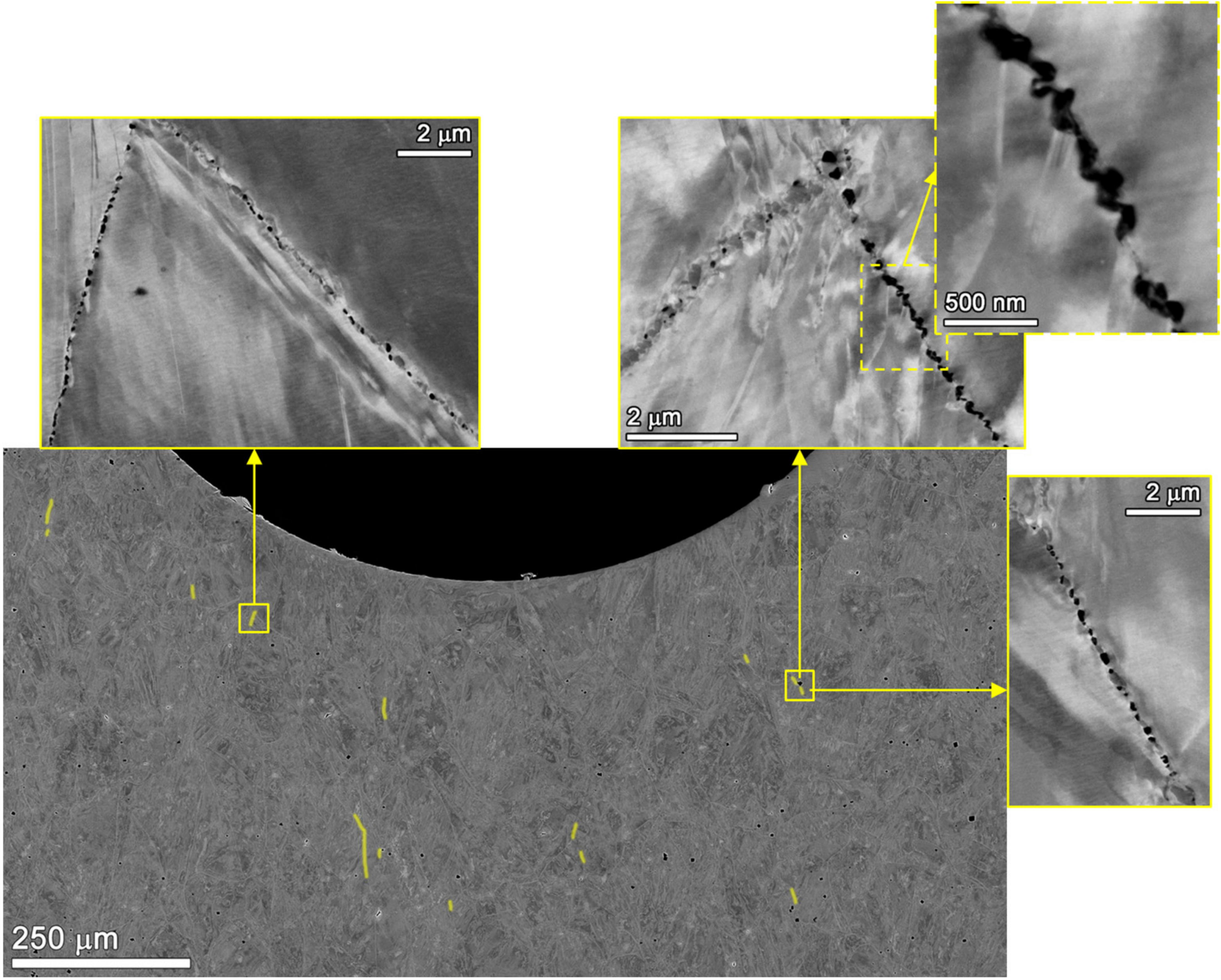
2 µm
2 µm
500 nm
2 µm
250 µm

Figure 80. SEM examinations revealing creep cracks in the cross-section of serial polish #1 for the c703 blunt notch specimen.

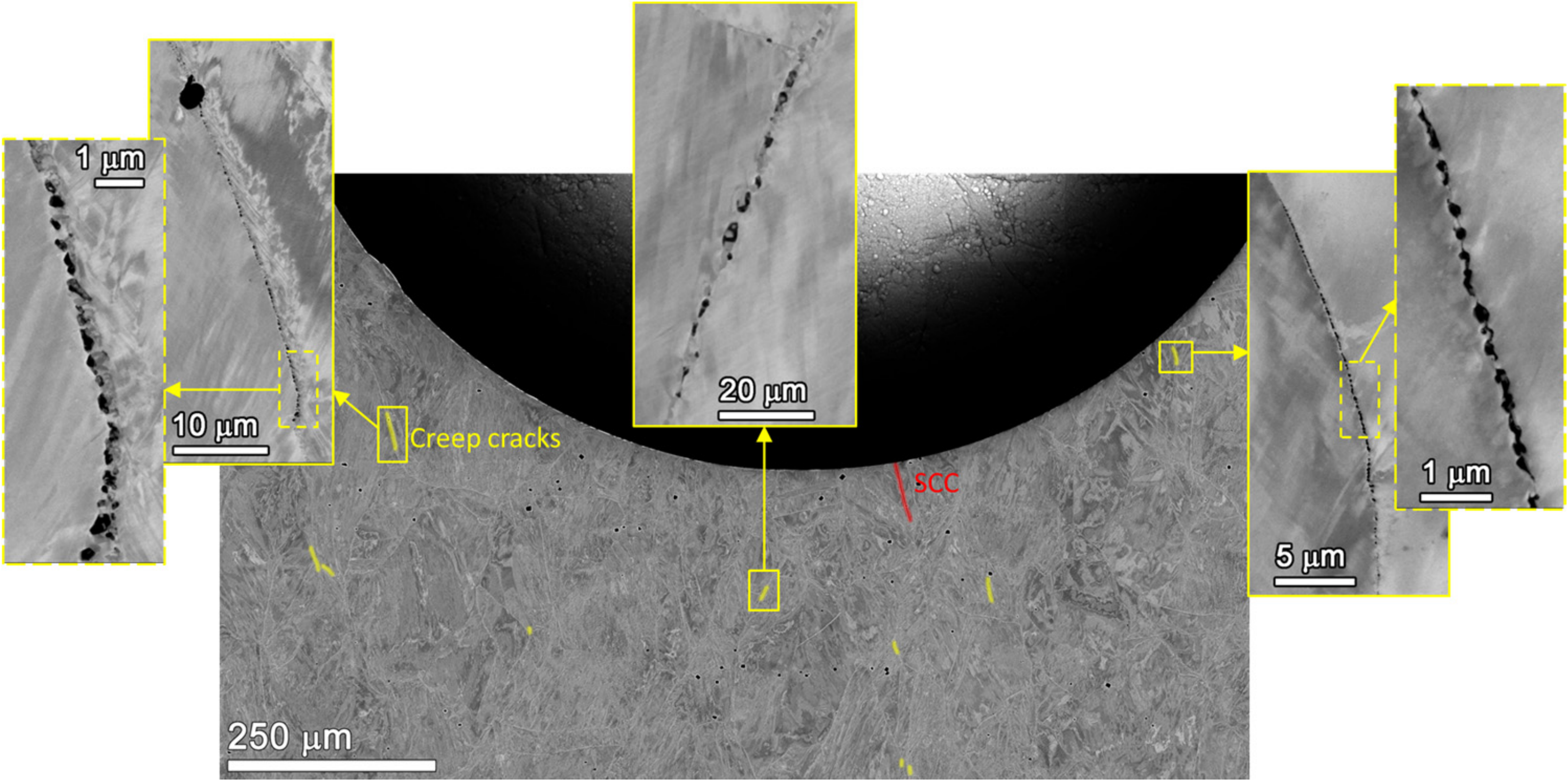

Figure 81. SEM examinations revealing creep cracks and creep cavities in the cross-section of serial polish #2 for the c703 blunt notch specimen. The lone SCC crack is the one shown in detail in Figures 78 and 79.

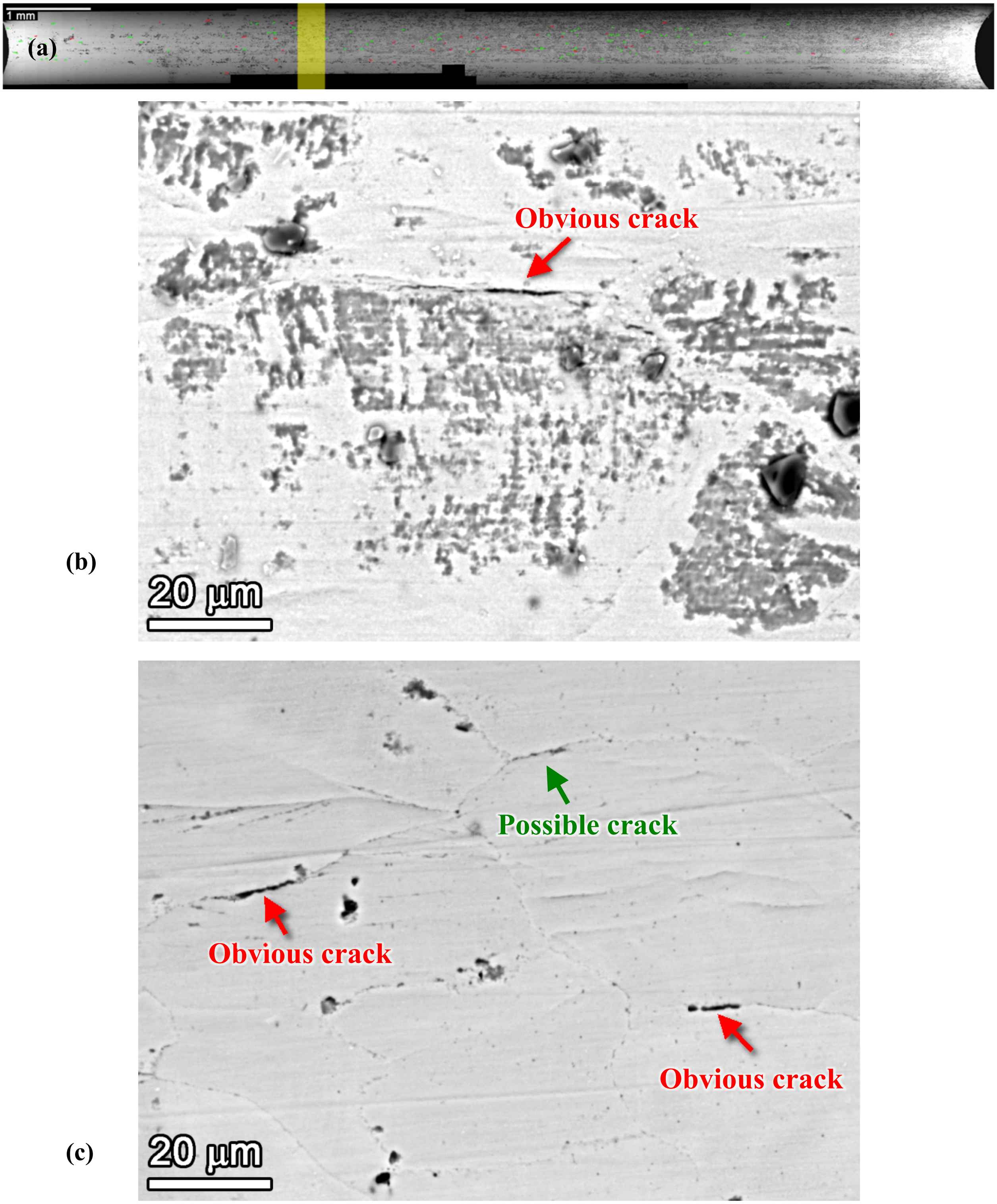

Figure 82. SEM-BSE characterizations of blunt notch specimen c704 (31%CF Sumitomo CRDM) surface (a) montage of the entire notch with red highlights for definite cracks and green highlights for possible cracks, and (b/c) higher magnification examples of cracks detected.

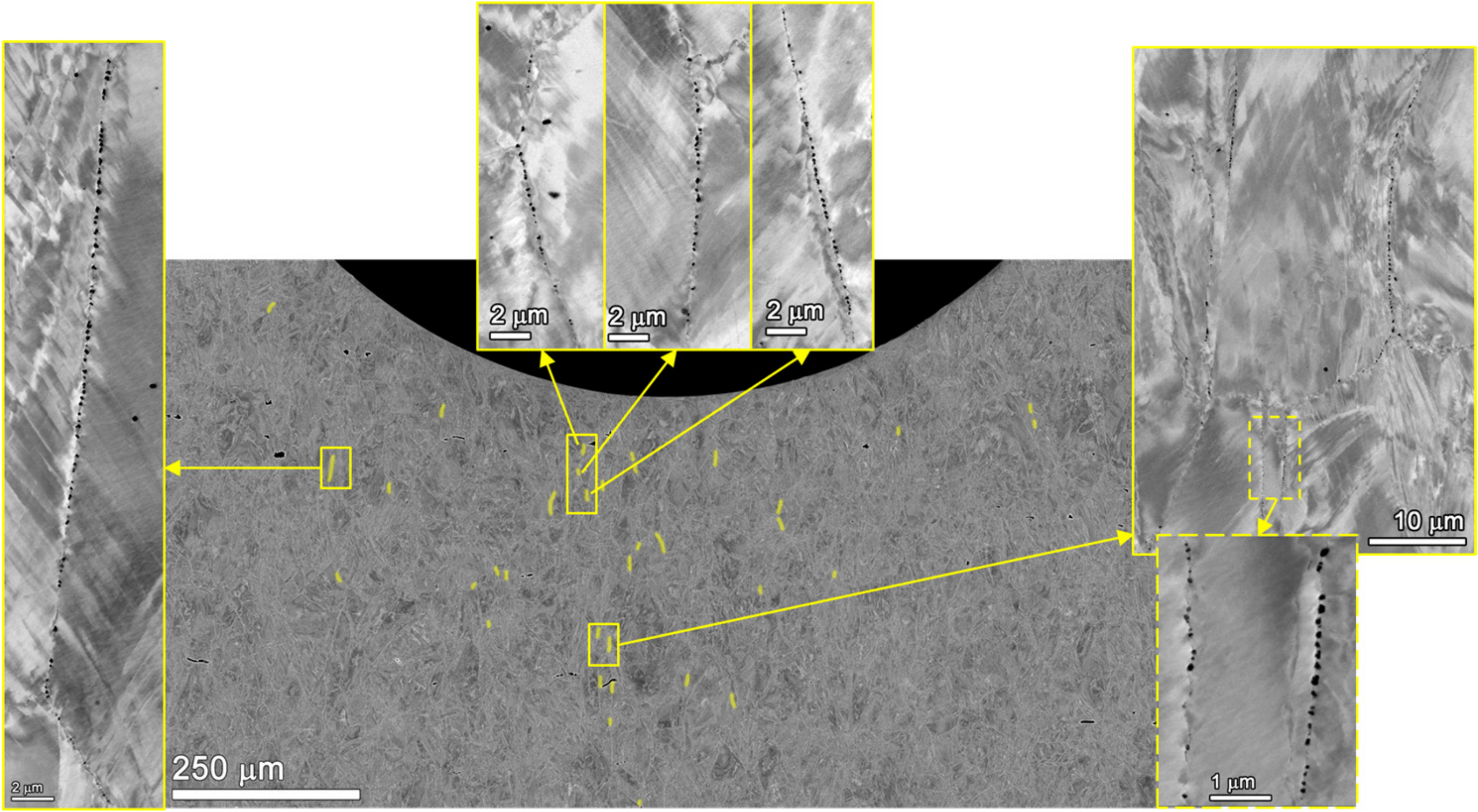

Figure 83. SEM examinations revealing creep cracks and creep cavities in the cross-section of serial polish #1 for the c704 blunt notch specimen.

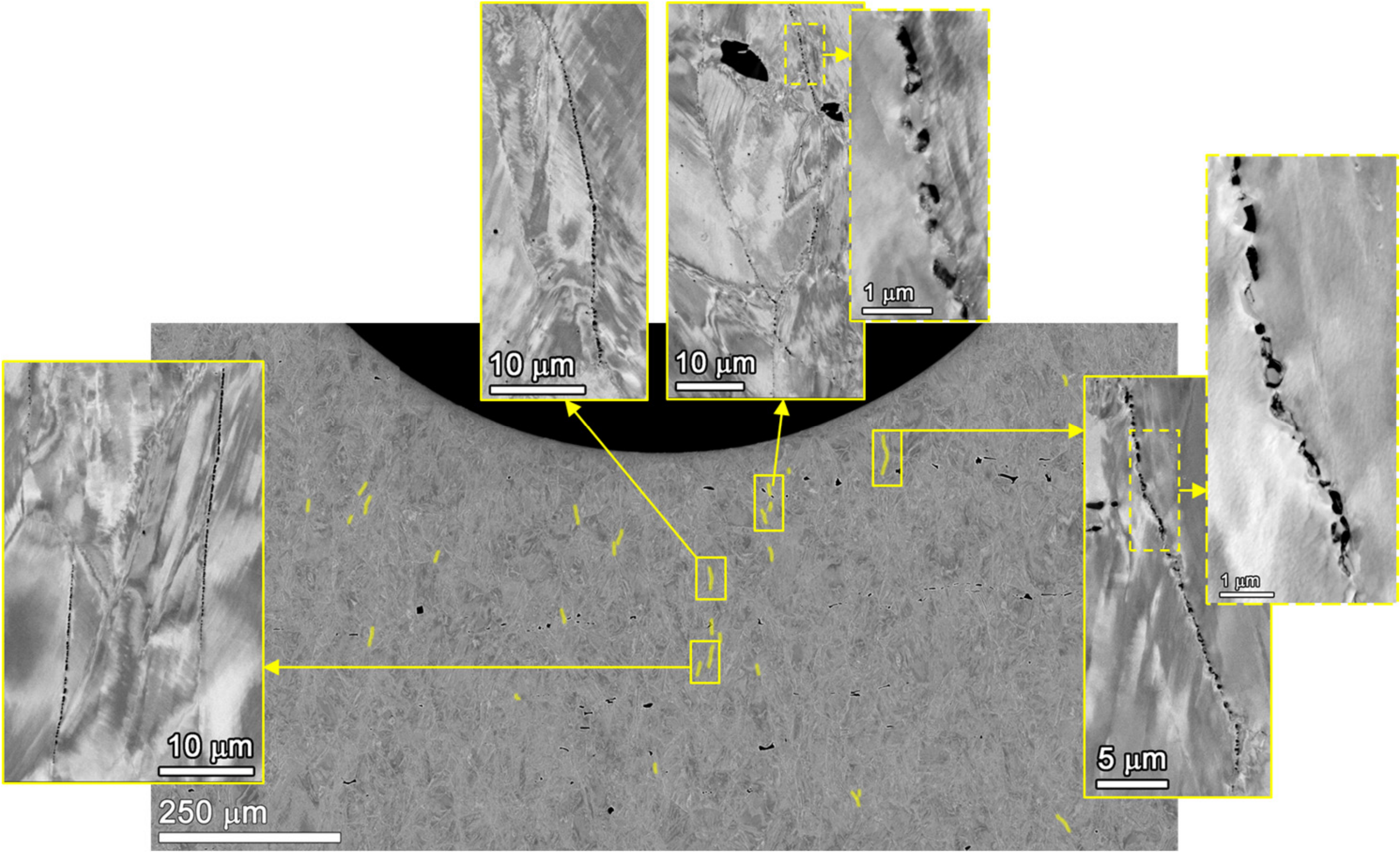

Figure 84. SEM examinations revealing creep cracks and creep cavities in the cross-section of serial polish #2 for the c704 blunt notch specimen.

The final two blunt notch test specimens were the 21%CF Valinox and Sumitomo CRDM specimens c707 and c708, respectively. Measured DCPD cracking response was summarized in Figure 74. As noted earlier, DCPD response revealed no indication of crack initiation and growth after 5542 hours, so the test was stopped for characterization of the specimens. Blunt notch surface examinations revealed a very low density of what appeared to be small cracks on the 21%CF c707 and c708 specimens by SEM-BSE imaging along with a few other features that were possible cracks. Montages of the blunt notch surfaces for the two specimens are presented in Figure 85 with obvious cracks highlighted in red and possible cracks highlighted in green. Even though surface damage was limited, the decision was made to section the 21%CF specimens c707 and c708 as done for the 31%CF specimens c703 and c704. The yellow bands shown on the two montages indicate the location where the specimen was sectioned to provide ~30% of the width for cross-section analyses and the other 70% to be used for further blunt notch SCC testing.

Initial cross-section characterizations have not revealed any significant depth to cracks targeted at the c707 and c708 surfaces. However, polish sequences have not yet intersected any definite surface cracks. The deepest crack encountered in either of the 21%CF specimens is presented in Figure 86 for the Valinox c707. While this is clearly an IG crack, its depth is only ~3 µm. In general, damage in the 21%CF specimens appears to be isolated at the surface. There is evidence for grain boundary cavities in both specimens, but their distribution and density suggests that they may be due to the cold forging (Figures 87 and 88). It seems that a few creep cracks were created during the loading ramps in c708 but none in c707. More detailed characterizations are continuing to better assess precursor damage structures in the 21%CF materials. Preliminary results suggest that the 21%CF materials are much more resistant to creep cavitation and crack nucleation as a result of the slow-strain-rate deformation than the 31%CF materials.

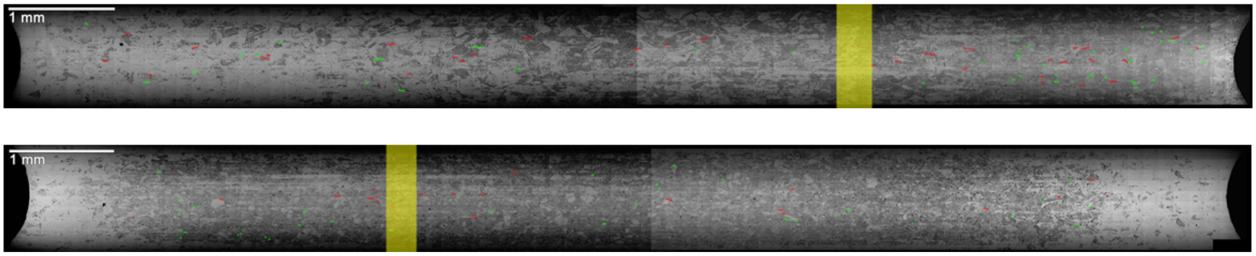

Figure 85. SEM-BSE image montages of entire blunt notch specimen surfaces: c707, 21%CF Valinox CRDM (above) and c708, 21%CF Sumitomo CRDM (below) with red highlights for definite cracks and green highlights for possible cracks.

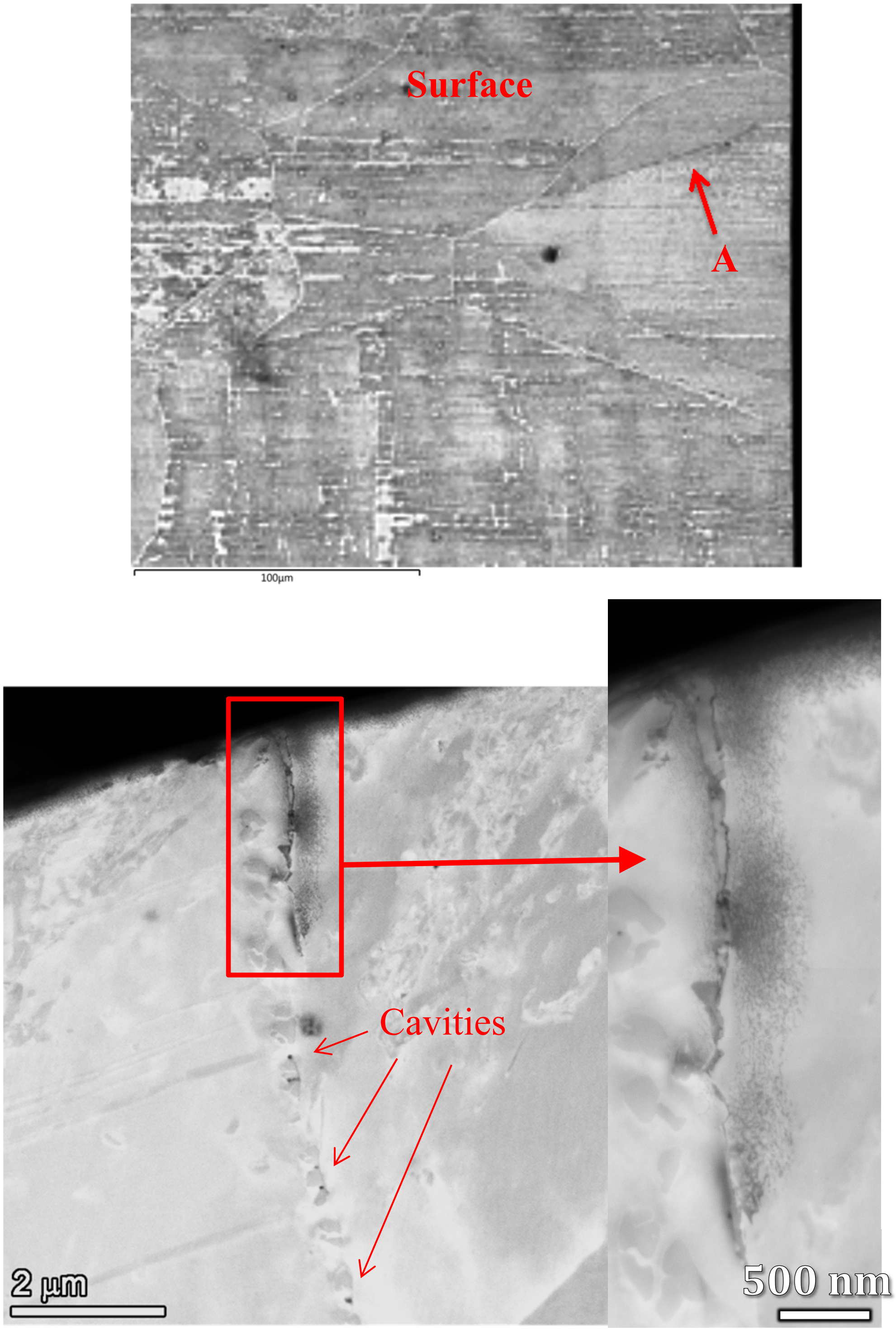

Figure 86. Example of crack analyses on the 21%CF Valinox CRDM specimen c707 specimen: (a) surface area with apparent crack where cross-section sample was obtained and (b) shallow IG crack to a depth of ~3 µm below the surface.

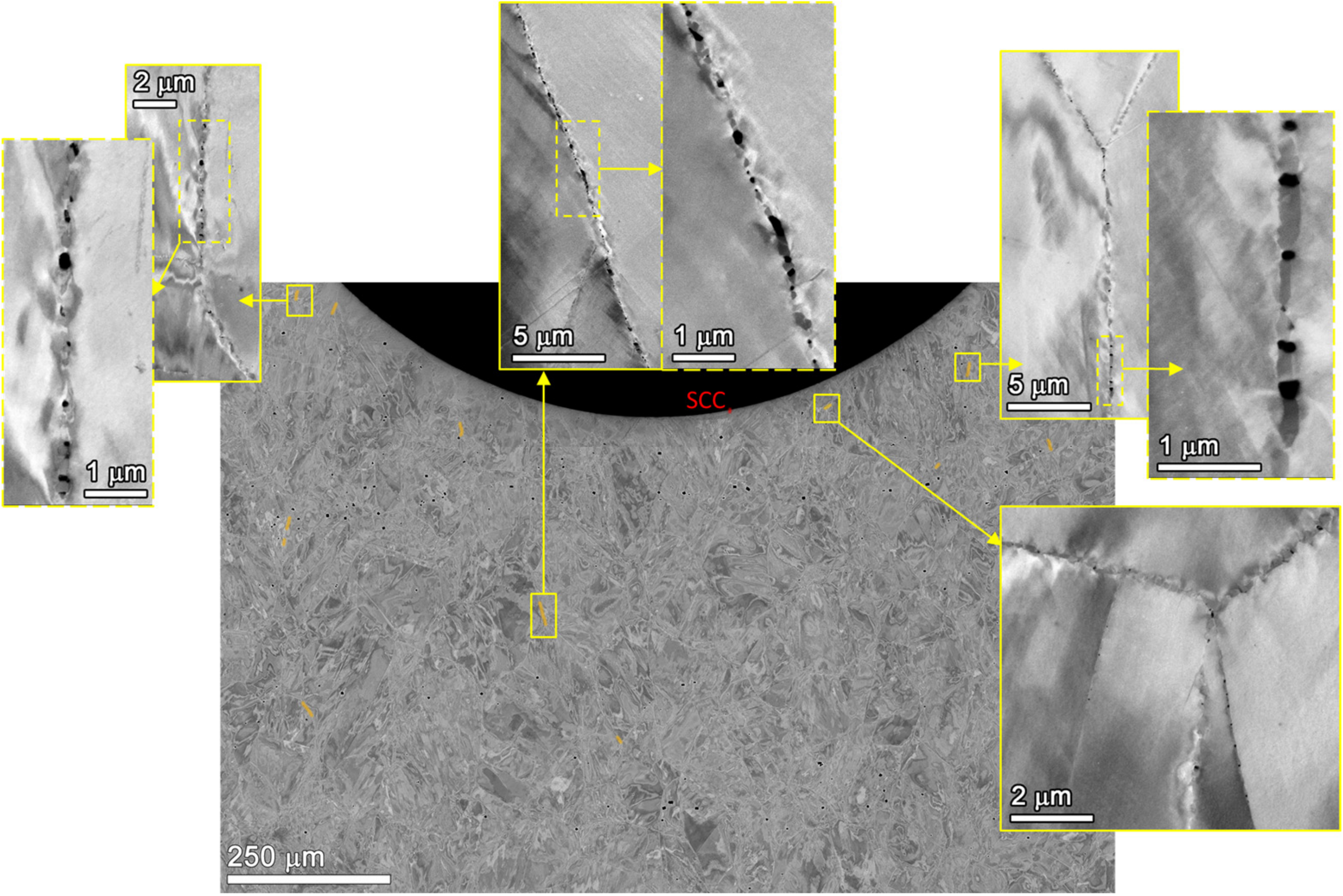

Figure 87. SEM examinations revealing groups of cavities formed during cold forging (in orange) in a cross-section for the c707 blunt notch specimen.

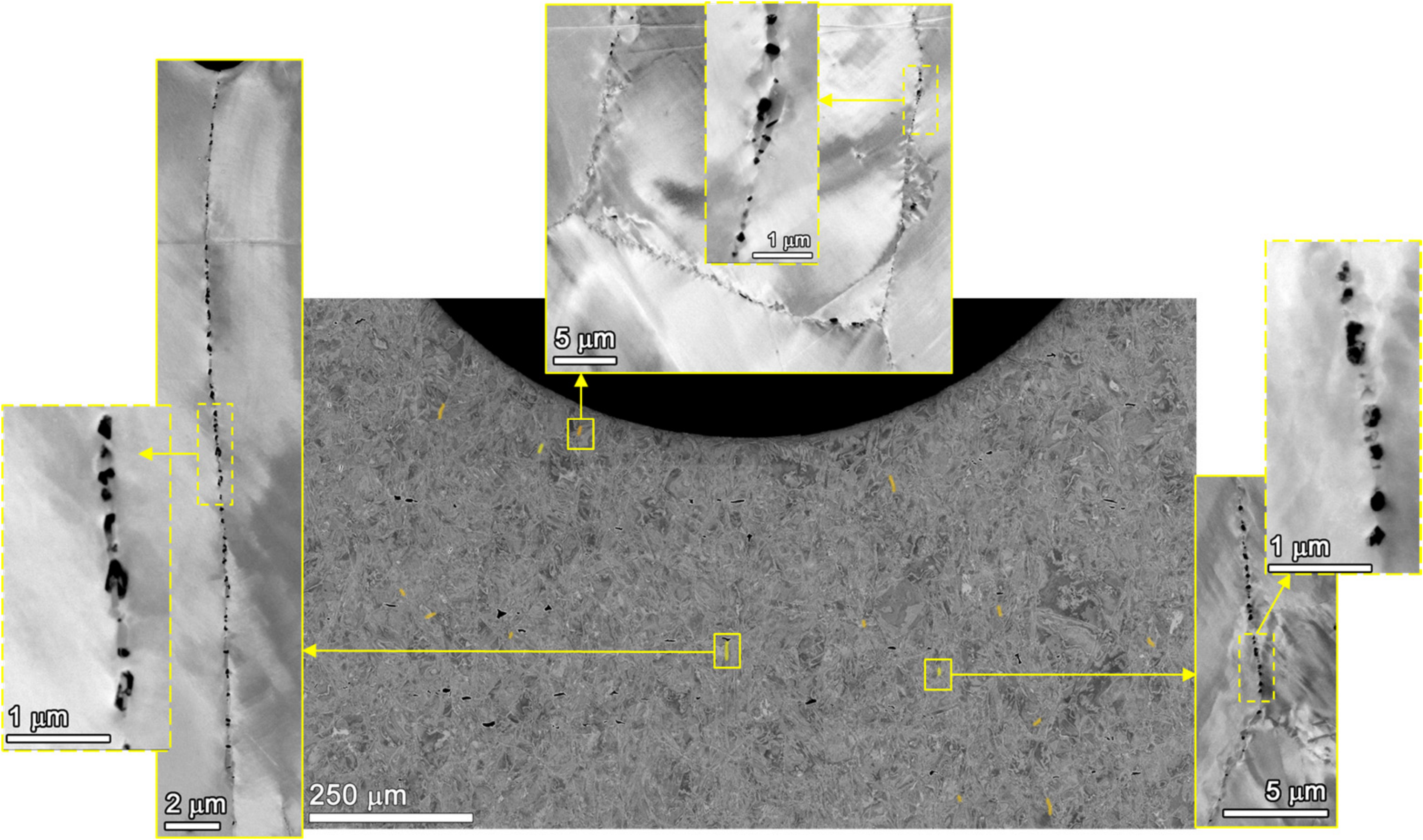

Figure 88. SEM examinations revealing groups of cavities formed during cold forging (in orange) and creep cracks (in yellow) in a cross-section for the c708 blunt notch specimen.

The 70% portions of all four blunt notch CT specimens were sent back to GEG and testing was resumed in 360°C PWR primary water at the same pseudo-K level of 36 MPa√m applied previously as documented in Figures 89 (31%CF) and 90 (21%CF). After ~3000 hours of exposure with no indication of SCC growth, the K level was increased by 1 MPa√m on all four specimens to attempt to determine whether any untracked SCC growth had occurred. A similar technique has been employed in SCC CGR tests to reveal evidence of untracked crack growth through the observation of a step change in crack length. However, no such change was observed for the blunt notch specimens, and these tests have now accumulated a total exposure approaching 9000 hours.

For the 21%CF specimens that appear to be free of any cracks deeper than ~5 µm, this lack of SCC growth is not surprising. However for the 31%CF specimens where surface cracks as deep as 200 µm have been observed, the lack of evolution into a growing SCC crack is somewhat surprising for the applied K level. One possibility for the lack of SCC growth is that the K of these relatively short but tight cracks off the blunt notch is not adequately represented by a standard K calculation. Thus, FEM is also underway again to assess what stress intensities may exist at the tips of these relatively short but tight cracks. The 31% CF specimens have recently been removed from testing again and will be reexamined at PNNL to assess whether any further crack extension has occurred. These observations will be covered in a future report.

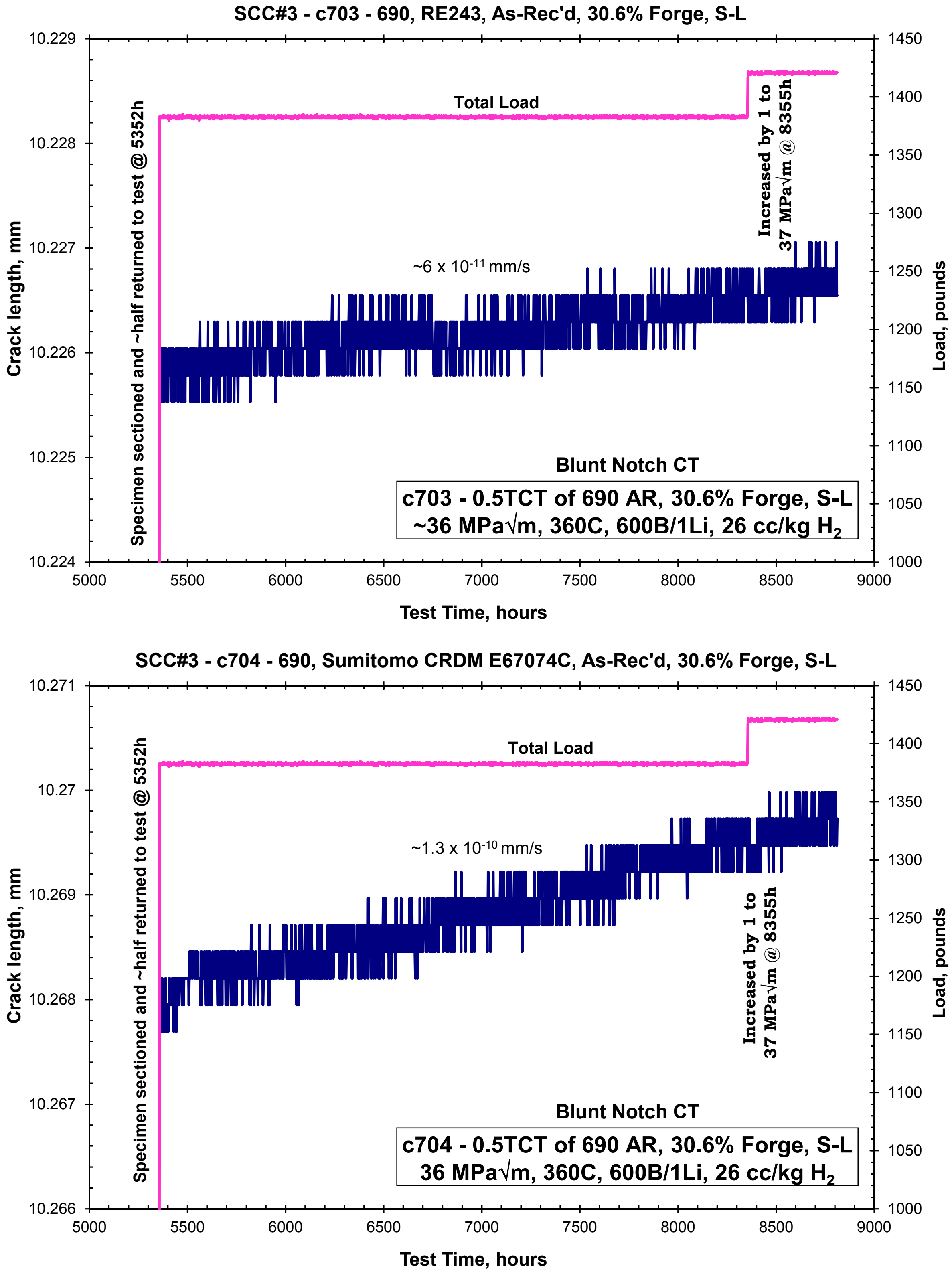

Figure 89. Constant K crack length versus time response for the 31%CF Valinox CRDM (c703) and 31%CF Sumitomo CRDM (c704) blunt notch specimens.

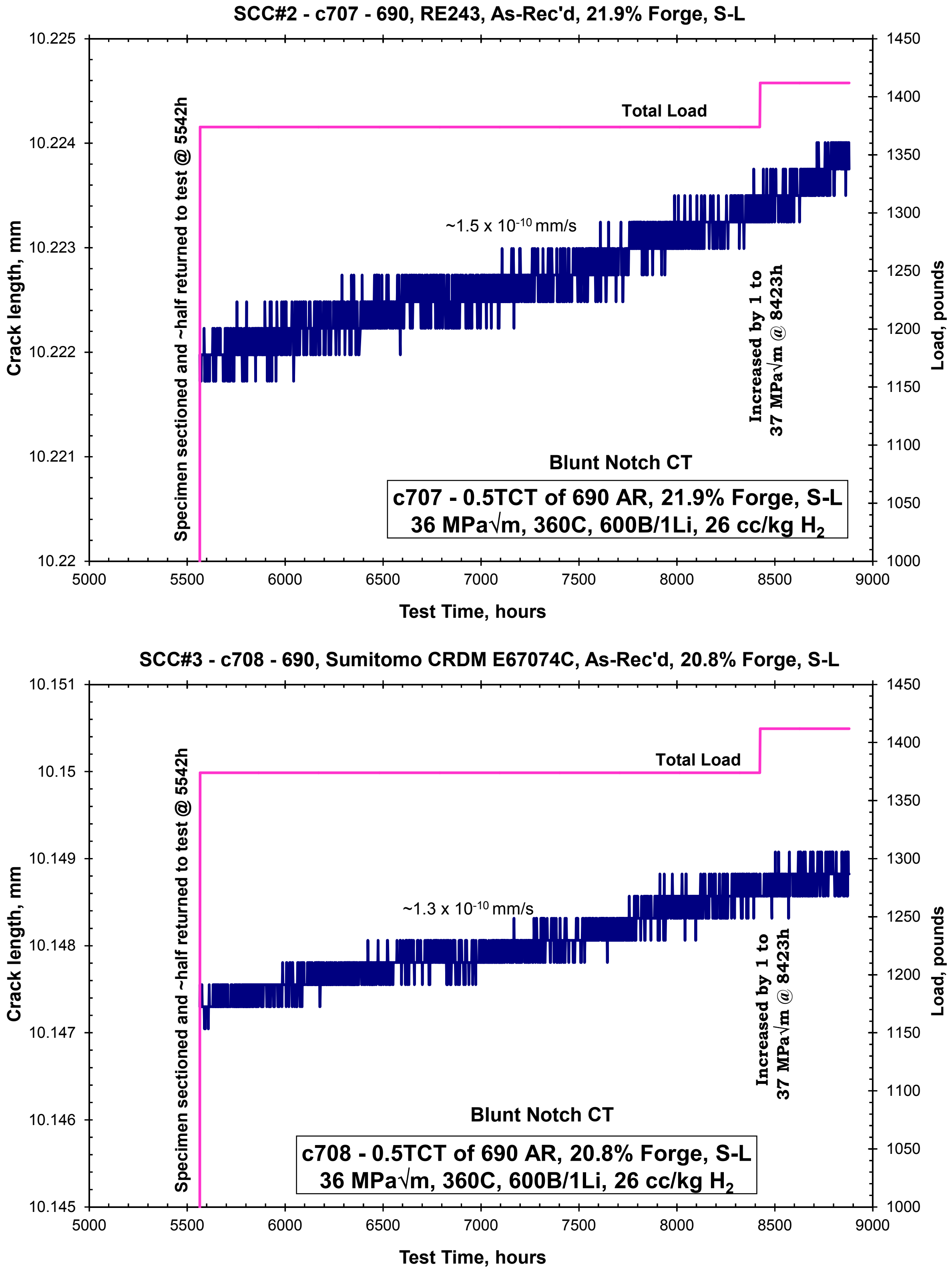

Figure 90. Constant K crack length versus time response for the 21%CF Valinox CRDM (c707) and 22%CF Sumitomo CRDM (c708) blunt notch specimens.

Constant Load Tensile Tests on Cold Forged Alloy 690 CRDM and Plate Materials

While alloy 690 exhibits excellent resistance to IGA (with or without stress) because of the highly protective Cr_2O_3 film that forms over grain boundaries intersecting the surface, the long term viability of this protective film and initiation resistance of alloy 690 should still be assessed. The protective film has been shown to be stable out to ~9000 hours (1 year) on two specimens (IN006/07) that were tested under aggressive conditions that included plastic straining. However, there are still unknown aspects of the long term microstructural evolution of alloy 690, one example being the unknown microstructural evolution that is causing the resistivity of this material to increase over time when exposed at 360°C. Long-term creep deformation may also affect the film stability or may enable crack precursor formation not related to comprising the protective surface film. To enable the task of performing long-term observations, a 36-specimen actively loaded and actively monitored test system was built and testing has been ongoing for more than 12 months. The validation of this test system design has benefited the NRC and industry justifying a jointly funded project to assess SCC initiation resistance of alloy 690/152/52 relative to alloy 600/182.

Testing first began on 21 alloy 690 specimens summarized in Table 9. These include four heats in a 31%CF condition and three heats in a 21%CF condition. Three heats - Sumitomo E67074C, Valinox RE243, and TK-VDM (Doosan) 133454 are CRDM materials, and one heat - TK-VDM 114092 is in the form of plate material. There are three specimens for each combination of heat and cold forge condition, and within each set of three, one has been polished to a 1 µm surface condition, and the other two have a ground "C" finish on the gauge section that was discussed previously. All specimens are being exposed at their yield stress. After ~2100 hours of operation, 15 additional CW alloy 690 specimens were inserted. These new alloy 690 specimens included the ANL (Special Metals) plate heat NX3297HK-12 of alloy 690 in a 26%CR condition, the GEG (Allvac) plate heat B25K in an 18%CF condition, the TK-VDM 114092 plate in a 21%CF condition, the Valinox CRDM heat RE243 in a 12%CF condition, and the GEG plate heat again in a 12%CF condition. Both the ANL and GE plate heats were previously observed to be very susceptible to SCC crack growth at the cold work levels used here. Summary information on the 15 additional alloy 690 specimens is given in Table 10. Testing was restarted with all 36 specimens again reloaded to their yield stress.

Table 9. Summary of Materials and Applied Stress (Yield Stress) for the First Group of Alloy 690 Specimens in the 36-specimen Test System

Specimen	Material	Material Condition	Surface Condition	Applied Stress, MPa
IN024 (CL)	Sumitomo CRDM	TT + 21%CF	1 µm Polish	575
IN025 (CL)	Sumitomo CRDM	TT + 21%CF	Ground C Finish	575
IN026 (CL)	Sumitomo CRDM	TT + 21%CF	Ground C Finish	575
IN027 (CL)	Valinox CRDM	TT + 21%CF	1 µm Polish	510
IN028 (CL)	Valinox CRDM	TT + 21%CF	Ground C Finish	510
IN029 (CL)	Valinox CRDM	TT + 21%CF	Ground C Finish	510
IN030 (CL)	Doosan CRDM	TT + 21.6%CF	1 µm Polish	540
IN031 (CL)	Doosan CRDM	TT + 21.6%CF	Ground C Finish	540
IN032 (CL)	Doosan CRDM	TT + 21.6%CF	Ground C Finish	540
IN033 (CL)	Sumitomo CRDM	TT + 31%CF	1 µm Polish	690
IN034 (CL)	Sumitomo CRDM	TT + 31 %CF	Ground C Finish	690
IN035 (CL)	Sumitomo CRDM	TT + 31%CF	Ground C Finish	690
IN036 (CL)	Valinox CRDM	TT + 31%CF	1 µm Polish	700
IN037 (CL)	Valinox CRDM	TT + 31%CF	Ground C Finish	700
IN038 (CL)	Valinox CRDM	TT + 31%CF	Ground C Finish	700
IN039 (CL)	Doosan CRDM	TT + 31%CF	1 µm Polish	665
IN040 (CL)	Doosan CRDM	TT + 31%CF	Ground C Finish	665
IN041 (CL)	Doosan CRDM	TT + 31%CF	Ground C Finish	665
IN042 (CL)	TK-VDM Plate	TT + 31.9%CF	1 µm Polish	680
IN043 (CL)	TK-VDM Plate	TT + 31.9%CF	Ground C Finish	680
IN044 (CL)	TK-VDM Plate	TT + 31.9%CF	Ground C Finish	680

CL = constant load

Table 10. Summary of Materials and Applied Stress (Yield Stress) for the Second Group of Alloy 690 Specimens that were added to the 36-Specimen Test System

Specimen	Material	Material Condition	Surface Condition	Applied Stress, MPa
IN053 (CL)	ANL Flat Bar	MA + 26%CR	1 μm Polish	775
IN054 (CL)	ANL Flat Bar	MA + 26%CR	1 μm Polish	775
IN055 (CL)	ANL Flat Bar	MA + 26%CR	Ground C Finish	775
IN056 (CL)	GE B25K Bar	MA + 18.3%CF	1 μm Polish	550
IN057 (CL)	GE B25K Bar	MA + 18.3%CF	1 μm Polish	550
IN058 (CL)	GE B25K Bar	MA + 18.3%CF	Ground C Finish	550
IN059 (CL)	TK-VDM Plate	TT + 21%CR	1 μm Polish	690
IN060 (CL)	TK-VDM Plate	TT + 21%CR	1 μm Polish	690
IN061 (CL)	TK-VDM Plate	TT + 21%CR	Ground C Finish	690
IN062 (CL)	GE B25K Bar	MA + 12.4%CF	1 μm Polish	510
IN063 (CL)	GE B25K Bar	MA + 12.4%CF	1 μm Polish	510
IN064 (CL)	GE B25K Bar	MA + 12.4%CF	Ground C Finish	510
IN065 (CL)	Valinox CRDM	TT + 11.7%CF	1 μm Polish	365
IN066 (CL)	Valinox CRDM	TT + 11.7%CF	1 μm Polish	365
IN067 (CL)	Valinox CRDM	TT + 11.7%CF	Ground C Finish	365

CL = constant load

DCPD-based strain response for 11 out of the 12 instrumented specimens for the most recent 3500 hours of testing is presented in Figures 91-94. Some portions of the specimen response have been omitted due to building outages that required temporarily reducing operating temperature and sometimes load. DCPD measurements for the one instrumented 31%CF specimens not shown here has been exhibiting a strong sensitivity to changes in water chemistry indicating a short circuit in the DCPD wiring. The response of the 11 specimens are all quite similar with indicated strain increases of 0.1-0.5%. The variation in strain does not consistently scale with cold work level or applied stress suggesting that much of this indicated strain may be due to ongoing material resistivity evolution that is not removed from these measurements. The trend towards a continually decreasing strain rate is also another indicator that much of the indicated strain is due to resistivity evolution. Testing of these specimens was just recently interrupted to perform detailed surface observations of the gauge sections of all the polished specimens and to perform length change measurements to attempt to quantify any possible creep strain. These observations will be covered in a future report.

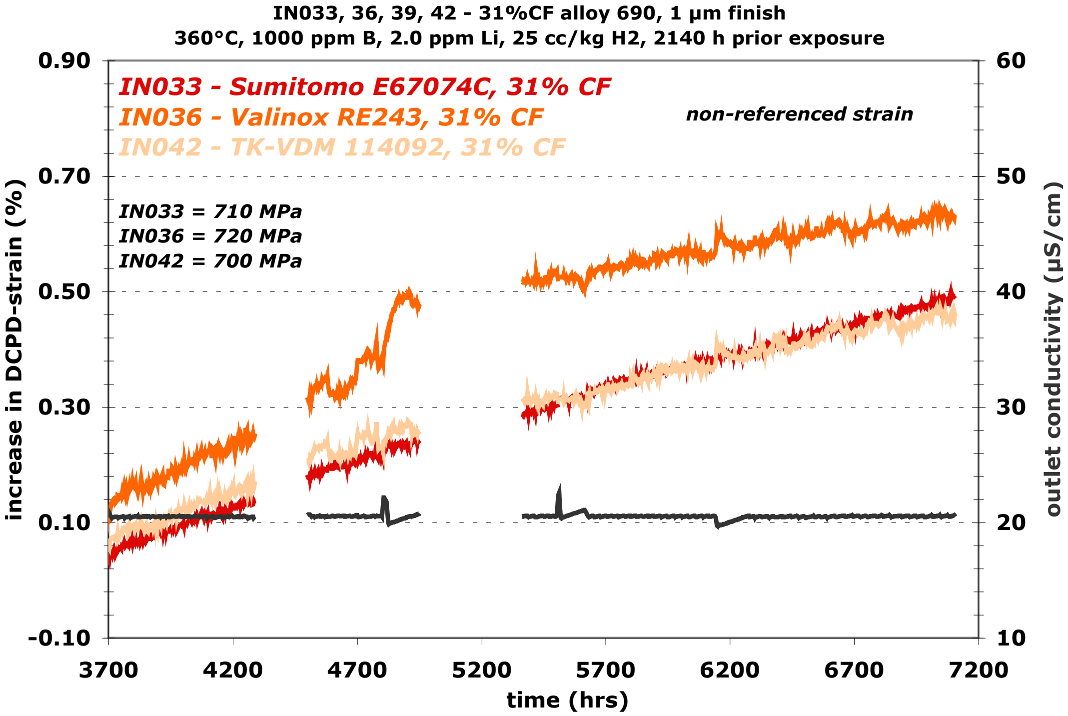

Figure 91. Non-referenced strain response for three heats of 31%CF alloy 690 undergoing long term constant load exposure at 360°C in the PNNL 36-specimen initiation test system. For each heat of material at this CW level, there are 3 specimens in the test rig.

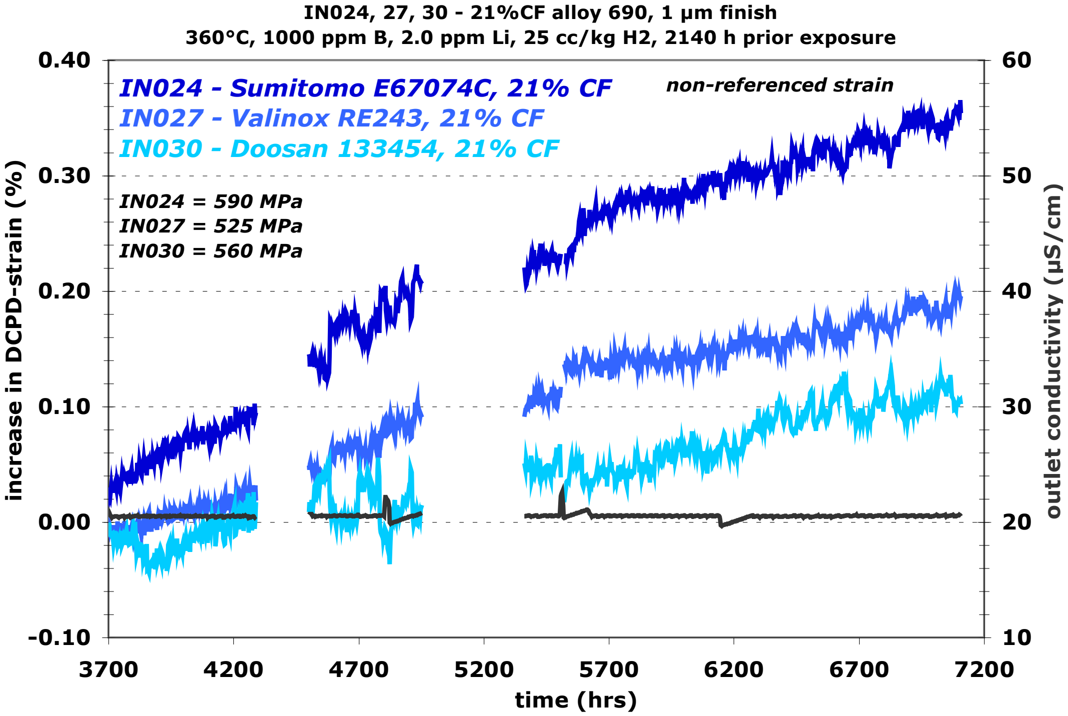

Figure 92. Non-referenced strain response for three heats of 21%CF alloy 690 undergoing long term constant load exposure at 360°C in the PNNL 36-specimen initiation test system. For each heat of material at this CW level, there are 3 specimens in the test rig.

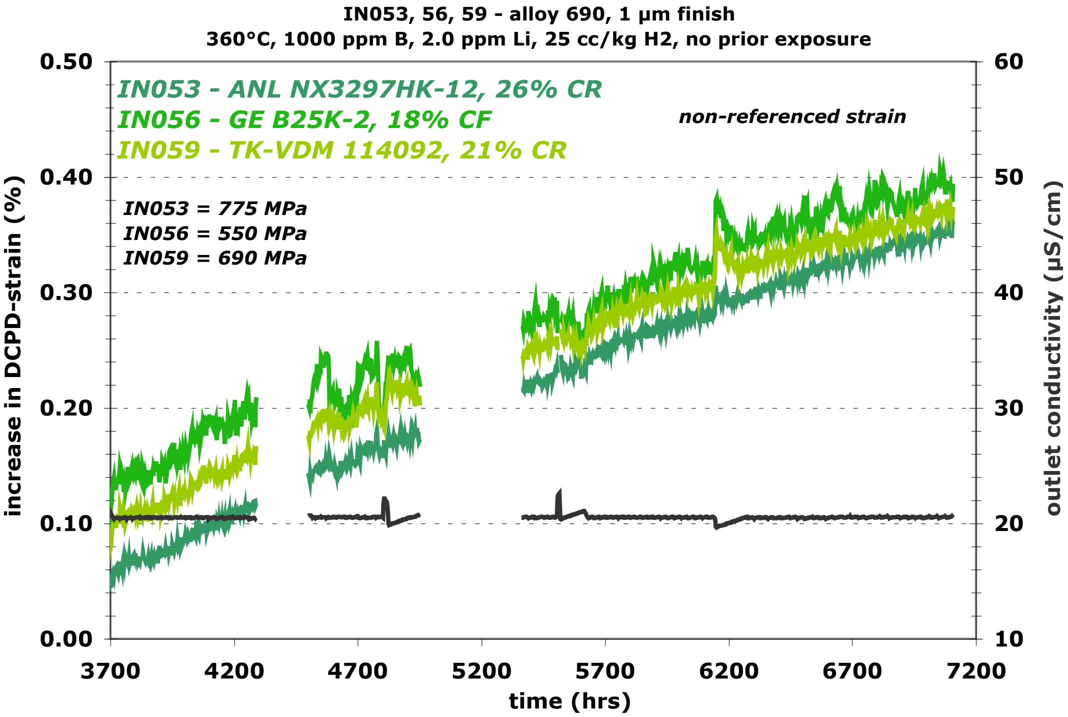

Figure 93. Non-referenced strain response for three heats of 18-26%CW alloy 690 undergoing long term constant load exposure at 360°C in the PNNL 36-specimen initiation test system. For each heat of material at this CW level, there are 3 specimens in the test rig.

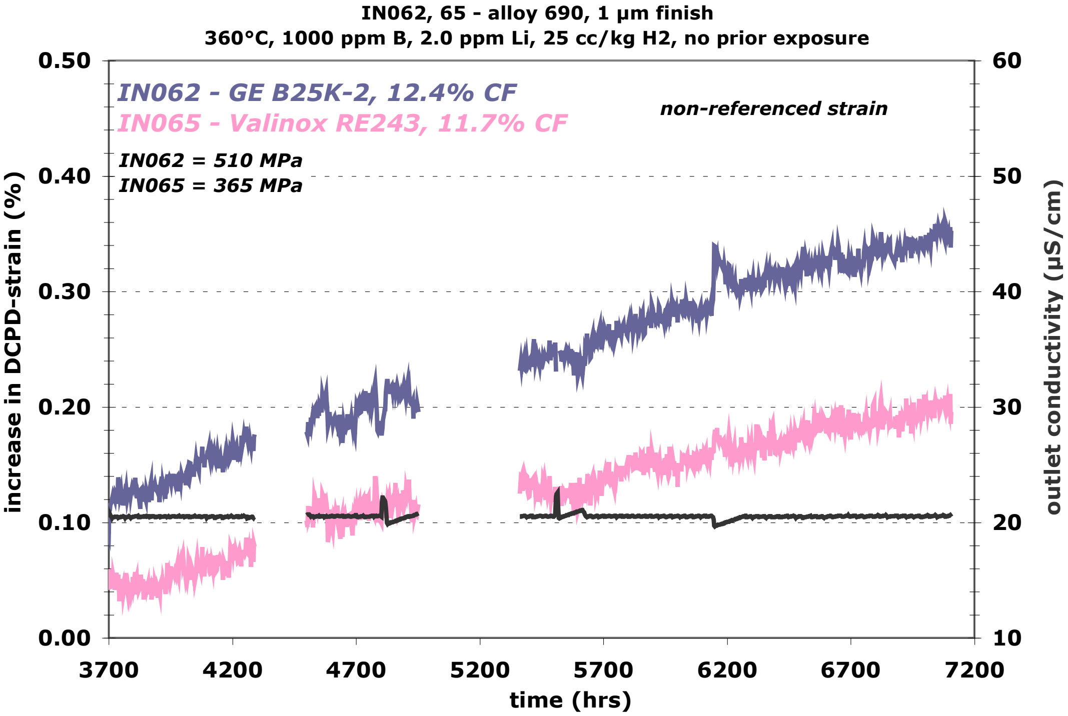

Figure 94. Non-referenced strain response for two heats of 12%CF alloy 690 undergoing long term constant load exposure at 360°C in the PNNL 36-specimen initiation test system. For each heat of material at this CW level, there are 3 specimens in the test rig.

Discussion of Alloy 690 SCC Initiation Results

The approach for SCC initiation testing was established by our experiments on CW alloy 600 (described earlier in this report) where crack nucleation was successfully detected in less than 2500 hours. Even though it is clear that the mechanisms controlling corrosion and SCC are different for alloy 600 and alloy 690 in PWR primary water, CW alloy 690 has been shown by many investigators to be highly susceptible to SCC crack growth. Moreover, SCC propagation rates comparable to those for MA alloy 600 have been measured for highly CW alloy 690 materials. This similarity in SCC propagation rates led to an expectation that highly CW alloy 690 may also be susceptible to SCC initiation in constant load tests.

The first phase of the SCC initiation test plan for alloy 690 was built around this hypothesis and utilized materials that exhibit high primary water SCC propagation rates (~$1x10^{-7}$ mm/s) when in a CW condition. SCC susceptible 26-31%CR materials (IN006/IN007) were selected to critically evaluate this assumption using tensile specimens and begin investigations of key factors influencing SCC initiation in alloy 690. The lack of SCC initiation in these specimens after long exposures in 360°C simulated PWR primary water at high stresses modified expectations. While the total test time for these early CR alloy 690 tests were only 2-3x higher than the measured SCC initiation times for CW alloy 600, surface characterizations on both stressed and unstressed alloy 690 revealed important differences in oxidation microstructures. A continuous chromia film forms above alloy 690 grain boundaries and effectively blocks IGA that acts as a precursor to SCC initiation in alloy 600. Results for the first constant load tests on SCC-susceptible alloy 690 specimens indicate that this protective chromia film is not broken down even after long exposures at the yield stress. Therefore, modifications to the testing approach were made to determine whether precursor cracks could be generated by other means. The most obvious method, which is the one currently being applied for this work, is dynamic straining.

Several different straining methods were explored in these early SCC initiation experiments. For the highly CR materials known to be susceptible to SCC growth, it was decided to periodically induce small amounts of in-situ tensile deformation at a moderate strain rate of ~$5x10^{-4}$ s^{-1}. The intent was to create surface damage and compromise the protective film leading to formation of SCC precursors. Most of this evaluation focused on the 26%CR ANL plate specimen IN006 when micrometer-length cracks were observed to nucleate off corroded TiN stringers that intersected the surface. Increasing plastic strain was found to increase the density and size of IG and TG cracks. However despite several applications of plastic strain and almost 4000 hours of additional exposure at very high stress, these cracks did not exceed ~10 µm in depth showing that alloy 690 is remarkably resistant to additional growth under these aggressive conditions.

For another series of specimens that were cold tensile strained prior to SCC initiation testing, the effect of cyclic loading and slow strain rate extension were both assessed. While it was understood that cyclic loading up to yield stress would produce only elastic strains, it was hoped that the strains would be sufficiently large to disrupt the surface oxide film. Although testing conditions were limited, no change in specimen response was observed during cyclic loading. The same specimens were then subjected to slow strain rate testing to 2.5-4.5% plastic strain over a period of eight days (strain rate of ~$1\text{x}10^{-7}$ s^{-1}). This produced a high density of slip bands intersecting the surface with many having the appearance of cracks with lengths up to ~10 µm. These results are consistent with the slow strain rate testing of alloy 690 in 360°C PWR primary water by Moss [35]. Surface cracks of a similar depth (average ~3 µm) were reported indicating that continuous dynamic strain can clearly lead to crack formation in alloy 690.

This assessment of slow strain rate effects was continued on initiation specimens and blunt notch specimens. When IN007 (31%CF Valinox RE243) was subjected to an order of magnitude slower strain rate (~$1\text{x}10^{-8}$ s^{-1}) than previous slow strain rate observations, IG creep cavitation and SCC initiation was observed to take place. Concurrent blunt notch tests on highly CW alloy 690 where slow loading ramps were applied to produce surface strain rates of ~$1\text{x}10^{-8}$ s^{-1} also resulted in the formation of creep cavitation and SCC initiation. While these tests established a means to produce SCC initiation, the specific details by which it occurred have not been determined. The most recent blunt notch tests have shown IG creep cavitation reaching the surface and leading to the nucleation of an SCC crack. It remains unclear whether grain boundary creep cavity formation is the primary cause of IG crack nucleation at the surface or whether both creep and SCC cracks nucleate simultaneously and through percolation processes, eventually link up. Attempts to answer this question are the focus of ongoing blunt notch and constant load tests on CW alloy 690.

These results clearly demonstrate that alloy 690 materials can exhibit quite different susceptibility to SCC initiation versus SCC growth. Highly CW alloy 690 that shows very high SCC propagation rates in tests on compact tension specimens have been remarkably resistant to SCC initiation in constant load tests on polished specimens. The parallel assessment of alloy 690 surface corrosion microstructures has shown that this material is resistant to IG corrosion-oxidation due to the formation of a protective chromia film above the grain boundaries that intersect the surface. As a result, SCC initiation from a smooth surface appears to be extremely difficult without aggressive straining to thin or break this protective oxide layer. It is interesting to note that strong Cr depletion is observed along grain boundaries to micrometer depths below the surface. Therefore if the protective layer is breached, IG corrosion and SCC of the Cr-depleted grain boundary might be expected.

An important conclusion from these early experiments is that dynamic plastic deformation appears to be required to nucleate cracks in alloy 690. Crack growth testing has also revealed limited CGRs at low K levels for highly CW alloy 690 heats even though high CGRs are measured at moderate stress intensities (20-30 MPa√m). Thus for SCC initiation to occur, it appears that dynamic straining is required to produce precursor cracks and enable crack growth to a sufficient depth and local K level enabling practical SCC initiation.

Summary and Conclusions

Current understanding for alloy 600 indicates that IG precursor flaws of sufficient size are needed to produce a critical local K for SCC growth and practical SCC initiation. The required precursor flaws are readily achieved in alloy 600 by stress-assisted IGA during constant load exposure followed by slow crack growth and crack coalescence. The progression to practical SCC initiation appears to be controlled by the SCC crack growth susceptibility of the alloy 600 material at low K levels. Experimentation to-date indicates that as-received alloy 600 is susceptible to SCC initiation in tests at constant equal to its yield strength. Nucleation of small surface microcracks is seen to occur rather quickly from IGA, but the transition to more macroscopic SCC initiation requires long exposure times. By comparison, CW alloy 600 transitions from micro-to-macroscopic SCC initiation rapidly due to its much greater susceptibility to SCC at low K levels. The effect of surface condition on SCC initiation has not yet been investigated in detail, but early observations suggest that a ground surface layer can delay SCC initiation slightly due to the formation of a Cr-rich surface layer that slows IGA. SCC initiation experiments on alloy 600 materials have also produced important advances in the in-situ measurement of crack nucleation. Although DCPD is not sensitive to the formation of small surface cracks, it can effectively identify the transition to practical SCC initiation. Research is continuing to quantify DCPD measurement capabilities with respect to crack length and depth.

SCC experimentation has revealed that CW alloy 690 is extremely resistant to SCC initiation even when highly susceptible to SCC growth. The first attempts to produce SCC initiation in constant load tests at high stress did not produce SCC. Detailed microstructural investigations of alloy 690 revealed that a protective chromia layer rapidly forms above grain boundaries in PWR primary water and this film appears to remain protective during constant load testing at high stresses. Efforts to accelerate the crack initiation process by application of tensile loading type plastic strain rates produced surface cracking, but no evidence of SCC initiation. Small surface precursor cracks formed during plastic straining remained in the micrometer size range and showed no evidence of growth. Application of plastic deformation at much slower strain rates promoted SCC initiation in both tensile and blunt notch specimens. Somewhat unexpectedly, extensive grain boundary creep cavitation and cracking was observed in these materials along with SCC initiation. Therefore, grain boundary cavitation may play a major role in producing the necessary IG precursor flaws for SCC initiation. Critical strain rates to promote cavitation damage have not been established, nor have experiments been performed to effectively assess the importance of the % cold work on susceptibility. An important aspect will be whether creep strain rates produced under constant load in PWR primary water are sufficient to promote significant grain boundary cavity formation and cracking. These represent key mechanistic issues that must be resolved for alloy 690. Goals of ongoing and near-term experiments will be to determine the influence of material (e.g., %CW and grain boundary microstructure) and stress (e.g., applied load and local K) on grain boundary cavity formation and SCC initiation. Constant load tensile and blunt notch tests will continue to be utilized with microscopic damage quantified by high-resolution characterizations.

Acknowledgments

The authors recognize collaborative research activities funded by the Nuclear Regulatory Commission (SCC crack growth tests on alloy 690 materials), the Office of Basic Energy Sciences (high-resolution grain boundary characterizations) and Rolls Royce (hardness and strain mapping on CW alloy 690 materials). These collaborations have been essential to the success of the SCC initiation research. Critical technical assistance is also recognized from Rob Seffens for SCC experimentation and Clyde Chamberlin for metallographic specimen preparation.

References

[1] *Stress Corrosion Crack Initiation of Alloy 600 in PWR Primary Water Environments*. Technical Milestone Report M3LW-13OR0403032, Light Water Reactor Sustainability Program, DOE Office of Nuclear Energy, March 2013.

[2] *Corrosion and Stress Corrosion Crack Initiation of Cold-Worked Alloy 690 in PWR Primary Water Environments*. Technical Milestone Report M2LW-13OR0402035, Light Water Reactor Sustainability Program, DOE Office of Nuclear Energy, September 2013.

[3] *Corrosion and Stress Corrosion Crack Initiation of Cold Worked Alloy 600 and Alloy 690 in PWR Primary Water Environments*. Technical Milestone Report M2LW-13OR0402035, Light Water Reactor Sustainability Program, DOE Office of Nuclear Energy, September 2014.

[4] D. Alley and D. Dunn, "Testing and analyses of Davis-Besse UNS N06600 control rod drive mechanism nozzles", in *CORROSION 2015,* March 15-19, 2015, Dallas, Texas.

[5] *Characterizations and Stress Corrosion Cracking Evaluations of Alloy 600 CRDM Nozzle Heats from the Davis Besse Nuclear Power Plant*. NRC Report, August 2013.

[6] D. S. Dunn, J. Collins, D. Alley, B. Alexandreanu, M. B. Toloczko and S. M. Bruemmer, "Primary Water Stress Corrosion Cracking Tests and Metallurgical Analysis of Davis Besse Control Rod Drive Mechanism Nozzle #4", in *Proc. 16th Int. Conf. Environmental Degradation of Materials in Nuclear Power Systems – Water Reactors*,

[7] *Microstructure, Corrosion and Stress Corrosion Crack Initiation of Alloy 600 in PWR Primary Water Environments*. Technical Milestone Report M3LW-13OR0403032, Light Water Reactor Sustainability Program, DOE Office of Nuclear Energy, March 2013.

[8] R. A. Etien, E. Richey, D. S. Morton and J. Eager, "SCC initiation testing of alloy 600 in high temperature water", in *15th International Conference on Environmental Degradation of Materials in Nuclear Power Systems-Water Reactors 2011,* 2011, Colorado Springs, CO.

[9] *Pacific Northwest National Laboratory Investigation of Stress Corrosion Cracking in Nickel-Base Alloys*. NUREG/CR-7103, Volume 1, Nuclear Regulatory Commission, Office of Nuclear Regulatory Research, May 2011.

[10] *Pacific Northwest National Laboratory Investigation of Stress Corrosion Cracking in Nickel-Base Alloys*. NUREG/CR-7103, Volume 2, Nuclear Regulatory Commission, Office of Nuclear Regulatory Research, November 2011.

[11] D. J. Paraventi and W. C. Moshier, "Assessment of the Interaction of Variables in the Intergranular Stress Corrosion Crack Growth Rate Behavior of Alloys 600, 82, and 182", in *Proc. 13th Int. Conf. Environmental Degradation of Materials in Nuclear Power Systems - Water Reactors*, Whistler, British Columbia.

[12] R. A. Morris, N. Lewis and D. S. Morton, "3D Analysis of Surface Treatment Effect on the Oxidation of Grain Boundaries in Alloy 600", in *16th Int. Conf. Environmental Degradation of Materials in Nuclear Power Systems – Water Reactors,* 2014: NACE International.

[13] J. P. Berge, "Importance of surface preparation for corrosion control in nuclear power stations", *Materials Performance*, Vol.36, Iss.11, 1997, pp. 56-62.

[14] D. Deforge, L. Duisabeau, S. Miloudi, Y. Thebault, T. Couvant, F. Vaillant and E. Lemaire, "Learnings from EdF Investigations on SG Divider Plates and Vessel Head Nozzles. Evidence of Prior Deformation Effect on Stress Corrosion Cracking", in *Fontevraud 7 - Contribution of materials investigations to improve the safety and performance of LWRs,* 2011, Avignon, France: Societe Francaise d'Energie Nucleaire (SFEN).

[15] P. Scott, M. C. Meunier, F. Steltzlen, O. Calonne, M. Foucault, P. Combrade and C. Amzallag, "Comparison of laboratory and field experience of PWSCC in alloy 182 weld metal", in *13th International Conference on Environmental Degradation of Materials in Nuclear Power Systems 2007,* 2007, Whistler, BC.

[16] C. Amzallag, J. M. Boursier, C. Pages and C. Gimond, "Stress corrosion life assessment of 182 and 82 welds used in PWR components", in *10th International Conference Environmental Degradation of Materials in Nuclear Power Systems - Water Reactors,* 2002: NACE International.

[17] C. S. Shin and C. Q. Cai, "Experimental and finite element analyses on stress intensity factors of an elliptical surface crack in a circular shaft under tension and bending", *International Journal of Fracture*, Vol.129, Iss.3, 2004, pp. 239-264.

[18] J. Toribio, N. Álvarez, B. González and J. C. Matos, "A critical review of stress intensity factor solutions for surface cracks in round bars subjected to tension loading", *Engineering Failure Analysis*, Vol.16, Iss.3, 2009, pp. 794-809.

[19] I. S. Raju and J. C. Newman, "Stress-intensity factors for circumferential surface cracks in pipes and rods under tension and bending loads". 1986, Philadelphia, PA: American Society for Testing and Materials, pp. 789-805.

[20] A. Carpinteri, "Elliptical-arc surface cracks in round bars", *Fatigue & Fracture of Engineering Materials & Structures*, Vol.15, Iss.11, 1992, pp. 1141-1153.

[21] L. A. James and W. J. Mills, "Review and synthesis of stress intensity factor solutions applicable to cracks in bolts", *Engineering Fracture Mechanics*, Vol.30, Iss.5, 1988, pp. 641-654.

[22] M. A. Astiz, "An incompatible singular elastic element for two- and three-dimensional crack problems", *International Journal of Fracture*, Vol.31, Iss.2, 1986, pp. 105-124.

[23] P. Scott, "An analysis of primary water stress corrosion cracking in PWR steam generators", in *NEA/CSNI Specialist Meeting on Operating Experience with Steam Generators,* September 16–20, 1991, Brussels, Belgium.

[24] A. R. McIlree, R. B. Rebak and S. Smialowska, "Relationship of stress intensity to crack growth rate of alloy 600 in primary water", in *International Colloquium on Contribution of materials Investigation to the Resolution of Problems Encountered in PWR Plants,* September 10–14, 1990, Fontevraud, France.

[25] *Materials Reliability Program (MRP) Crack Growth Rates for Evaluating Primary Water Stress Corrosion Cracking (PWSCC) of Thick-Wall Alloy 600 Materials (MRP-55) Revision 1.* EPRI, Palo Alto, CA: 1006695, 2002.

[26] S. Le Hong, "Influence of Surface Condition on Primary Water Stress Corrosion Cracking Initiation of Alloy 600", *Corrosion*, Vol.57, Iss.4, 2001, pp. 323-333.

[27] S. Le Hong, C. Amzallag and A. Gelpi, "Modelling of stress corrosion cracking initiation of Alloy 600 in primary water of PWRs", in *9th International Symposium on Environmental Degradation of Materials in Nuclear Power Systems—Water Reactors,* August 1–5, 1999, Newport Beach, California.

[28] P. Andresen and M. Morra, "Effects of Positive and Negative dK/da on SCC Growth Rates", in *12th International Conference on Environmental Degradation of Materials in Nuclear Power System – Water Reactors,* 2005, Salt Lake City, UT.

[29] E. Richey, D. S. Morton and M. K. Schurman, "SCC initiation testing of nickel-based alloys using in-situ monitored uniaxial tensile specimens", in *12th International Conference on Environmental Degradation of Materials in Nuclear Power Systems-Water Reactors,* 2005, Salt Lake City, UT.

[30] R. L. Klueh, "Discontinuous creep in short-range order alloys", *Materials Science and Engineering*, Vol.54, Iss.1, 1982, pp. 65-80.

[31] *Status Review of Initiation of Environmentally Assisted Cracking and Short Crack Growth*. EPRI, Palo Alto, CA: 1011788, 2005.

[32] *Pacific Northwest National Laboratory Investigation of Stress Corrosion Cracking in Nickel-Base Alloys, Volume 1*. NUREG/CR-7103 Vol. 1, January 2007.

[33] *Pacific Northwest National Laboratory Investigation of Stress Corrosion Cracking in Nickel-Base Alloys, Volume 2*. NUREG/CR-7103 Vol. 2, February 2012.

[34] *Pacific Northwest National Laboratory Investigation of Stress Corrosion Cracking in Nickel-Base Alloys, Volume 3: Stress Corrosion Cracking of Cold Worked Alloy 690 (in review)*. NUREG/CR-7103 Vol. 3, January 2015.

[35] T. Moss and G. S. Was, "Accelerated Stress Corrosion Crack Initiation of Alloy 690 and Alloy 600 in High Temperature Hydrogenated Water", in *16th International Conference on Environmental Degradation of Materials in Nuclear Power Systems-Water Reactors,* 2013, Asheville, NC.